Doping Strategy for Enhanced Photocatalytic Hydrogen Production on Tantalum Layered Perovskite Nanosheets

By

Tuğba Yalçın

A Dissertation Submitted to the
Graduate School of Sciences and Engineering
in Partial Fulfillment of the Requirements for
the Degree of

Doctor of Philosophy

in

Materials Science and Engineering

May 3, 2024

Doping Strategy for Enhanced Photocatalytic Hydrogen Production on Tantalum Layered Perovskite Nanosheets

Koç University

Graduate School of Sciences and Engineering

This is to certify that I have examined this copy of a doctoral dissertation by

Tuğba Yalçın

and have found that it is complete and satisfactory in all respects,
and that any and all revisions required by the final
examining committee have been made.

Committee Members:

Assoc. Prof. Uğur Ünal (Advisor)

Prof. Dr. Alper Uzun

Assoc. Prof. Umut Aydemir

Prof. Dr. Ramazan Yıldırım

Assoc. Prof. Nil Özbek

Date: 03.05.2024

I dedicate this dissertation to my family and my closest friends for their endless support, being with me in difficult times, and believing in my life.

ABSTRACT

Doping Strategy for Enhanced Photocatalytic Hydrogen Production on Tantalum Layered Perovskite Nanosheets

Tuğba Yalçın

Doctor of Philosophy in Materials Science and Engineering

May 3, 2024

Rise in greenhouse gas levels due to human activity, such as burning fossil fuels, causes global warming and environmental problems. Thus, industries and researchers are investigating alternative energy sources to find solutions to environmental problems and slow down global warming. Hydrogen is one of the solutions to these problems. Semiconductor photocatalysis has been researched for hydrogen production as a sustainable energy source since the 18th century. Many photocatalysis materials, such as metal oxide, metal sulfide, and metal nitride, have been studied and used as photocatalysts. In addition to these materials, layered perovskite oxides have gained significant interest in the photocatalytic field over the last 20 years—the heightened interest results from its tunable band structure, flexible interlayer structure, and tunable morphology. Furthermore, exfoliating layered materials gives 2D building blocks of bulk materials. Resulting nanosheets with few atomic layers offer a high surface area, low migration distance, and high charge separation to improve photocatalytic activity. Although there is a vast interest for efficient H_2 production with photocatalytic water splitting, research on H_2 production activities needs a long way to go to achieve solar-hydrogen efficiencies above 10%, raising questions about strategies to achieve effective photocatalytic activity.

The common approach to achieve a high productivity from a photocatalyst is to use co-catalysts, which improves charge separation in photocatalysts. In general, noble metals like Pt are used as cocatalysts in nanoparticle form on the surface of photocatalyst. In this case, the inner atoms of the catalysts are inactive since only surface atoms play a role in catalytic activity. In this study, the effects of introducing Pd, Sn, and N into the structure were conducted for photocatalytic hydrogen production in an aqueous 10 vol.% methanol solution as a sacrificial agent without cocatalyst. After exfoliation of tantalum-based perovskite oxide, PdO_6 and SnO_6 octahedra were formed when Ta was substituted

with Pd or Sn, which acted as a single-atom catalyst site (SACs). These obtained octahedra structures reduce the original phase's electrical structure and serve as sites for trapping electrons, thereby reducing the recombination rate of photo-induced carriers.

Furthermore, exfoliated materials have high surface areas, making them ideal platforms to disperse SACs uniformly. This allows for the use of all metal atoms added to the structure with nearly 100% photocatalytic activity. On the other hand, nitrogen, which is partly substituted for oxygen, has a great potential to minimize electronic band energies due to the formation of isolated electronic states positioned above the top of the oxygen (O) 2p valence band. Various structural, spectroscopic, and electrochemical characterization techniques were used to analyze materials' properties in detail. According to the results, all target materials were successfully synthesized, their bandgap changes were determined, and their hydrogen production rates increased after the doping and proton exchange processes.

ÖZETÇE

Tantal Katmanlı Perovskit Nanotabakalarda Geliştirilmiş Fotokatalitik Hidrojen Üretimi için Katkı Stratejisi

Tuğba Yalçın

Malzeme Bilimi ve Mühendisliği, Doktora

3 Mayıs 2024

Fosil yakıtların yakılması gibi insan faaliyetleri nedeniyle sera gazı seviyelerinin yükselmesi küresel ısınmaya ve çevre sorunlarına neden olmaktadır. Bu nedenle, endüstriler ve araştırmacılar çevre sorunlarına çözüm bulmak ve küresel ısınmayı yavaşlatmak için alternatif enerji kaynaklarını araştırmaktadır. Hidrojen bu sorunların çözümlerinden biridir. Yarı iletken fotokataliz, 18. yüzyıldan beri sürdürülebilir bir enerji kaynağı olarak hidrojen üretimi için araştırılmaktadır. Metal oksit, metal sülfür ve metal nitrür gibi birçok fotokataliz malzemesi üzerinde çalışılmış ve foto katalizör olarak kullanılmıştır. Bu malzemelere ek olarak, katmanlı perovskit oksitler son 20 yılda fotokatalitik alanda önemli bir ilgi görmüştür- artan ilgi, ayarlanabilir bant yapısı, esnek ara katman yapısı ve ayarlanabilir morfolojisinden kaynaklanmaktadır. Ayrıca, katmanlı malzemelerin pul pul dökülmesi, yığın malzemelerin 2D yapı taşlarını verir. Ortaya çıkan az sayıda atomik katmana sahip nano tabakalar, fotokatalitik aktiviteyi iyileştirmek için yüksek yüzey alanı, düşük göç mesafesi ve yüksek yük ayrımı sunar. Fotokatalitik su ayrıştırma ile verimli H_2 üretimi için büyük bir ilgi olmasına rağmen, H2 üretim faaliyetleri üzerine yapılan araştırmaların %10'un üzerinde güneş-hidrojen verimliliği elde etmek için uzun bir yol kat etmesi gerekiyor ve bu da etkili fotokatalitik aktivite elde etme stratejileri hakkında soruları gündeme getiriyor.

Bir foto katalizörden yüksek verimlilik elde etmek için yaygın yaklaşım, foto katalizörlerde yük ayrımını iyileştiren eş-katalizörlerin kullanılmasıdır. Genel olarak, Pt gibi soy metaller foto katalizör yüzeyinde nanoparçacık formunda ko-katalizör olarak kullanılır. Bu durumda, katalizörlerin iç atomları inaktiftir, çünkü katalitik aktivitede sadece yüzey atomları rol oynar. Bu çalışmada, Pd, Sn ve N'nin yapıya dahil edilmesinin etkileri, ko-katalizör olmadan hacimce %10'luk sulu metanol çözeltisinde fotokatalitik hidrojen üretimi için gerçekleştirilmiştir. Tantal bazlı perovskit oksidin pul pul

dökülmesinden sonra, Ta, tek atomlu katalizör bölgesi (SACs) olarak işlev gören Pd veya Sn ile ikame edildiğinde PdO_6 ve SnO_6 oktahedraları oluşmuştur. Elde edilen bu oktahedra yapılar, orijinal fazın elektriksel yapısını azaltır ve elektronları yakalamak için bölgeler olarak hizmet eder, böylece foto-indüklenmiş taşıyıcıların rekombinasyon oranını azaltır. Ayrıca, pul pul dökülmüş malzemeler yüksek yüzey alanlarına sahiptir, bu nedenle SAC'leri eşit şekilde dağıtmak için ideal platformlardır. Bu sayede yapıya eklenen tüm metal atomlarının neredeyse %100 verimlilikle kullanılmasına olanak tanır. Öte yandan, kısmen oksijen yerine ikame edilen azot, oksijen (O) 2p valans bandının tepesinin üzerinde konumlanmış izole elektronik durumların oluşumu nedeniyle elektronik bant enerjilerini en aza indirmek için büyük bir potansiyele sahiptir. Malzemelerin özelliklerini ayrıntılı olarak analiz etmek için çeşitli yapısal, spektroskopik ve elektrokimyasal karakterizasyon teknikleri kullanılmıştır. Sonuçlara göre, tüm hedef malzemeler başarılı bir şekilde sentezlenmiş, bant aralığı değişimleri belirlenmiş ve doping ve proton değişim süreçlerinden sonra hidrojen üretim oranları artmıştır.

ACKNOWLEDGEMENTS

First and foremost, I would like to express my profound gratitude to my supervisor, Assoc. Prof. Uğur Ünal, for his invaluable guidance, support, and encouragement throughout my Ph.D. studies. Assoc. Prof. Ünal's expertise in inorganic material characterization, layered perovskite catalysis synthesis, and electrochemical techniques has significantly contributed to the improvement and focus of my research. His patience with my questions during the early stages of developing my research topic was instrumental in helping me gain a deeper understanding of the field and refine my research focus. I also look forward to continuing to collaborate with him and to learning from him in the future.

I would like to express my sincerest gratitude to the members of my thesis committee, namely Prof. Alper Uzun, Assoc. Prof. Dr. Umut Aydemir, Prof. Ramazan Yıldırım, and Assoc. Prof. Dr. Nil Özbek, for their invaluable contributions in terms of their time, expertise, and constructive criticism, which have significantly contributed to the improvement of this work.

The Scientific and Technological Research Council of Turkey (TÜBİTAK) is gratefully acknowledged for its financial support to the 1001 project (Scientific and Technological Research Projects Support Program) titled "***2D nanosheets of layered perovskites for photocatalytic CO_2 reduction reactions***" with project number 118Z865. 2214-A International Research Scholarship Program enabled me to participate in the Functional Materials and Material Modeling – Alpay Research Group between May and July 2023, and the TÜBİTAK 2244-Industry Ph.D. Program between Arçelik A.Ş and Koç University with project number 118C124, which provided scholarships, tuition support, research opportunities, and access to resources. Furthermore, as a result of this collaboration, I was offered a position as a Research and Development Senior Expert Engineer at Arçelik after the program. I would like to express my gratitude to Dr. S. Alper Yeşilçubuk. from Arçelik for his understanding and supportive attitude throughout my doctoral education. I would also like to thank Dr. Simge Tarkuç.

I would also like to express my gratitude to my colleagues at Unal Lab. In particular, I would like to thank M. Tuğrul Avcu for his invaluable support and assistance throughout my doctoral studies. Despite encountering numerous challenges, I was able to

maintain uninterrupted progress in my experimental studies thanks to his guidance and encouragement. It is beyond the scope of this written expression to convey the significance and import of the assistance you have provided. Nevertheless, I express my gratitude with sincerity. I would like to acknowledge two individuals who fostered a sense of belonging, infused my experimental process with joy when I commenced my Ph.D., and openly shared their ideas and suggestions to facilitate my growth. The first of these is Ali Berk Demir, and the second is Kaan Yalçın.

I would like to express my gratitude to my closest friends for their unwavering support, encouragement, and understanding throughout my academic journey. Their friendship has been a constant source of motivation and strength, helping me navigate the challenges and celebrate successes. I am truly fortunate to have such a wonderful friend by my side, and I am deeply grateful for their presence in my life. With their cooperation, this research was possible. I can list the names of these friends as follows: I would like to extend my gratitude to the following individuals for their invaluable contributions to this research: Tuba Kara, Hatice Tokmak, Büşra Çiçekalan, Özge Payanda Konuk, İlayda Terzi, Canberk Sezer, Pelda Akın, Kübra Nur Özvural, Güncem Özgün Eren, Asım Önal, Şule Meltem Sinanoğlu, Negin Ahmetoğlu, Atakan Koçanalı, Onur Konuk, and Şeyma Yılmaz, Şule Bayrak.

I am deeply grateful to my family for their endless love, encouragement, and understanding throughout this journey. Their constant belief in me has been my greatest motivation. Finally, thank you to everyone who has played a part, big or small, in completing this thesis.

Table of Contents

List of Tables

List of Figures

Abbreviations

XRD	X-Ray Diffraction
UV-vis DRS	Ultraviolet-Visible Diffuse Reflection Spectroscopy
XRD	X-Ray Photoelectron Spectroscopy
ICP-MS	Inductively Coupled Plasma-Mass Spectrometry
BET	Brunauer-Emmett-Teller
CA	Chronoamperometry
PEIS	Potentiostatic Electrochemical Impedance Spectroscopy
GC	Gas Chromatograph
W.E.	Working Electrode
C.E.	Counter Electrode
R.E.	Reference Electrode
VBM	Valence Band Maximum
CBM	Conduction Band Minimum
HER	Hydrogen Evolution Reaction
OER	Oxygen Evolution Reaction
PEC	Photoelectrochemical
PC	Photocatalytic
WS	Water-Splitting
vdW	Van Der Waals
KM	Kubelka-Munk
BE	Binding Energies
PCM	Polymerized Complex Method
LPOs	Layered Perovskite Oxides
SACs	Single Atomic Catalysts
NSs	Nanosheets
2D	Two-Dimensional
Eg	Band Gap Energies
DJ	Dion-Jacobson
RP	Ruddlesden-Popper
AV	Aurivillius
TBPOH	Tetrabutylphosphonium Hydroxide
TBAOH	Tetrabutylammonium Hydroxide
TBA	Tetrabutylammonium
FTO	Fluorine-Doped Tin Oxide
$CsCa_2Ta_3O10$	CCTO
$HCa_2Ta_3O_{10}$	HCTO
$[Ca_2Ta_3O_{10}]^-$	CTO
$CsCa_2Ta_3O_{10-y}N_y$	CCTOx
$HCa_2Ta_3O_{10-y}N_y$	HCTOx

$[Ca_2Ta_3\ O_{10-y}N_y]^-$	CTOx
1.5%Pd-$CsCa_2Ta_3O10$	1.5%Pd-CCTO
1.5%Pd-$HCa_2Ta_3O_{10}$	1.5%Pd-HCTO
1.5%Pd- $[Ca_2Ta_3O_{10}]^-$	1.5%Pd-CTO
3%Pd-$CsCa_2Ta_3O10$	3%Pd-CCTO
3%Pd-$HCa_2Ta_3O_{10}$	3%Pd-HCTO
3%Pd- $[Ca_2Ta_3O_{10}]^-$	3%Pd-CTO
5%Pd-$CsCa_2Ta_3O10$	5%Pd-CCTO
5%Pd-$HCa_2Ta_3O_{10}$	5%Pd-HCTO
5%Pd- $[Ca_2Ta_3O_{10}]^-$	5%Pd-CTO
1.5%Pd-$CsCa_2Ta_3\ O_{10-y}N_y$	1.5%Pd-CCTOx
1.5%Pd-$HCa_2Ta_3\ O_{10-y}N_y$	1.5%Pd-HCTOx
1.5%Pd- $[Ca_2Ta_3\ O_{10-y}N_y]^-$	1.5%Pd-CTOx
$CsLaTa_2O_7$	CLTO
H $LaTa_2O_7$	HLTO
$[LaTa_2O_7]^-$	LTO
$CsLaTa_2O_{7-y}N_y$	CLTOx
$HLaTa_2O_{7-y}N_y$	HLTOx
$[LaTa_2O_{7-y}N_y]^-$	LTOx
1.5%Pd- $CsLaTa_2O_7$	1.5%Pd-CLTO
1.5%Pd- $HLaTa_2O_7$	1.5%Pd-HLTO
1.5%Pd- $[LaTa_2O_7]^-$	1.5%Pd-CLO
3%Pd- $CsLaTa_2O_7$	3%Pd-CLTO
3%Pd- $HLaTa_2O_7$	3%Pd-HLTO
3%Pd- $[LaTa_2O_7]^-$	3%Pd-CLO
5%Pd-$CsCa_2Ta_3O10$	5%Pd-CLTO
5%Pd-$HCa_2Ta_3O_{10}$	5%Pd-HLTO
5%Pd- $[Ca_2Ta_3O_{10}]^-$	5%Pd-CLO
1.5%Pd- $CsLaTa_2O_{7-y}N_y$	1.5%Pd-CLTOx
1.5%Pd- $CsLaTa_2O_{7-y}N_y$	1.5%Pd-HLTOx
1.5%Pd- $[LaTa_2O_{7-y}N_y]^-$	1.5%Pd-LTOx
0,75%Sn- $CsLaTa_2O_7$	0.75%Sn-CLTO
0,75%Sn- $HLaTa_2O_7$	0.75%Sn-HLTO
0,75%Sn- $[LaTa_2O_7]^-$	0.75%Sn-LTO
1.5%Sn- $CsLaTa_2O_7$	1.5%Sn-CLTO
1.5%Sn- $HLaTa_2O_7$	1.5%Sn-HLTO
1.5%Sn- $[LaTa_2O_7]^-$	1.5%Sn-CLO

3%Sn- $CsLaTa_2O_7$	3%Sn-CLTO
3%Sn- $HLaTa_2O_7$	3%Sn-HLTO
3%Sn- $[LaTa_2O_7]^-$	3%Sn-CLO
5%Sn- $CsLaTa_2O_7$	5%Sn-CLTO
5%Sn- $HLaTa_2O_7$	5%Sn-HLTO
5%Sn- $[LaTa_2O_7]^-$	5%Sn-CLO

Chapter 1: Introduction

This thesis aimed to explore layered perovskite photocatalyst materials that are effective in both the ultraviolet and visible regions for photo-driven water splitting. In order to achieve this goal, it was necessary to create a single atomic catalyst site within the ultra-thin perovskite metal oxide layers obtained by adding low amounts of metal to the B field in the crystal structure of the metal oxide layers of layered perovskites in the Dion-Jacobson phase. The incorporation of single atomic catalysts (SACs) within the metal oxide nanolayers is expected to enhance the photocatalytic performance and provide high selectivity. The doping of N in the oxygen regions of the perovskite structure is also aimed at modifying the absorption peak of the material. It is postulated that this will increase light absorption due to the potential for substituting N on the O sides to create isolated states on the upper part of the O 2p valence band. This thesis represents a pioneering study in the synthesis of single-site noble metal doped two-dimensional nanosheets of perovskite-type layered oxides as new photocatalytic materials for both ultraviolet and visible light. The materials produced will be among the first to demonstrate effective photocatalytic activity in the literature.

This chapter summarizes photocatalytic water-splitting as a potential solution to the global energy crisis. The subsequent chapters present a discussion of synthesis and characterization methods in Chapter 2, the comparison of photocatalytic hydrogen evolution of two- and three-layer Tantalum-Based Oxynitride in Chapter 3, the performance effect of Pd single-site metal doped 2D nanosheets on photocatalytic hydrogen evolution for three-layered in Chapter 4 and for two-layered in Chapter 5, the performance effect of Sn single-site metal doped 2D nanosheets on photocatalytic hydrogen evolution for two-layered in Chapter 6. Finally, a comprehensive conclusion of the research findings in Chapter 7.

1.1 Climate Change and Renewable Energy

By the mid-21st century, the exponential growth of technological advancements had caused a population explosion and a concomitant increase in energy requirements. Electricity is vital today but relies heavily on unsustainable fossil fuels (nearly 80%, according to a 2020 Global Status report in Figure 1.1) [2]. Unarguably, a clean and sustainable mix of renewable energy sources, such as solar, wind, and others, is directed

to meet this energy demand due to reaching the threshold level of use of fossil energy sources.

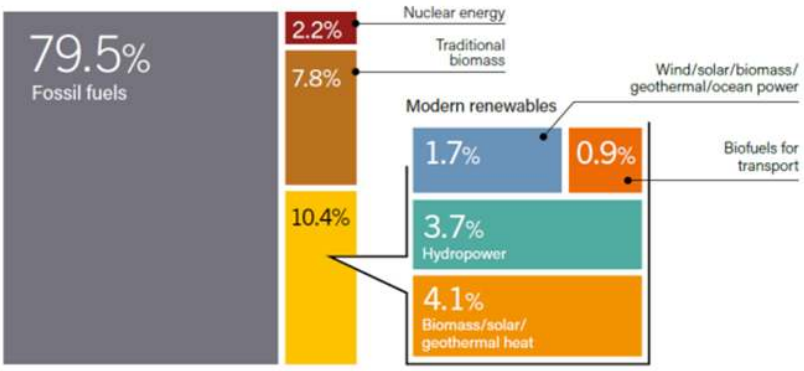

Figure 1.1. The ratio of renewable energy sources to global energy use in 2018 [2].

Renewable energy sources like solar, wind, and biomass are gaining research attention [3]. Solar energy is the most valuable, high amount of abundant, and highly efficient, with a vast capacity of 1575-49387 EJ per year, significantly more than our global annual energy consumption of 559.8 EJ [2]. Therefore, there is a need for a game-changer solution that uses clean energy from the sun and tackles climate change caused by burning fossil fuels. One exciting solution being explored is solar hydrogen production from water since this gas has a considerable energy capacity and zero-emission and clean energy [4]. As shown in Figure 1.2, the annual number of research papers on solar H_2 production has increased rapidly since 2005.

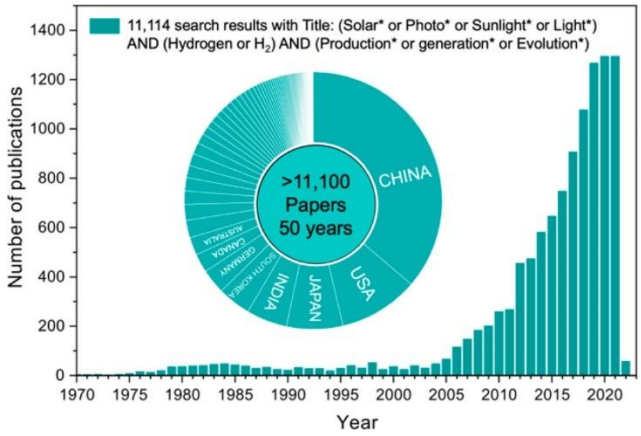

Figure 1.2 Number of publications searched by the words (Solar* or Photo* or Sunlight* or Light*) and (Hydrogen or H_2) and (Production* or Generation* or Evolution*) in their titles [5].

Even though intensive studies continue, photocatalytic hydrogen production performance in particle photocatalysis still needs to be at the expected level [6]. Possible strategies to increase solar to chemical conversion rate and improve charge transfer include structural, elemental doping, and defect engineering [7]. Explanations about this are given in section 1.4.

1.2 General Approaches for Water Splitting Methods

The solar-powered hydrogen evolution reaction (HER) can be employed in two principal ways: photocatalytic (PC) and photoelectrochemical (PEC). [8]. Both of these methods are discussed in detail below.

1.2.1 Basic Principle of Photocatalytic Water Splitting

In photocatalytic water-splitting (WS), solar energy can be used to split water molecules into hydrogen and oxygen gases on the surface of a light-activated catalyst, typically a semiconductor material in Figure 1.3. While splitting water seems straightforward, achieving it remains a considerable challenge. The reaction is thermodynamically unfavorable due to a positive standard Gibbs free energy change ($\Delta G^0 = +237$ kJ/mol). According to the Nernst equation[9], this corresponds to a positive standard electrode potential ($\Delta E^0 = 1.23$ V) [10].

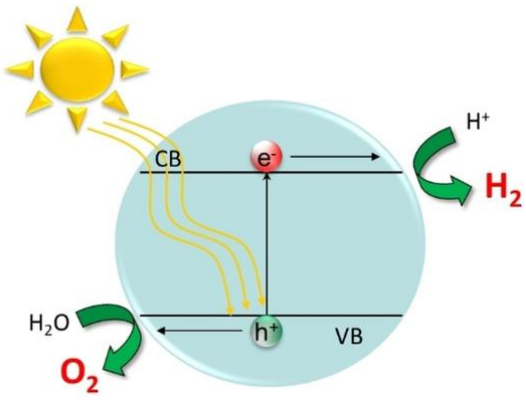

Figure 1.3 Schematic illustrations of water splitting process [11]

Water oxidation to oxygen especially requires a four-electron transfer and can be highly complex. Hydrogen evolution is more straightforward than water oxidation, requiring

only a two-electron transfer [11]. This difference in electron transfer necessitates the following overall water-splitting reaction:

$$Water\ Oxidation: 2H_2O + 4h^+ \rightarrow 4H^+ + O_2 \quad (1.1)$$

$$Water\ reduction: 4H^+ + 4e^- \rightarrow 2H_2 \quad (1.2)$$

$$Overall\ water\ splitting: 2H_2O \rightarrow 2H_2 + O_2\ \Delta G^0 = +237\ \text{kJ/mol} \quad (1.3)$$

The critical steps in photocatalytic WS are as follows. The semiconductor's bandgap should be greater than 1.23 eV for photocatalytic water splitting. If the photon energy exceeds the semiconductor's bandgap, photo-induced electrons (e^-) and holes (h^+) are generated in its conduction and valence bands. These light-induced electron-hole (h^+) pairs then sequentially participate in surface chemical reactions at the semiconductor-electrolyte interface, driving the reduction of water to hydrogen gas (H_2) and the oxidation of water to oxygen gas (O_2) as given

in Figure 1.3[12].

1.2.2 Basic Principle of Photoelectrocatalytic Water Splitting

The photoelectrocatalytic (PEC) method in Figure 1.4. works together with photocatalysis and electrocatalysis [13]. Typically, photocatalysts are deposited on conductor substrates to form photoanodes or photocathodes for water splitting. In this system, light energy generates electricity using a semiconductor/electrolyte interface, similar to a battery.

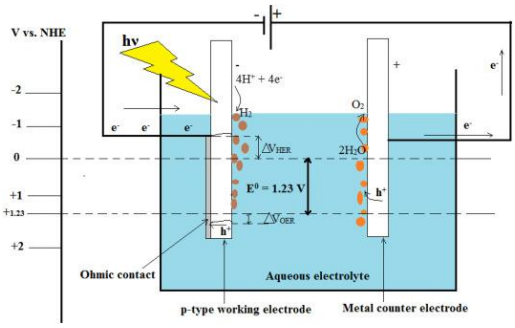

Figure 1.4 Working principle of a photoelectrochemical device [14]

The pioneering work on PEC water-splitting dates back to the 18th century. In 1972, Fujishima and Honda successfully demonstrated hydrogen production through

photoelectrochemical (PEC) water-splitting. Following the initial breakthrough, significant efforts have been made to assess the commercial feasibility of this research area [15]. Following the initial breakthrough, significant efforts have been made to synthesize other oxide materials as candidates for photo-electrodes that do not require an external bias for water decomposition. Studies reveal that perovskite oxide materials like $BaTiO_3$ [16] and $SrTiO_3$ [17], [18], [19] exhibit significantly lower light energy conversions than TiO_2, requiring no external bias.

The dissertation primarily examines the potential of perovskite oxides for producing solar hydrogen fuels. Figure 1.5 shows that several ABO_3 perovskites have been studied in the literature as potential materials for water splitting. Examples include $NaTaO_3$ [20], $KNbO_3$ [21], $NaNbO_3$ [22], $BaTiO_3$[23]. Figure 1.5 indicates oxide band gaps, reduction and oxidation potential, and their conduction and valance bands compared to water's reduction and oxidation potentials.

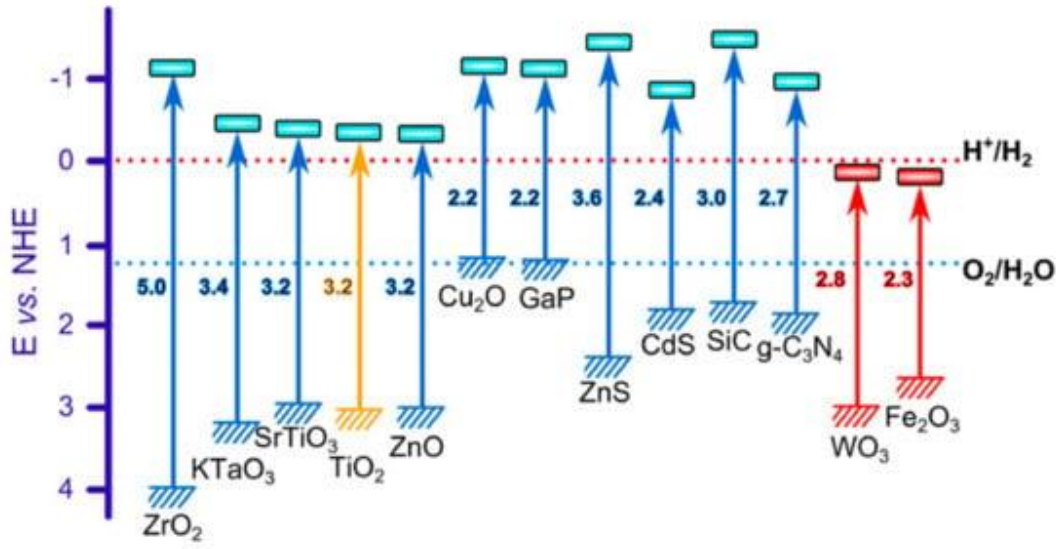

Figure 1.5 The study plots the conduction bands, valence bands, and band gaps of common oxide semiconductors, along with their oxidation and reduction potential of water at pH=0 [24].

Additionally, the derivatives of perovskite oxides, such as layered perovskite oxides and oxynitrides, were started to be investigated in terms of their hydrogen or oxygen production performance over the last few decades. Some representative pristine and modified layered perovskites display water-splitting performances under visible light in Figure 1.6. Even though their application in industry is still limited, the modified materials exhibit dramatic increases in photocatalysis and great potential for future use.

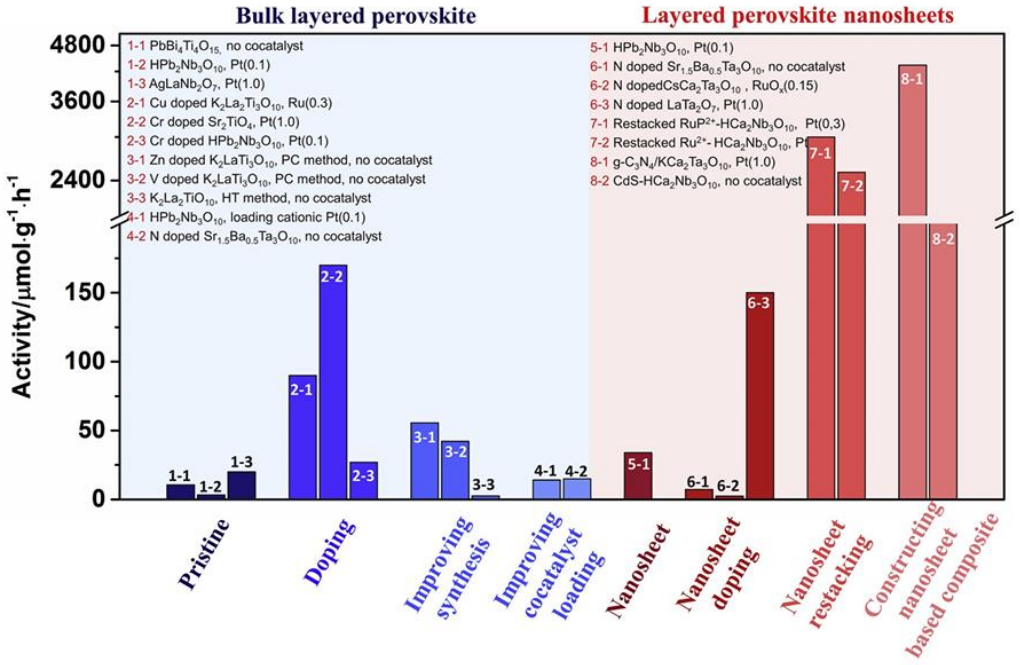

Figure 1.6 The study examines the photocatalytic activities of water splitting performances (H_2 generation rate) from pristine and modified layered perovskites under visible-light irradiation.

1.3 Layered Perovskite Oxides (LPOs)

The ideal cubic perovskite oxide, the general formula ABO_3 (A: alkaline/rare earth cation, B: transition metal cation), is a parent structure for layered perovskite materials. The layered oxide structure has a stacked structure consisting of extensive 2D ABO_3 slabs. These slabs include a 3D network of corner-sharing BO_6 octahedra where A (12 coordinated) locates the interstitial lattice sites [25], as seen in Figure 1.7 below.

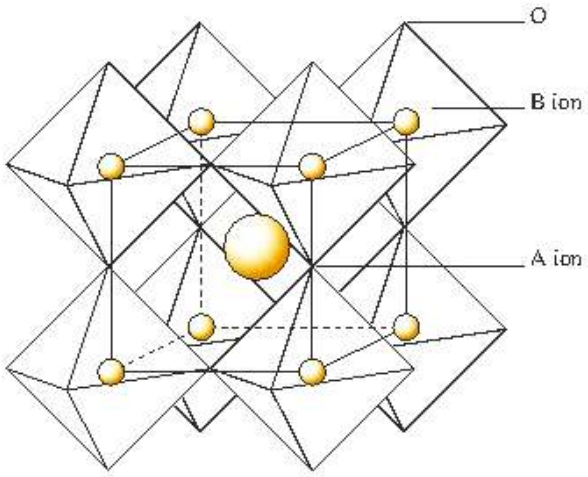

Figure 1.7 Illustration of cubic perovskite oxide structure [26].

In contrast to other oxides, perovskite oxides play an important role in broad applications in catalysis [27], metal batteries [28], and solid oxide fuel cells [29] due to their remarkable structural versatility and compositional flexibility. The total or partial intercalation of versatile metal cations in perovskite oxides' A and B sites also allows them to be used as redox catalysts, such as in OER [30], [31], [32] and HER [33], [34], [35] and to expand the perovskite family and finely tune its properties. Therefore, over two hundred perovskite-based materials have been documented in photocatalytic applications. Table 1.1 exhibits some layered perovskite oxides investigated for photocatalytic water splitting.

Table 1.1 Layered perovskite oxides investigated for photocatalytic water splitting in the literature.

Chemical Formula	**E_g (eV)**	**Sacrificial reagent**	**Co-catalyst**	**H_2 (µm/g.h)**	**Light Type**	**Ref.**
$K_2La_2Ti_3O_{10}$	3,69	Methanol		6,0	Hg lamp $\lambda < 420$ nm	[36]
$K_2La_2Ti_3O_{10-x}N_x$	3,44	Methanol		7,2	Hg lamp $\lambda < 420$ nm	[36]
$KLaTiO_4$	3,54	Methanol	Pt	30,5	Xe lamp $\lambda > 300$ nm	[37]

$KLaTiO_{4-x}N_x$	2,12	Methanol	Pt	2,9	Xe lamp λ > 300 nm	[37]
$Na_2Ca_2Nb_4O_{13}$	3,3	Methanol	Pt 1%	1355	Xe lamp	[38]
Rh / Ln doped $Ca_3Ti_2O_7$		Methanol	Pt 1%	3.3	Xe arc lamp λ > 420 nm	[39]
$Bi_2SrTa_2O_9$	3,44	Methanol		0,5	Xe lamp λ > 300 nm	[40]
$SrTa_2O_9$	3,73	Methanol		16,5	Xe lamp λ > 300 nm	[40]
$H_{1.81}Sr_{0.81}Bi_{0.19}Ta_2O_9$	3,88	Methanol		57.67	Hg lamp λ > 300 nm	[41]
$K_{0.5}La_{0.5}Bi_2M_2O_9$ (M = Ta, Nb)	3,4			5,9	Hg lamp	[42]
$PbBi_2Nb_2O_9$	2,8	Methanol $AgNO_3$		7.6	Xe lamp λ > 420 nm	[44]
$KCa_2Nb_3O_{10}$	3,6		Pt 1%	21,6	Xe lamp λ > 300 nm	[45]
$HLaNb_2O_7$	4,2	Methanol	Pt	4800	Hg lamp λ > 300 nm	[46]
Ag/$RbLaNb_2O_7$, $RbA_2Nb_3O_{10}$	2,4-3,7	Methanol	Pt (1 wt.%)	13616	Xe lamp λ > 300 nm	[47]
2D- $Ca_2NbTa_2O10^-$		Methanol	Pt	1500	Xe lamp λ > 300 nm	[48]
$CsCa_2Ta_3O_{10-x}N_x$		Methanol	Rh (0,15 wt.%)	15610	Xe lamp	[49]
$CsCa_2Ta_3O_{10-x}N_x$		Methanol	Rh (0,15 wt.%)	10	Xe lamp λ > 420 nm	[49]

$RbLaTa_2O_{6.77}N_{0.15}$	2.9	Methanol	Pt %2	2800	Xe lamp λ > 420 nm	[50]
$RbNdTa_2O_7$	3,8			234.8	Xe lamp λ > 300 nm	[51]

Even though the perovskite structure was introduced as ABO_3, its derivates depend on their lattice plane parameters. For instance, ($A_{n+1}B_nO_{3n+3}$) has the layer of (111) plane, whereas ($A_nB_nO_{3n+2}$) structure has the layer of (110) plane [52]. There are three types of (100) layered perovskites, which are the Ruddlesden-Popper phase ($A_{n+1}B_nO_{3n+1}$), Dion-Jacobson phase (A'[$A_{n-1}B_nO_{3n+1}$]), and Aurivillius phase (Bi_2O_2)($A_{n-1}B_nO_{3n+1}$) [52]. The detailed crystal structures for the (100) layered perovskite family illustrated below are shown in Figure 1.8. The number (represented by "n") of BO_6 octahedra in a stacked layer determines the thickness of each layer.

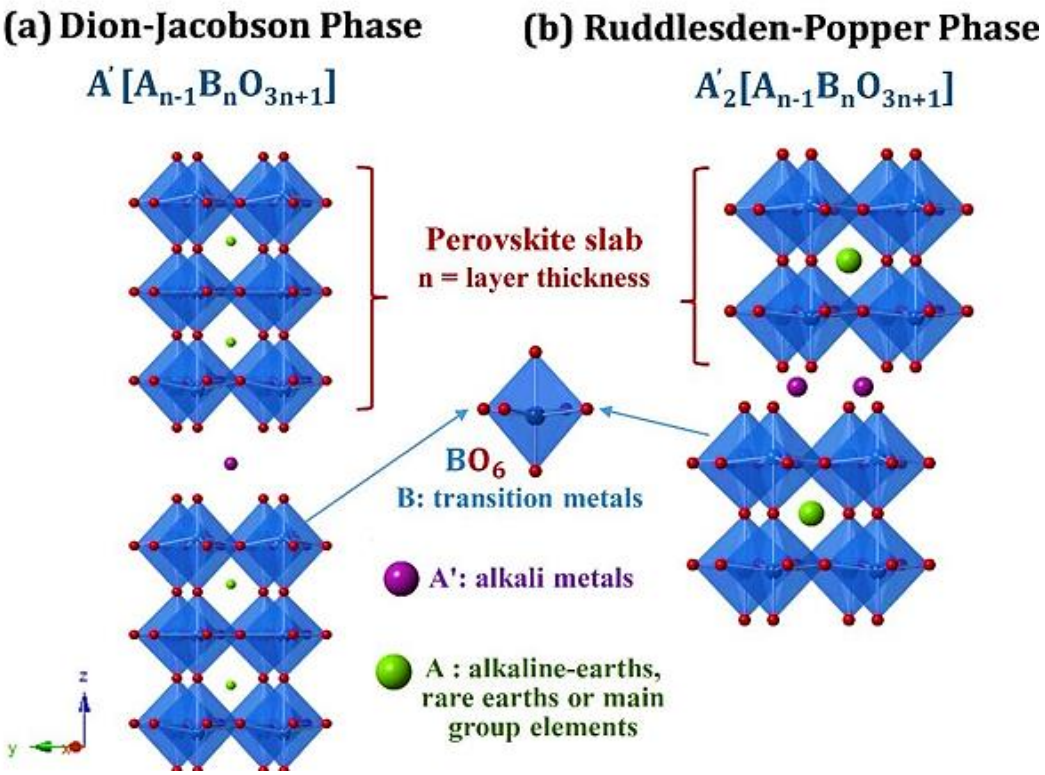

Figure 1.8 Two important families of (100) layered oxide perovskite structures of (a) a triple-layered Dion-Jacobson and (b) a double-layered Ruddlesden-Popper [53].

According to Figure 1.8, a difference between Dion-Jacobson (DJ) and Ruddlesden-Popper (RP) is that the latter has twice the interlayer charge density as the first. Aurivillius (AV) has the same structure as Ruddlesden-Popper but stacked Bi_2O_2 layers arranged between the perovskite layers [54]. Despite strongly covalent bonding in stacked perovskite slabs, the interaction between the perovskite sheets and the A-cations primarily relies on van der Waals (vdW) forces [55]. These vdW interactions contribute to overall stability, allowing for flexibility and facilitating interactions between adjacent layers [56]. The soft structure enables the exfoliation of monolayers and restacking [57]. The exfoliation technique considerably enhances their photocatalytic performance due to reduced material thickness and increased specific surface area [58]. A detailed explanation of this technique is discussed in detail in section 1.4.3.

1.4 Topochemical Manipulation of Layered Perovskites

Despite their excellent photocatalytic activity, perovskite materials need significant improvements in stability and performance to be viable for industrial use. In addition, pristine layered perovskite has limited absorption of visible light and insufficient charge separation efficiencies, which fail to ensure efficient gas generation [59]. In order to achieve the desired photocatalytic performance, layered perovskite materials must undergo a series of modifications [60]. These include the use of a co-catalyst, band-gap engineering and the exfoliation of layered perovskites. A summary of these modifications is provided below in sequential order.

1.4.1 The use of co-catalyst

Layered perovskite oxide materials (LPOs) require additional catalysts to split water effectively, and platinum (Pt) is often used for this purpose. Pt nanoparticles increase the efficiency of photocatalysis by preventing the recombination of electrons and holes. However, Pt is costly, and how it is loaded into the material can affect its effectiveness [61]. The layered perovskite (n=4) Ruddlesden-Popper phase $Na_2Ca_2Nb_4O_{13}$ was prepared by Arney et al. [38]. The photocatalytic rates for hydrogen production under ultraviolet light for platinized RP particles in %20 (v/v) methanol solution were found to range from ~230 to 1355 $\mu molg^{-1}h^{-1}$ in the photochemical

deposition (PCD) method of platinization and ~113–1099 μmol$g^{-1}h^{-1}$ in impregnation method (IWI) of platinization. The result of Arney's study shows that the PCD method enhances photocatalytic activity by precisely placing platinum cocatalysts on specific sites, unlike the less targeted IWI method, which results in more minor improvements. Many previous studies have demonstrated that forming platinum islands on the surface of semiconductors can act as a catalyst to facilitate water reduction to generate H_2 [62], [63]. Researchers are looking for cheaper cocatalysts made from readily available materials to reduce the cost of this technology [64]. For example, Shimizu et al. [65] display that adding Ni as a co-catalyst to $H_2La_{2/3}Ta_2O_7$ significantly enhances H_2 and O_2 evolution rates. This enhancement is particularly pronounced with a NiO content of 0.5 wt. %, reaching maximum activity at 2 wt. % and decreasing slightly with higher NiO content. This effect is attributed to the short-distance migration of photogenerated electrons and holes to adjacent Ni (II) and surface TaO_6 sites, respectively, separating electron-hole pairs. To put it briefly, co-catalysts play two crucial roles in efficient photocatalysis: providing active reaction sites to reduce the activation energy barrier for reduction-oxidation reactions and acting as a charge sink to facilitate electron and hole separation, reducing charge recombination rate [66].

Although they serve as a kinetic aid for reducing water to give hydrogen, co-catalysis has limited active sites. Because only surface atoms can participate in catalysis. The potential benefit of atoms on the inner side of a nanoparticle remains underutilized. Additionally, material waste must be minimized because of the high cost of precious metal catalysts such as iridium and platinum. Scientists predict that if each atom can be used as a catalytic reaction center, it will significantly increase the amount of active catalyst and the number of reactions that can coincide [67], [68]. Single-atom catalysts (SACs) are increasingly popular due to their unique advantages, including maximum atom utilization and homogenous active sites for exceptional catalytic selectivity, activity, and stability in this context [69]. Furthermore, these catalysts have the strategic dispersion of individual metal atoms onto high-surface-area support materials [70], [71]. The accessibility of all metal atoms is maximized in this strategic dispersion, optimizing precious metal utilization and demonstrably enhancing catalytic activity and efficiency [72]. Due to their remarkable thinness at the atomic level and extensive surface area, Nanosheets provide an ideal platform for the dispersion of SACs. This structure effectively hinders the aggregation of

single metal atoms. [73], [74]. Xueli Zheng and others stated that the water oxidation activity of IrNiFe SACs was due to the highly oxidized Ir single atom in NiFe oxyhydroxide. The optimum catalyst was obtained by increasing the oxidation state and modulating the Ir active sites. A unique in situ cryogenic-photochemical reduction method has successfully achieved Ir single atomic regions [75]. In conclusion, SACs utilize the intrinsic electronic characteristics of nanosheets, allowing for precise adjustment of the electronic structure of metal atoms to enhance catalytic performance in targeted reactions, as illustrated in Figure 1.9. Further, a single-site atom refers to an isolated atomic region [73] that serves both as a producer of photocatalytic solar products and as a co-catalyst on the surface.

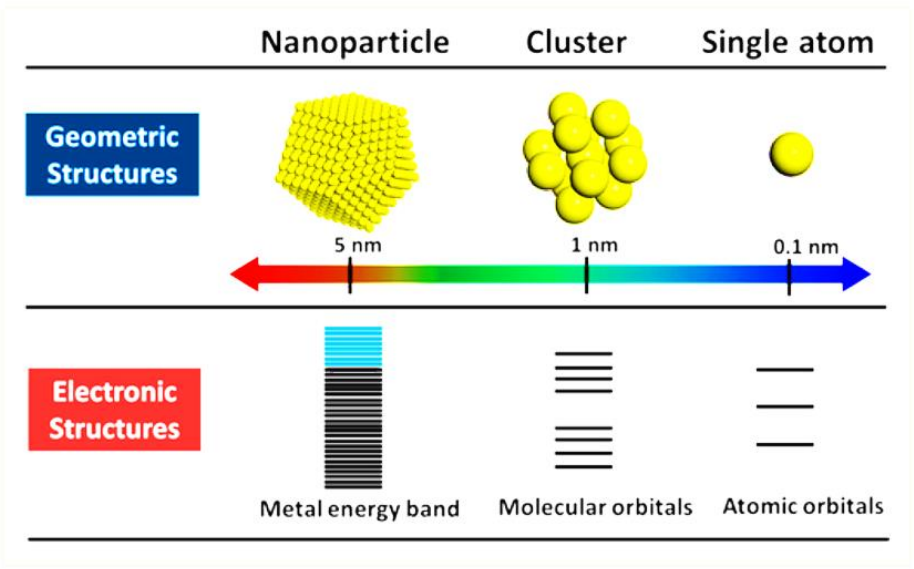

Figure 1.9 Geometric and electronic structures of single atom, clusters, and nanoparticles [76].

1.4.2 Band-gap engineering

Dion-Jacobson (DJ) layered perovskite was inspected for hydrogen evolution capability in this dissertation. It consists of layers of BO_6 octahedra linked at corners and separated by layers of alkali A' cations (Cs^+, Rb^+, and K^+) [77]. The crystals with perovskite slabs and flexible interlayer galleries provide distinctive electronic and catalytic properties, making them promising candidates for energy conversion in catalyst applications. Even though DJ-based layered perovskite photocatalysts' gap energies are in the ultraviolet region, the tendency of the layered perovskite to chemical substitution and flexible interlayer structure allows for reducing the band gap energy to the visible region [78]. N-

chemical substitution is a powerful strategy for tuning the band energy in layered perovskites [49]. This substitution involves incorporating nitrogen atoms, a precursor containing elements like ammonia, urea, and melamine, into the layered perovskite structure during high-temperature calcination to produce oxynitrides compounds [79], [80].

Many studies show that these compounds provide photocatalytic H_2 production by splitting water in visible light. Some of them are as follows. Kulischow et al. displayed that nitrogen doping performed using ammonia contributes to a decrease in band gaps of doped $AB_2Nb_3O_{10}$ compounds (A = Cs, Rb, K; B = Ca, Sr) down to 2.5 eV and moves to the higher wavelength in absorption. The best photocatalytic H_2 production under simulated solar irradiation among these compounds was found in $HCa_2Nb_3O_{10-x}N_x$ derived from $RbCa_2Nb_3O_{10-x}N_x$ with up to 40 µmol/h [81]. Lv et al. synthesized nitrogen-doped perovskite nanosheets (NSs) denoted as $(TBA)^{+|}LaTa_2O_{7-x}N_x]^-$. These NSs exhibit powerful photocatalytic performance for water splitting to produce hydrogen and oxygen, with a 4-fold and 8-fold higher production than bulk $RbLaTa_2O_{7-x}N_x$.

Additionally, the band gap decreases from 4.26 to 2.09 eV after nitrogen doping, maintaining activity even with photon wavelengths up to 600 nm [50]. Kawashima et al. synthesized protonated lanthanum titanium oxide, $H_2La_2Ti_3O_{10}$, and oxynitride, $H_2La_2Ti_3O_{10-3/2x}N_x$, crystals from the oxide, nitride, and deoxidized layered $K_2La_2Ti_3O_{10}$ crystals. Although partial nitridation and reoxidation resulted in a noticeable change in absorption wavelength at about 449–460 nm and band gap energy of $K_2La_2Ti_3O_{10}$ crystals, their crystal structure and morphology were maintained [36]. It has been demonstrated that the structure remains unchanged, yet the electronic properties undergo a modification.

As mentioned in the above articles, due to shrinking band gap energy, the DJ (oxy)nitride compounds containing Ti^{4+}, $Nb^{5+,}$ and Ta^{5+} have absorption edges of 450 to 650 nm [82]. The increase in the visible-light region can be attributed to two factors: The first factor is partially replacing nitrogen with oxygen. This creates new orbitals by combining oxygen's 2p orbitals with nitrogen's 2p orbitals, and these new orbitals shift the valence band upwards. The second factor is the formation of an isolated N 2p narrow band above the O 2p valence band within the forbidden band because of the absorption of interstitial nitrogen impurities [36]. Figure 1.10 compares the schematic representation of the oxide-

based electronic structure and (oxy)nitride-based electronic structure. Bandgap engineering refers to manipulating the energy difference between the valence and conduction bands in a material to control its light absorption properties [83].

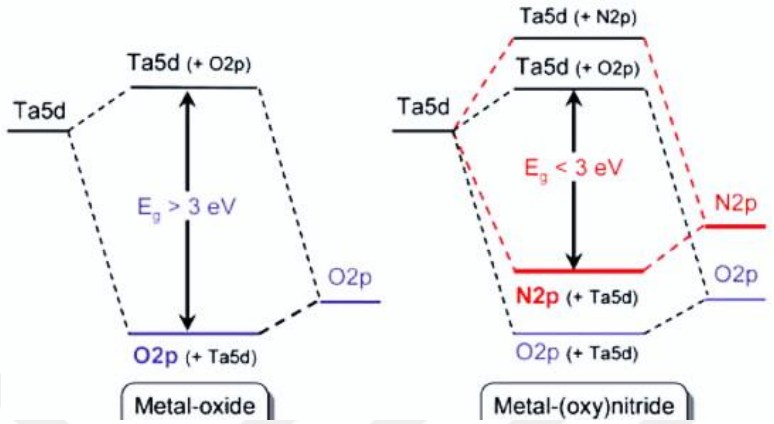

Figure 1.10 Schematic representation of electronic energy band positions of a metal oxide and metal (oxy)nitride [84].

1.4.3 Exfoliation of layered perovskites

Layered DJ-based perovskite materials have flexible interlayers that enable the generation of nanosheet morphology. Its structure consists of solid covalent or ionic bonds within each layer and van der Waals (vdW) bonding between the layers to create a robust and well-defined 3D structure for each sheet. These bonds ensure the integrity and stability of the material within each layer. However, the vdW interaction allows facile exfoliation by using exfoliation of the solid's dispersion in a solvent with the appropriate surface tension or intercalation of molecules/atoms and subsequent agitation (such as shear or ultrasonication) of the intercalated material [85]. Exfoliation is essential to generating specific surface area and atomic thickness layers.

On the one hand, the higher the surface area, the more active the sites. In addition, the ultrathin layers provide the shortening migration distance. In this way, most bulk recombination can be prevented, improving performance. In other words, these 2D materials, characterized by submicron lateral dimensions and atomic-scale thickness, exhibit superior photocatalytic characteristics and excellent charge separation, minimizing recombination chances compared to their bulk counterparts (See **Figure 1.11** for reference) [60].

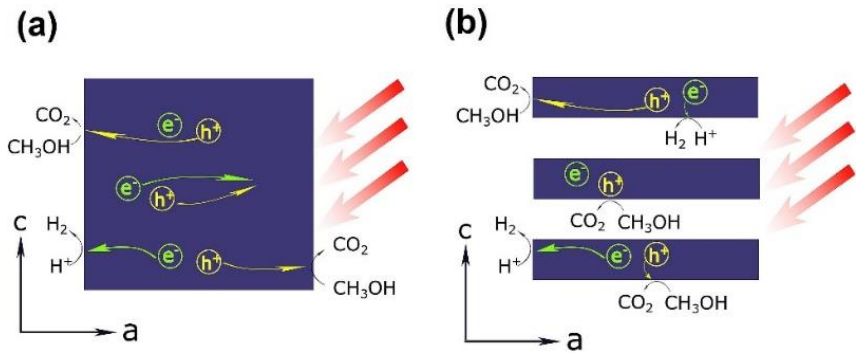

Figure 1.11 Schematic illustrations of the mechanisms involved in photocatalytic hydrogen evolution from methanol solution over **(a)** non-layered materials and **(b)** layered perovskites.

Layered perovskite NSs have attracted attention to applications in water-splitting processes for two decades due to the properties mentioned above. For example, studies have shown that nanosheets derived from $Ca_2Nb_3O_{10}$ [86], [87], $HCa_2Nb_3O_{10}$ [88], $HSr_2Nb_3O_{10}$ [89], $HLaNb_2O_7$ [90], and $KCa_2Nb_{3-x}Rh_xO_{10-\delta}$ [91] exhibit greater photocatalytic efficiency compared to their original compounds. The performance-enhancing properties of this modification have been previously elucidated; this section will now present information regarding exfoliation techniques. Treacy et al. discovered that intercalating large groups like tetrabutylammonium (TBA^+) can expand the interlayer space of layered perovskites, resulting in the formation of colloidal nanosheets [92]. Layered perovskite nanosheet is based on the sequential execution of several reactions in liquid-phase chemical exfoliation. Sequential ion exchange and ultrasonic exfoliation of bulk materials into nanosheets are shown in Figure 1.12 [40].

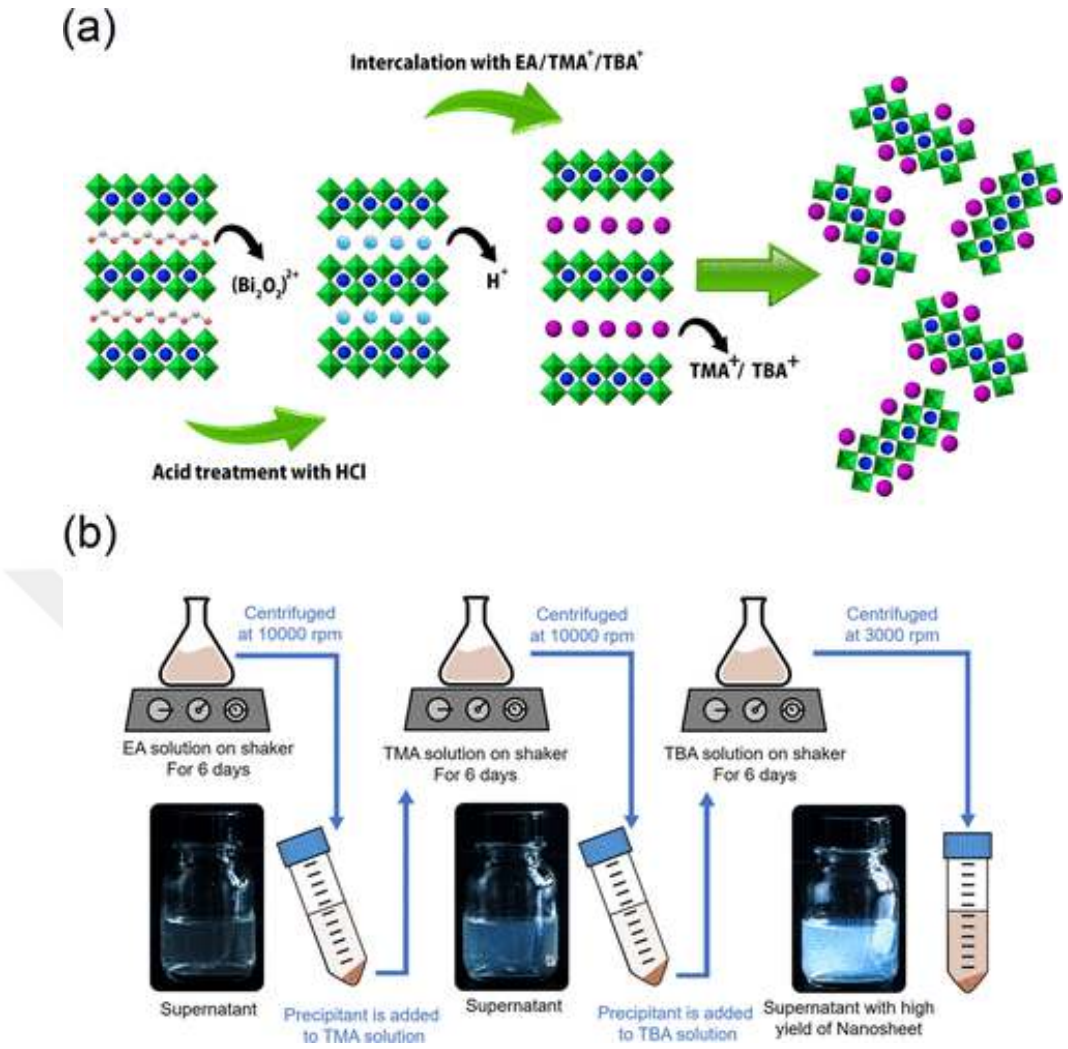

Figure 1.12 (a) Sequential mechanism protonation, intercalation, and exfoliation to produce nanosheets from bulk materials **(b)** Schematic of the three-step exfoliation procedures [40].

The molecular structure of the exfoliators, including the number of hydrophilic groups, and the methods of the delamination process are critical factors for exfoliation. These factors must be considered in order to achieve successful delamination. Especially, a layered structure with a highly hydrophilic interlayer space consisting of polar groups behaves like a Brønsted–Lowry acid, quickly reacting with a base in the environment to conduct an acid-base reaction, thus allowing the formation of a colloidal solution, and the strong hydration repulsion plays a dominant role in colloidal stability [93]. Some layered structures have high charge density between perovskite slabs; therefore, more energy is required to exfoliate these structures. In order to overcome the strong Coulomb force, it

is necessary to optimize the exfoliation process of the layered material by attempting various factors, including the use of different exfoliating agents, varying the ratios between hydrophilic molecules and organic base molecules, adjusting the temperature, and modifying the exfoliation process [94]. This chapter provides information to help improve our understanding of layered materials' exfoliation mechanisms and investigate their effects on photocatalytic performance.

Chapter 2: Synthesis and Characterization Methods

2.1 Synthesized Methods of Powder Tantalates for Photocatalysis

2.1.1 Synthesis of powders with Pechini method:

All used chemicals were purchased in analytical grade and not further purified. Pure $CsLaTa_2O_7$ (CLTO) and $CsCa_2Ta_3O_{10}$ (CCTO) and their modification Pd (1.5, 3, and 5%) and Sn (0.75, 1.5, 3, 5%) doped in Ta site of CLTO and CCTO were synthesized by polymerized complex method (PCM), which relies on ethylene glycol polymerization of metal citrates [95]. The starting chemicals are Cs_2CO_3 (99.99%, Sigma Aldrich), Ca $(NO_3)_2.4H_2O$ or La $(NO_3).6H_2O$ (analysis EMSURE® ACS, Sigma Aldrich), $TaCl_5$ (99.98%, Sigma Aldrich), citric acid (CA) (98%, Sigma Aldrich), ethylene glycol (99%, Sigma Aldrich), methanol (99.8%, Sigma Aldrich). The doped chemicals are $PdCl_2$ (99.99%, Sigma Aldrich) and $SnCl_2$ (99.99%, Sigma Aldrich). The PC synthesis was made shortly as follows as it is given in Figure 2.1: First, $TaCl_5$ and citric acid (Ta: CA=10:1) were dissolved in methanol, then in stoichiometric ratios, respectively, Ca $(NO_3)_2.4H_2O$ or La $(NO_3)_3 \cdot 6H_2O$, Cs_2CO_3 (20% excess amount). Finally, ethylene glycol (40 mL) was added as a film generation agent. When Pd or Sn were added as dopant materials, a methanol solution was added immediately after Ta was added. All chemicals were stirred for one hour at room temperature to obtain a transparent homogeneous solution. Afterward, the mixture was stirred at 80°C for three hours until it became more transparent, containing metal ion and citric acid complexes. It was heated at 150±5°C for two hours to remove excess solvents and promote polymerization. Heating at 150±5°C caused the ethylene glycol odor to disappear, and the solution became viscous with a change of color from colorless to deep yellow but without any visible formation precipitation. A resin was pyrolyzed at 400±5°C for 3 hours, resulting in a black solid mass. This was ground into powder using a glass rod and subsequently ground in agate mortar. The black powder was called precursor hereafter. The powder precursor was heated at 550°C for 5 hours in static air on an alumina crucible. Then the resulting powders were calcinated at 1000°C for 5 hours (heated 5°C/min, cooled naturally).

2.1.2 Synthesis of oxynitride powders:

In order to produce an oxynitrate powder, the pristine phase was placed in the center of the horizontal furnace. The calcination conditions at the furnace required to produce oxynitride powder were as follows. It was created by allowing ammonia gases (99.99%, SERVITRAX) to flow at 100 mL/min (99.99%, Servitrax) for 5 hours (20℃/min) at 1073K.

2.1.3 Proton exchange and exfoliation reactions:

The cesium ions in the 0,8 grams of layered oxide or oxynitride materials were substituted with protons through acid exchange using 250 mL of 3 M HCl solution for a week, with the acid solution being replaced daily. Following the proton exchange, the powder was repeatedly rinsed with clean water using centrifugation until the pH reached up to 7. The protonated powder dried at room temperature. The protonated form was stirred in a solution of 100 mL of a 1.0 M ethylamine (EA) (70 wt.% in water, Sigma Aldrich) for seven days, followed by two weeks of starting in a solution of 150 mL of a 0.025 M tetrabutylphosphonium hydroxide (TBPOH) (40 wt.% in water, Sigma Aldrich) to exfoliate colloidal solution nanosheets. During the two-week TBPOH mixing phase, care was taken to ensure that the mixture completed 36 hours of sonication. After this process, the unexfoliated powder was separated by centrifuging at 1000 rpm for 10 min to obtain nanosheet colloids. The resulting nanosheet colloids were restacked by adding 2.5M HCl to form precipitates. This solid was then rinsed several times with pure water to remove residual TBA^+, Cl^- and HCl, followed by freeze-drying, which eliminates water or other solvents in nanosheet powder from a frozen product through a process known as sublimation, in an oven between -34° and -45°C. After all these processes, the nanosheet was ready for use. All synthesized examples in the thesis are labeled as indicated in Table 2.1 below.

Table 2.1 Codes of all synthesized powders

Sample	**Label**
$CsCa_2Ta_3O10$	CCTO
$HCa_2Ta_3O_{10}$	HCTO

$[Ca_2Ta_3O_{10}]^-$	CTO
$CsCa_2Ta_3O_{10-y}N_y$	CCTOx
$HCa_2Ta_3O_{10-y}N_y$	HCTOx
$[Ca_2Ta_3\ O_{10-y}N_y]^-$	CTOx
1.5%Pd-$CsCa_2Ta_3O10$	1.5%Pd-CCTO
1.5%Pd-$HCa_2Ta_3O_{10}$	1.5%Pd-HCTO
1.5%Pd- $[Ca_2Ta_3O_{10}]^-$	1.5%Pd-CTO
3%Pd-$CsCa_2Ta_3O10$	3%Pd-CCTO
3%Pd-$HCa_2Ta_3O_{10}$	3%Pd-HCTO
3%Pd- $[Ca_2Ta_3O_{10}]^-$	3%Pd-CTO
5%Pd-$CsCa_2Ta_3O10$	5%Pd-CCTO
5%Pd-$HCa_2Ta_3O_{10}$	5%Pd-HCTO
5%Pd- $[Ca_2Ta_3O_{10}]^-$	5%Pd-CTO
1.5%Pd-$CsCa_2Ta_3\ O_{10-y}N_y$	1.5%Pd-CCTOx
1.5%Pd-$HCa_2Ta_3\ O_{10-y}N_y$	1.5%Pd-HCTOx
1.5%Pd- $[Ca_2Ta_3\ O_{10-y}N_y]^-$	1.5%Pd-CTOx
$CsLaTa_2O_7$	CLTO
H $LaTa_2O_7$	HLTO
$[LaTa_2O_7]^-$	LTO
$CsLaTa_2O_{7-y}N_y$	CLTOx
$HLaTa_2O_{7-y}N_y$	HLTOx
$[LaTa_2O_{7-y}N_y]^-$	LTOx
1.5%Pd- $CsLaTa_2O_7$	1.5%Pd-CLTO
1.5%Pd- $HLaTa_2O_7$	1.5%Pd-HLTO
1.5%Pd- $[LaTa_2O_7]^-$	1.5%Pd-CLO
3%Pd- $CsLaTa_2O_7$	3%Pd-CLTO
3%Pd- $HLaTa_2O_7$	3%Pd-HLTO
3%Pd- $[LaTa_2O_7]^-$	3%Pd-CLO
5%Pd-$CsCa_2Ta_3O10$	5%Pd-CLTO
5%Pd-$HCa_2Ta_3O_{10}$	5%Pd-HLTO
5%Pd- $[Ca_2Ta_3O_{10}]^-$	5%Pd-CLO
1.5%Pd- $CsLaTa_2O_{7-y}N_y$	1.5%Pd-CLTOx

1.5%Pd- $CsLaTa_2O_{7-y}N_y$	1.5%Pd-HLTOx
1.5%Pd- $[LaTa_2O_{7-y}N_y]^-$	1.5%Pd-LTOx
0,75%Sn- $CsLaTa_2O_7$	0.75%Sn-CLTO
0,75%Sn- $HLaTa_2O_7$	0.75%Sn-HLTO
0,75%Sn- $[LaTa_2O_7]^-$	0.75%Sn-LTO
1.5%Sn- $CsLaTa_2O_7$	1.5%Sn-CLTO
1.5%Sn- $HLaTa_2O_7$	1.5%Sn-HLTO
1.5%Sn- $[LaTa_2O_7]^-$	1.5%Sn-CLO
3%Sn- $CsLaTa_2O_7$	3%Sn-CLTO
3%Sn- $HLaTa_2O_7$	3%Sn-HLTO
3%Sn- $[LaTa_2O_7]^-$	3%Sn-CLO
5%Sn- $CsLaTa_2O_7$	5%Sn-CLTO
5%Sn- $HLaTa_2O_7$	5%Sn-HLTO
5%Sn- $[LaTa_2O_7]^-$	5%SnCLO

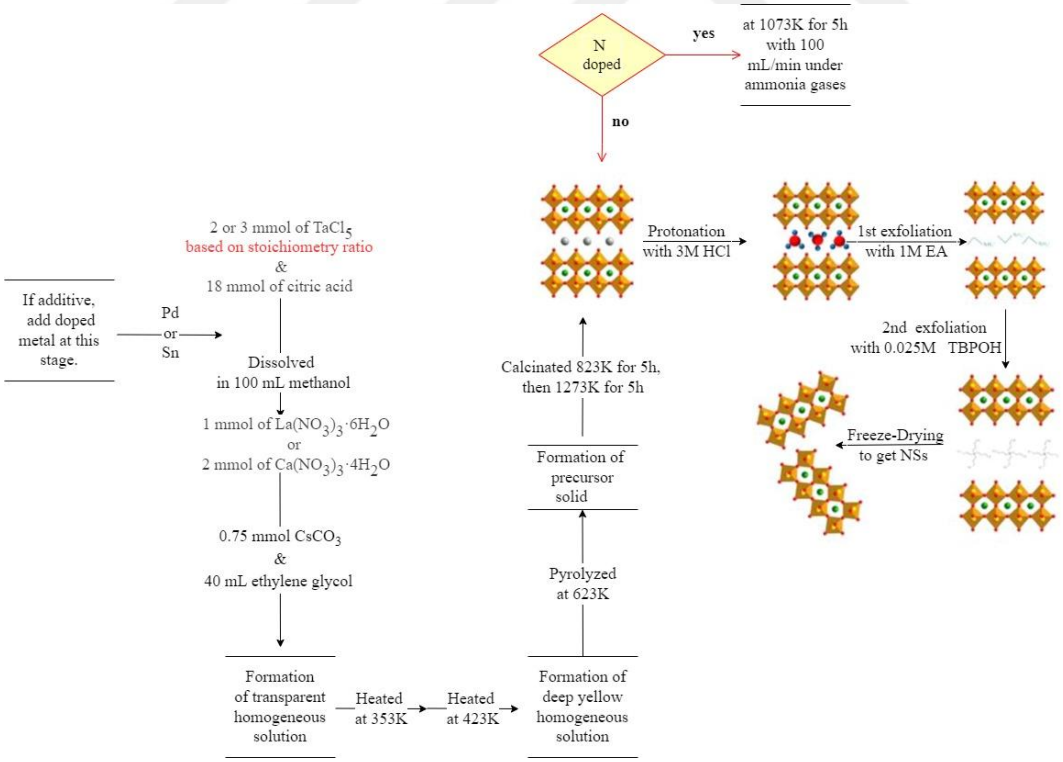

Figure 2.1 Scheme of synthesis of DJ type layered perovskite oxide nanosheet.

2.2 Physical and Chemical Characterization Methods

This chapter presents a synopsis of diverse experiments, characterization methods, and the underlying theory essential for comprehending the measurements conducted for powder material.

2.2.1 X-ray Diffraction (XRD)

X-ray diffractometer (XRD) investigates the crystalline phase, chemical composition, lattice parameters, crystalline size, shape impurity, and the presence of doping elements in the crystal lattices of the photocatalyst system [96]. Crystallographic structures of synthesized materials were determined by XRD (Rigaku Mini Flex 600; Cu Kα (λ = 1.5418 Å)) with a scanning rate of 10°/min operating at 40 kV/15 mA. X-ray diffraction spectra were recorded in the 2θ range of 5° to 60°. A zero-background powder specimen holder was employed for the XRD analysis of all samples.

2.2.2 Raman Spectroscopy

Raman spectroscopy is used for structural analysis, phase identification, chemical characterization, and identification of chemical functional groups and molecular species detected in layered perovskite photocatalysis [97]. Raman spectroscopy was carried out using a Renishaw INVIA spectrometer with a 633 nm initial excitation laser (%5 laser power, 20 exposure time) for synthesized materials.

2.2.3 Ultraviolet-visible (UV-vis) Diffuse Reflectance Spectroscopy (DRS)

UV-vis diffuse reflectance spectroscopy (UV-vis DRS) is a technique used to calculate the electronic band structure of photocatalytic systems. This technique probes the material's response to electromagnetic radiation within the ultraviolet-visible region (200-800 nm) by analyzing its light absorption and scattering properties. The Kubelka-Munk equation provides for interpreting the collected data and inferring the electronic structure of the photocatalyst [98]. In this dissertation, UV-vis DRS were conducted on Shimadzu UV-3600 – UV-Vis-Nir Spectrophotometer in the 220–800 nm range using barium sulfate as an external reference with reflection coefficient R = 1. The reflectance spectra were transformed into coordinates $(Fh\nu)^{1/2} = f(h\nu)$, where $F = (1-R)^2/2R$ is the Kubelka-

Munk function[99]. Linear sections of the graph were extrapolated, and an optical bandgap energy E_g was found as an abscissa of their intersection point.

2.2.4 X-ray Photoelectron Spectroscopy (XPS)

X-ray photoelectron spectroscopy (XPS) is a surface-sensitive technique that uses photons from an X-ray source to excite atoms near the surface of a solid. The ejected electrons are collected and measured by a hemispherical electron energy analyzer. The kinetic energy of these electrons indicates their binding energy, allowing for the identification of the element and the specific core level of the electron [100]. X-ray photoelectron spectroscopy (XPS) measurements were characterized with a Thermo Scientific K-Alpha instrument using Al Kα ($h\nu$ = 1486.6 eV) radiation for the synthesized photocatalyst. The XPS data acquired was deconvoluted using Thermo Avantage v5.973. The binding energies (BE) position was calibrated using the C 1s peak (284.4 eV).

2.2.5 Inductively Coupled Plasma Mass Spectrometry (ICP-MS)

Inductively Coupled Plasma-Mass Spectrometry (ICP-MS) uses an intense heat source (plasma) to break down a sample and ionize its elements. It then analyzes these ions using a mass spectrometer to determine their composition [101]. ICP-MS is well-suited for measuring trace elements like dopant cations (positively charged ions) and their ratios within a sample [102]. ICP-MS analysis verified the successful incorporation of palladium into the perovskite lattice (or crystal structure) and quantified the doping level. This technique is susceptible and can detect dopant cations at concentrations as low as parts per billion (ppb) within the material.

This thesis employed ICP-MS using an Agilent 7700x instrument to determine the amount of palladium incorporated into the layered perovskite material. The perovskite samples were first digested in a mixture of aqua regia (10 mL) using a Start D Milestone Microwave Digestion system. Following digestion, the samples were diluted with a 2% v/v HNO_3 solution.

ICP-MS is a more reliable method for quantifying the actual weight percent of Pd because it can accurately measure tiny amounts of precious metals, even in complex samples.

2.2.6 Scanning Electron Microscopy (SEM)

Electron microscopy is used to study the structure and morphology of materials at the nanoscale [103]. It allows researchers to visualize the size, shape, and arrangement of catalyst particles or structures for photocatalysts.

Scanning Electron Microscopy (SEM) is a powerful technique for studying a sample's morphology, including size, shape, and surface features. It utilizes a focused beam of high-energy electrons (typically 0.5-30 keV) to scan the sample's surface. The interaction of these electrons with the sample generates various signals, including:

Secondary Electrons: Provide detailed information about the sample's topography due to their interaction with the surface features.

Backscattered Electrons: Offer information about the elemental distribution within the sample based on the average atomic number of elements present. While this can give some clues about the chemical composition, a more precise technique like Energy-dispersive X-ray spectroscopy (EDX) is often used with SEM for a more comprehensive elemental analysis. SEM micrographs have a large depth of field, providing a three-dimensional appearance of the sample's surface [104].

This thesis used SEM to investigate layered bulk materials' morphology and platelet size, cation-proton exchanged materials, and restacked nanosheets. This thesis used SEM to investigate layered bulk materials' morphology and plate size, cation-proton exchanged materials, and restacked nanosheets. The field-emission-type scanning electron microscopy (FESEM) images were analyzed using a Zeiss Ultra Plus field emission scanning microscope with 200.00 KX magnification and 5.00 kV.

2.2.7 The Brunauer-Emmett-Teller (BET) analysis

The Brunauer-Emmett-Teller (BET) analysis is an essential analytical technique. BET theory explains the phenomenon of physical adsorption, where gas molecules form weak vdW interactions with a solid surface. The measured quantity in BET represents the sample's total surface area per unit mass [105]. BET method was used to calculate the specific surface area of bulk and nanosheet materials using N_2 adsorption-desorption

measurement on Micromeritics ASAP 2020 HD in the dissertation. Before measurements, powders were degassed at 373 K under vacuum overnight.

2.3 Film Preparation

Two distinct synthesis methodologies were utilized to fabricate tantalate-based photoelectrodes. The first method was that bulk photocatalysts were coated on fluorine-doped tin oxide (FTO) on a conductive glass side by a spin-coated instrument. The second method was the coating method of nanosheet materials on FTO, taking into account the work done by Shi et al. [106]. A detailed explanation of the first verification method is given in the paragraph below.

2.3.1 Films from powders

Substrate materials were selected from fluorine-doped tin oxide (FTO) glasses and cut with 25 x 10 mm dimensions. FTOs were meticulously cleaned through sonication with acetone and ethanol, followed by deionized water (DI). The ingredients of the coating solution were 20 mg of the photocatalyst, 40 µL terpineol, 40 µL acetylacetone, 80 µL ethylene glycol, and 1 mL ethyl alcohol. The solution was dispersed in 1 mL of DI and 1 mL of ethanol and then stirred for 1h for a homogeneous mixture. 100 µL of this mixture was drop-cast onto the FTO substrate and spread evenly using a spin-coater at 500 rpm for 5 seconds, followed by 3000 rpm for 30 seconds. The coated sample was then calcinated at 400°C for 60 minutes in air.

2.3.2 Films from nanosheets

The coating procedure was performed considering the single drop approach in the article by Shi et al. [106]. This single-dropped coating method is followed by preheating the substrates on a hot plate at 100–120°C for 3 minutes, facilitating rapid solution evaporation and film formation. 40 µL of the synthesized nanosheet suspension was diluted into 200 µL of ethanol as the precursor suspension was used for film deposition. 100µL of this mixture was dropped on a hot FTO glass. Then, the mixture was meticulously taken from its center using a pipette. Finally, the prepared film was dried using Ar gases. The coating method is shown in Figure 2.2.

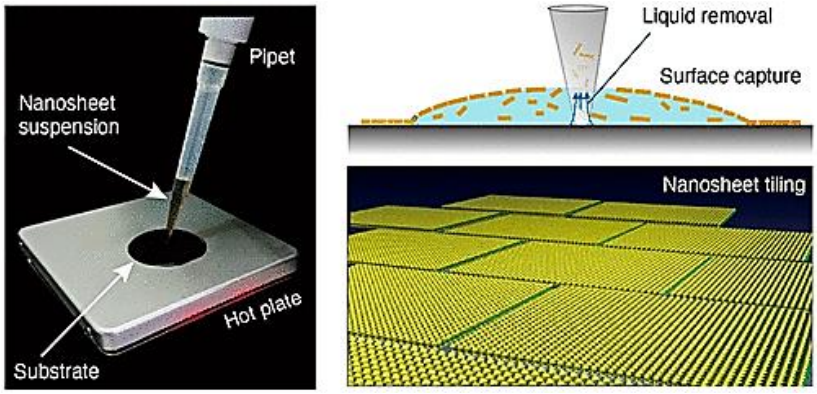

Figure 2.2 Single droplet assembly for 2D nanosheet tiling [106].

2.4 Electrochemical and Photoelectrochemical Characterization Methods of Photoelectrode

The PEC measurements were conducted using the working electrode (W.E.), counter electrode (C.E.), and reference electrode (R.E.), which comprise three electrode systems as illustrated in Figure 2.3. The synthesized photoelectrode, 10 mm x 10 mm Pt wire, and vs. SCE (sat'ed KCl) are working, counter, and reference electrodes in the thesis. Nitrogen gas was bubbled to electrolyte solutions (0.5M K_2SO_4 including 5% methanol) to eliminate dissolved oxygen before PEC analysis for at least 15 min. The N_2 was continuously purged in the solution to ensure oxygen did not re-enter the solution throughout the analysis. Chronoamperometry (CA) and Potentiostatic Electrochemical Impedance Spectroscopy (PEIS) were valuable techniques used to analyze the behavior of photoelectrodes in PEC studies in this dissertation.

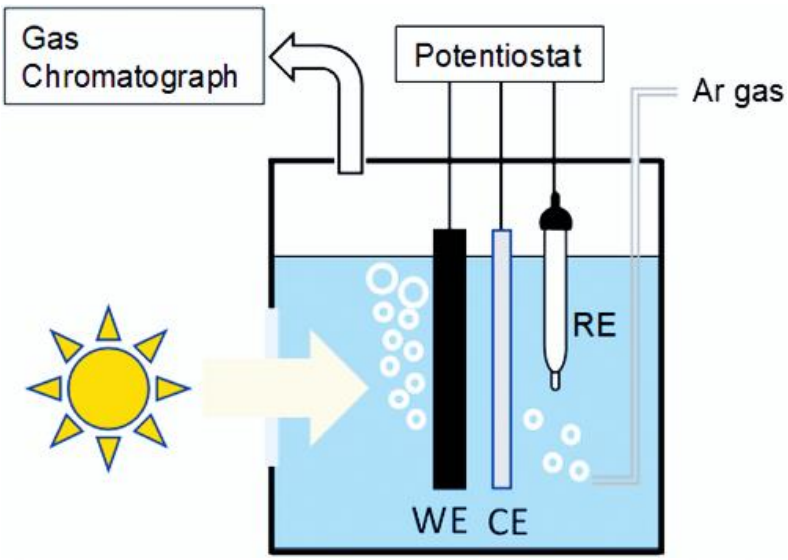

Figure 2.3 Schematic of three electrode systems for PEC [107]

2.4.1 Chronoamperometry (CA)

Chronoamperometry (CA) measures the current of a photoelectrode over time, used in PEC analysis to evaluate photocurrent stability and investigate electron transfer processes, providing insights into the photoelectrode's performance under light at constant voltage [108]. CA measurements were performed under chopped illumination (20s on/off cycles) using a potentiostat (Princeton Applied Research Versa STAT MC) at a fixed potential of 1 V (vs. SCE). The light source was used by a strong Xenon lamp (300 watts) made by Newport (model 66901). The electrolyte solution is 0.5M of K_2SO_4 (including %2.5 methanol).

2.4.2 Potentiostatic Electrochemical Impedance Spectroscopy (PEIS)

Potentiostatic Electrochemical Impedance Spectroscopy (PEIS) is commonly utilized in photoelectrochemical (PEC) studies to evaluate electrochemical behavior occurring at the photoelectrode/electrolyte. PEIS works by applying a small AC voltage at variable frequencies and measuring the current response of the system. The resulting data is analyzed through graphical representations called Nyquist or Bode diagrams. Nyquist analysis visually represents the impedance at the electrode interface across various frequencies. It separates the impedance into its real and imaginary components. The real part is associated with resistance and electron transfer processes, while the imaginary part reflects various reactive processes at the interface, including double-layer capacitance.

On the other hand, Bode analysis presents the impedance data in two separate plots: a magnitude plot showing the absolute value of impedance versus frequency and a phase plot showing the phase shift between the applied voltage and the resulting current [109]. By analyzing these plots, researchers can gain insights into the frequency dependence of the system's response. In the phase plot, the peak observed at an intermediate frequency range could be associated with the lifetime of electrons within the photoanode material [110]. On the other hand, the radius of the arc on the Nyquist plot corresponds to the charge transfer rate at the interface between the photoelectrode and the electrolyte. A smaller arc radius indicates a higher efficiency in photoinduced charge transfer [111]. Nyquist plot EIS measurements were conducted from 10^3 to 10^{-2} Hz with 0.01 mV amplitude at 1V vs Hg/HgO (1M KOH) in 0,5M K_2SO_4.

2.5 Photocatalytic Hydrogen Production

The range of 5-15 mg of photocatalyst and 5 mL of the methanol-water mixture (10% volume methanol) were placed into a quartz vessel with a total volume of 10 mL with rubber two stoppers to generate an inert medium. These stoppers created an inert atmosphere during the HER experiment. Before the HER measurement, the mixture in the quartz cell was sonicated for 30 min to get homogenous dispersion. Then, the vessel was purged using argon (50 mL/min) for at least 20 minutes to remove air inside. After that, Ar flow (20 mL/min) was placed between these two stoppers to prevent air from entering the cell. A foam test was applied to the gas outlet to check whether the Ar flow was between two stoppers. The experimental setup employed a horizontal illumination system with a 300 W xenon light source (Newport, 66901), as illustrated in Figure 2.4. The light source was operated with or without an AM 1.5 filter. The vessel containing the solution was stirred at 200 rpm. The experiment proceeded over a five-hour timeframe. Every hour, a sample was extracted from the cell's headspace using a 100 µL gas-tight syringe (A needle - series H, ISOLAB) for injection into the gas chromatograph (Shimadzu, GC-2014).

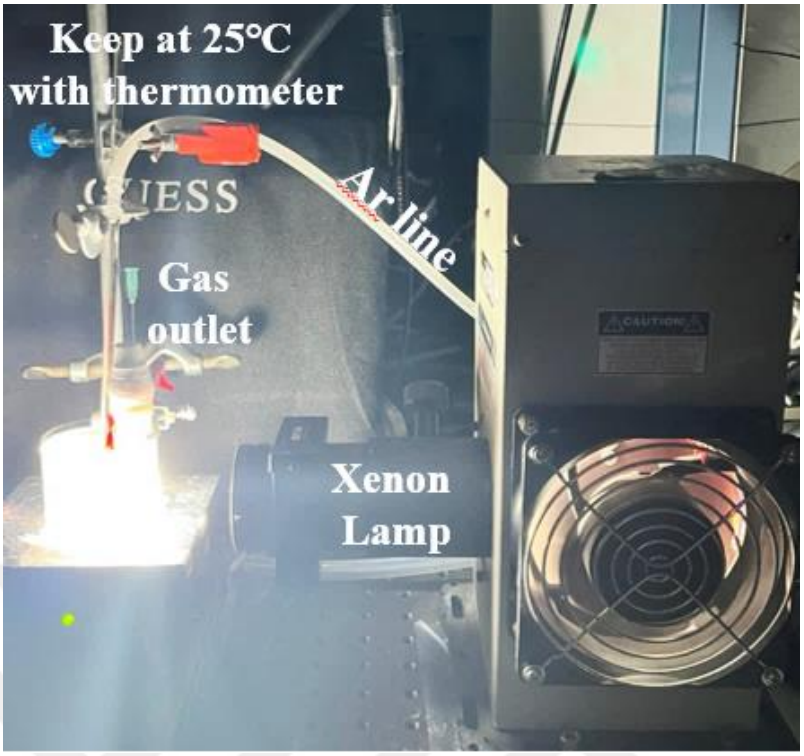

Figure 2.4 Experimental setup.

The inlet temperature of GC and thermal conductivity detector (TCD) was at 150 °C with a bridge current of 40 mA, while the temperature of the MS 5A column (Technorama, NF-38427-FS) was set at 65 °C. A 10 mL cell containing 5 mL of water was used for hydrogen (H_2) calibration within a gas chromatograph (GC). Controlled volumes of H_2 gas, ranging from 10 to 100 µL with 10 µL increments, were injected into the GC system, and peak areas were correlated with the injected quantities to establish a calibration curve. This curve allows for converting peak area from GC analysis of unknown samples into the corresponding amount of H_2 present. The ideal gas equation was used to convert peak areas to moles of H_2, considering a headspace volume of 5 mL. The calibration curve in Figure 2.5 was used to quantitatively determine H_2 based on peak area in GC measurements.

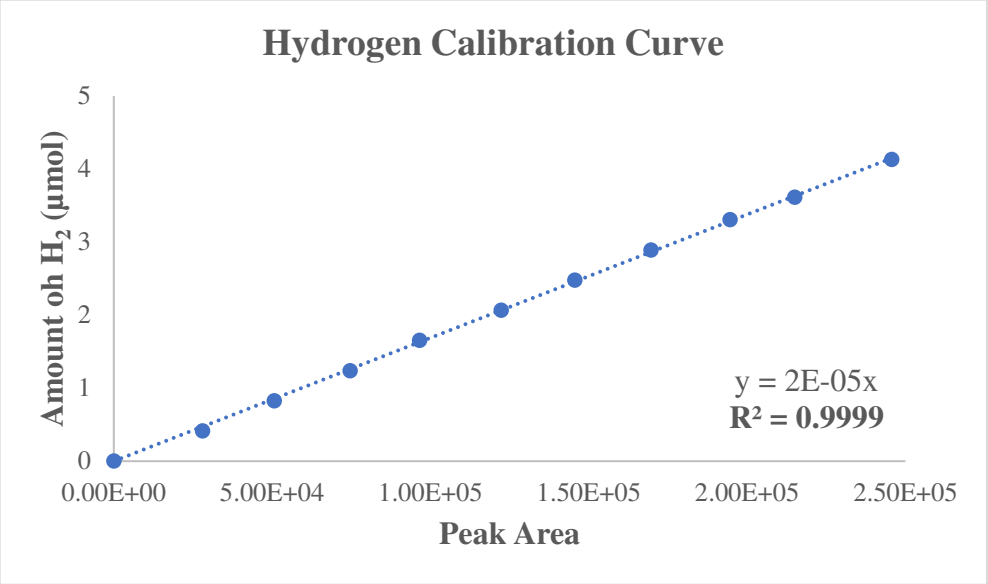

Figure 2.5 Hydrogen calibration curve.

Chapter 3: Comparison of Two and Three-Layer Tantalum-Based Oxynitrides for Photocatalytic Hydrogen Evolution

3.1 Introduction

Layered perovskites are extensively researched for splitting applications as photocatalysts because their slabs and flexible interlayer galleries have unique electronic and catalytic properties. Most studies focus on the A-site or B-site cation exchange for new phase preparation. However, little information on the layer number factor has been documented, which affects performance. One common approach to improving the activity of layered perovskites involves manipulating the cations between the layers and producing nanosheet powder. The former strategy often involves exchanging protons (H^+) with other cations, such as Cs^+ and Rb^+ between the layers. Notably, the latter approach is most effective when applied to 2D perovskite powders derived from bulk materials. While possessing outstanding characteristics for catalytic purposes, their primary limitation arises from the lack of active work in the visible region due to their band energies exceeding 3 eV [112].

Consequently, various techniques have been investigated to enhance the response of pristine metal oxide photocatalysts to visible light. Among these techniques, nitrogen doping introduces new electronic states within the perovskite's bandgap, thereby enabling visible light absorption. This, in turn, facilitates the utilization of these perovskites in visible-light-driven catalysis applications. [113]. In 2012, S. Ida et al. published a paper [49] about the effect of exfoliation of a Layered Oxynitride for photocatalytic hydrogen evolution. The researchers fabricated ultra-thin sheets of calcium tantalum oxynitride, which show improved hydrogen gas generation (0.10 μmol/h) from water under visible light but low performance with even methanol. When loaded with rhodium, they produce hydrogen (156.1 μmol/h) and oxygen gases under ultraviolet light dramatically compared to non-modified ones. In 2017, M. Lv et al. published a paper [50] on photocatalytic water splitting with Lanthanum Tantalate Perovskite Nanosheets. The atomic thickness of nanosheets is synthesized via exfoliation from its pristine state. These NSs showed superior photocatalytic activities for water splitting, with a quantum efficiency of 1.29% and 3.27% under visible-light illumination, significantly higher than bulk structure. In 2020, Y. Tang et al. published a paper [114] on synthesizing a three-layer oxynitride

perovskite of $K_2Ca_2Ta_3O_9N \cdot 2H_2O$ and compares its photocatalytic activity with a two-layer perovskite. Three-layer oxynitride perovskite of $K_2Ca_2Ta_3O_9N \cdot 2H_2O$, a single-phase layered perovskite with an absorption edge of around 460 nm and an estimated band gap of around 2.7 eV. The structure and light absorption properties remain unchanged. However, the material $K_2Ca_2Ta_3O_9N \cdot 2H_2O$ produced significantly less hydrogen (H_2) gas and had a shorter lifetime compared to $K_2Ca_2Ta_3O_9N \cdot 1.6H_2O$, showing the effect of interlayer water in photocatalytic activity. In 2021, P. Wang reported [115] the synthesizes Dion-Jacobson layered perovskites, including $LaTaO_4$, $KLaTa_2O_7$, and $KCa_2Ta_3O_{10}$, with n values of 1, 2, and 3, respectively. Among these, $KLaTa_2O_7$ performs better than $KCa_2Ta_3O_{10}$ and $LaTaO_4$ in methanol under UV illumination. The researchers explained that positioning the conduction bands is the primary determinant affecting photocatalytic generation of hydrogen.

Considering the information mentioned above, N doping is one of the methods applied to make active catalysis in the visible region. When oxygen is substituted with nitrogen in the perovskite oxide lattice, nitrogen acts as a dopant. This substitution causes the creation of the new energy states at their forbidden energies by hybridizing the N 2p and O 2p orbitals to reduce the band energy, thereby moving their valance band position upward. This thesis section successfully synthesized tantalum-based oxynitride nanosheets (n=2 and n=3) through a two-step intercalation process. The aim was to investigate their photocatalytic H_2 efficiency in full spectrum and A.M. 1.5G light sources. In addition to photocatalytic, Photoelectrochemical properties were assessed in a three-electrode system. The combined results demonstrated that two layered tantalum-based Dion–Jacobson layered perovskites had higher hydrogen generation under both spectral conditions than others.

3.2 Experimental Procedure

The experimental part is explained in detail in chapter 2.

3.3 Result and Discussion

3.3.1 X-Ray diffraction Spectroscopy (XRD)

The identification of the crystal phases of the synthesized powders was performed by X-ray diffraction (XRD) (Figure 3.1). The black, red, and blue colors represent three pristine tantalum-based oxides (CCTO or HCTO), oxynitride (CCTOx or HCTOx), and Pd-doped oxynitride (1.5% Pd-CCTOx or1.5% Pd-HCTOx), subsequently. The gray, purple, and green colors represent two pristine tantalum-based oxides (CLTO or HLTO), oxynitride (CLTOx or HLTOx), and Pd-doped oxynitride (1.5% Pd-CLTOx or1.5% PD-HLTOx), respectively. The peaks are indexed as 5.79º (001), 11.59º (002), 17.43º (003), 29.99º (100), 23.31º (003), 23.72º (101), 25.82º (102), 28.99º (103), 29.25º (005), 32.73º (110), 32.97º (104), 33.27º (111), 34.84º (011), 35.27º (006), 35.27º (006), 37.32º (113), 37.52º (113), 40.57º (114), 41.4º (007), 42.52º (106), 44.46º (115), 46.97º (200), 47.37º (201), 47.66º (008), 47.88º (107), 48.55º (202), 48.88º (116) for three layered tantalum oxide in Figure 3.1.a according to the ICDD database [116]. The peaks are indexed as 7.95º (001), 22.89º (100), 24.02º (003), 24.27º (101), 28.02º (102), 32.22º (004), 32.59º (110), 33.42º (005), 32.97º (104), 33.27º (111), 34.84º (011), 35.27º (006), 35.27º (103), 33.60º (111), 36.48º (112), 39.89º (104), 40.58º (005), 40.89º (113), 46.48º (114), 46.76º (200), 47.10º (105), 47.51º (201), 49.18º (006), 49.72º (202), for two layered tantalum oxide in Figure 3.1.c. Analysis of the sample's diffraction peaks confirmed its structure as tetragonal symmetry, aligning with previously reported observations [49], [62]. No peaks corresponding to impurities were detected, indicating high material homogeneity, even after doping. However, there is a structural difference between a protonated compound and its parent compound. This difference arises due to a change in the crystallographic structure. Specifically, the space group, which defines the symmetry of the crystal lattice, changes from P4/mmm to I4/mmm [117]. This change in the space group signifies a different arrangement of atoms in the material than its parent compounds due to Cs^+ exchange with H^+. Although the in-plane (100) and (110) diffraction peaks are preserved due to the covalent solid bond in the layered structure after the proton exchange process, the (001) peak of two and three layered materials slightly shifts towards higher angles, showing that the interlayer space has been narrowed as a result of the substitution of Cs^+ ions with H^+ ions [$r(H^+) = -0.38$ Å and $r(Cs^+) = 1.65$ Å] as given in Figure 3.1.b and

Figure 3.1.d [118]. The absence of impurity peaks in the diffraction pattern and a perfect match to literature values strongly indicated the successful synthesis of a highly crystalline phase for all modified phases.

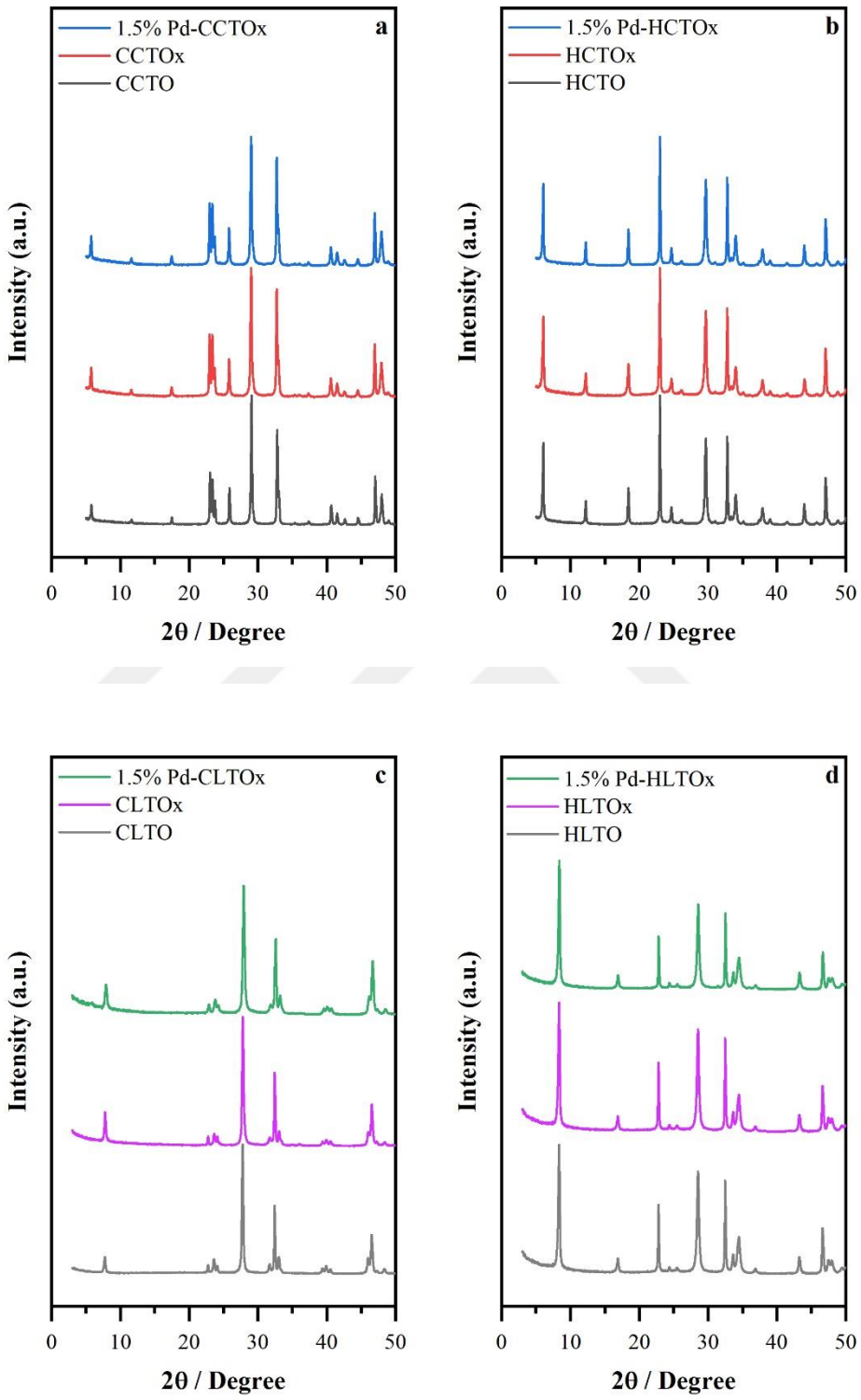

Figure 3.1 XRD patterns of **(a)** $CsCa_2Ta_3O_{10}$ (CCTO), **(b)** $HCa_2Ta_3O_{10}$ (HCTO), **(c)** $CsLaTa_2O_7$ (CLTO), and **(d)** $HLaTa_2O_7$ (HLTO) and their oxynitride version and Pd doped oxynitride version.

3.3.2 Raman Spectroscopy

Raman spectroscopy was employed to identify the structural variations, and the results are presented in Figure 3.2. The Raman spectra of both binary and ternary oxides (depicted in black) and oxynitride systems (illustrated in red) were found to align with prior findings in the literature [49]. Following nitridation, new peaks appeared in their Raman spectrum, highlighted by the dashed line in Figure 3.2. The new peaks observed after nitrogen treatment likely involve nitrogen atoms incorporated into the material's structure. These nitrogen atoms might partially convert some existing oxygen-tantalum structures (TaO_6) into new phases containing nitrogen ($TaO_{6-x}N_x$ or TaN_6). However, these new peaks disappeared when heated at 1073K, indicating they were related to the presence of nitrogen. In addition, there are three possible explanations for the observed peaks: (i) Vibrations caused by nitrogen atoms replacing other atoms within the crystal structure. (ii) Vibrations due to imperfections created to maintain electrical neutrality after nitrogen was incorporated. (iii) Vibrations originating from unexpected materials present in the sample. In the case of improper optimization of synthesis conditions during the nitridation process, a Ta_3N_5 impurity phase can be generated, as documented in the literature [49]. However, the absence of the Ta_3N_5 impurity phase in the XRD pattern of the oxynitride crystals proves that Ta^{+5} was not reduced to Ta^{+4}, supported by XPS analysis. Therefore, the new peaks observed are solely related to incorporating nitrogen into the desired CLTO and CCTO structures.

In addition, protonation caused a reduction of peak intensity at 930 cm^{-1} for CCTO and 920 cm^{-1} for CLTO in Figure 3.2.a and Figure 3.2.b bands, accompanied by a redshift in their spectra. These peaks correspond to the vibrational mode of the Ta–O terminal bond, which is notably sensitive to the presence of interlayer species. This sensitivity arises from protonation facilitating the exchange of H^+ with Cs^+ in the interlayer spacings [119].

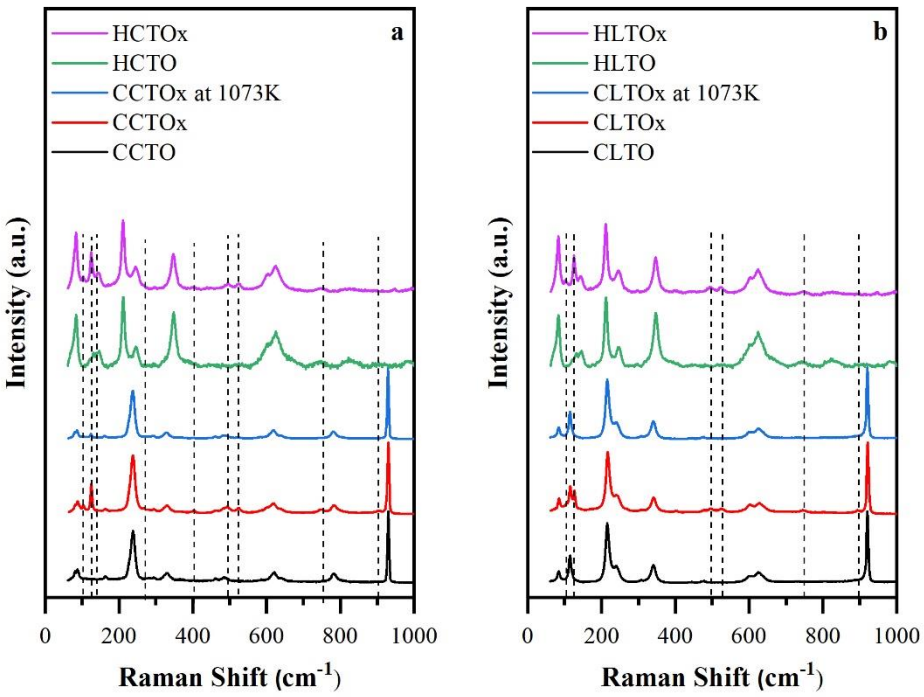

Figure 3.2 Raman spectrum **(a)** $CsCa_2Ta_3O_{10}$ and **(b)** $CsLaTa_2O_7$ and its derivates including nitride and protonated powder.

3.3.3 Ultraviolet-visible (UV-vis) Diffuse Reflectance Spectroscopy

UV–VIS absorption spectra and Kubelka-Munk (KM) function curves were employed to analyze the photocatalysis light absorption characteristics and bandgap. The optical band gaps were determined by plotting $[F(R)h\nu^{1/\eta}]$ against photon energy (hν), with F(R) representing the Kubelka-Munk function and η set to 2 for indirect transitions, as demonstrated in Figure 3.4 [112]. The intercept of the tangent lines of the KM plot indicated that the band gap of triplet and doublet tantalum-based perovskite oxide samples ($CsCa_2Ta_3O_{10}$ and $CsLaTa_2O_7$) exceeded 4eV, implying effective performance primarily in the ultraviolet region in contrast, the bandgap energies of $CsCa_2Ta_3O_{10-x}N_x$ (CCTOx) and $CsLaTa_2O_{7-x}N_x$ (CLTOx) extended into the visible light range to 2.0 eV and 1.9 eV, respectively, making them superior photocatalysts for solar applications in Figure 3.4.c and Figure 3.4.d.

The substitution of nitrogen with oxygen in the lattice modifies the material's electronic structure. This modification can cause electrons in the valence band to move to more positive energy levels, narrowing the band gap [120]. This change in the electronic

structure is accompanied by a change in the material's color, as the material absorbs and emits light at higher wavelengths (Figure 3.4. and Figure 3.4.b). The change in the electronic structure due to nitrogen intercalation likely causes the material to absorb light in the red part of the spectrum. After N loading to the oxide sample under ammonia gases, the white-colored catalyst converted to orange, as seen in Figure 3.3. The change in the electronic structure caused by nitrogen intercalation can also make the material a more efficient photocatalyst.

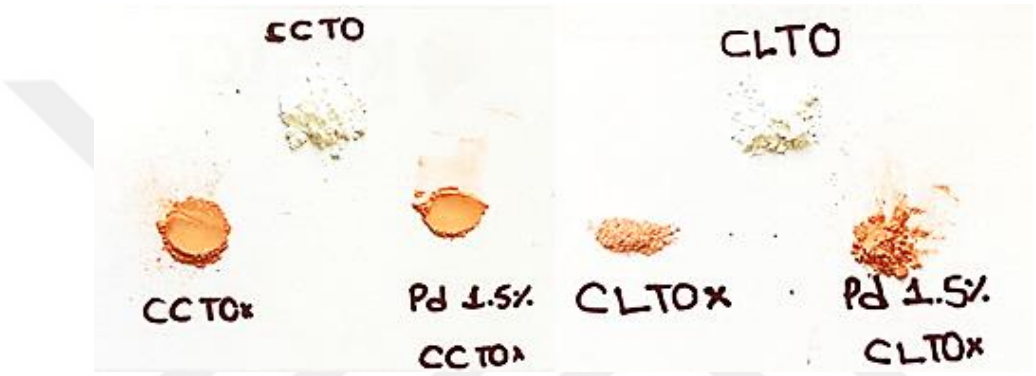

Figure 3.3 Change in color after N doping from white to light orange**.**

Additionally, the absorption spectrum revealed that tantalum-based oxynitride materials exhibit two absorption bands: around 500-600 nm and approximately 300-500 nm. The former is attributed to excitation from the N 2p orbital to the Ta 5d orbital, while the latter corresponds to excitation from the O 2p orbital to the Ta 5d orbital in Figure 3.4.a and Figure 3.4.b. When O^{2-} ions in the oxide phase are replaced by N^{3-} ions, the top of the valence band of the oxynitride crystal shifts upward due to the higher potential energy of N 2p atomic orbitals compared to O 2p atomic orbitals.

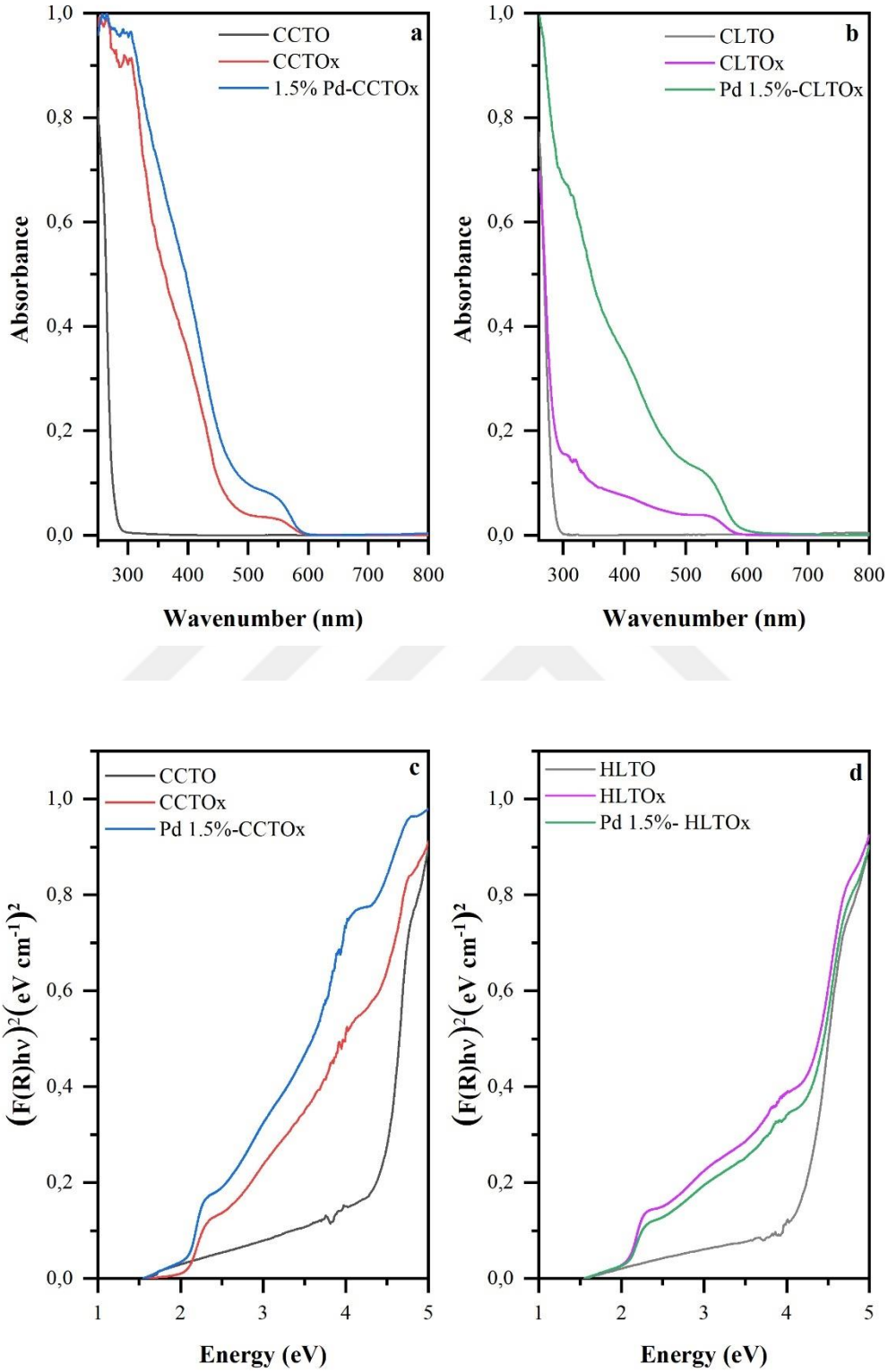

Figure 3.4 UV-vis absorption spectra of **(a)** $CsCa_2Ta_3O_{10}$, **(b)** $CsLaTa_2O_7$, and their oxynitride and Pd-doped oxynitride versions, as well as the transformation of diffuse reflectance data using the KM, for **(c)** $CsCa_2Ta_3O_{10}$ and **(d)** $CsLaTa_2O_7$ and their respective oxynitride.

Doping pure structure with Pd atoms also modifies its light absorption properties, potentially making it a slightly more effective photocatalyst by allowing it to utilize visible light, as seen in Figure 3.4. Consequently, this oxynitride material efficiently converts solar energy as a visible-driven photocatalyst.

3.3.4 X-ray Photoelectron Spectroscopy (XPS)

X-ray photoelectron spectroscopy (XPS) was employed to investigate the powder sample's elemental composition and chemical states. The acquired XPS data was deconvoluted using Thermo Avantage v5.973 software for improved peak analysis. The spectra were calibrated using the C 1s peak at 284.4 eV to ensure accurate binding energy information. All XPS spectra were also corrected for charging effects concerning the same C 1s peak. In the XPS binding energy spectra of CCTOx and CLTOx and their derivatives for Ta 4d, the Ta $4d_{3/2}$ and Ta $4d_{5/2}$ peaks centered at about 239.9 and 228.8 eV correspond to tantalum with the oxidation state of +5 in tantalum-based layered perovskite in Figure 3.5 [121].

Interestingly, XPS analysis revealed that these Ta 4d peak centers remained virtually unchanged after nitrogen doping. Therefore, the observed color change from white to light orange does not arise from reducing the tantalum oxidation state, such as the formation of Ta^{4+} species. The formation of this orange-colored powder is attributed to the doping N in the oxygen site, which causes an increase in the valence band maximum (VBM), as shown in Figure 3.8. This shift in the valence band, in turn, causes the material to absorb light at longer wavelengths (lower energy) compared to its original state. Consequently, the material starts absorbing a portion of the visible light as also observed in the UV-vis absorption spectrum.

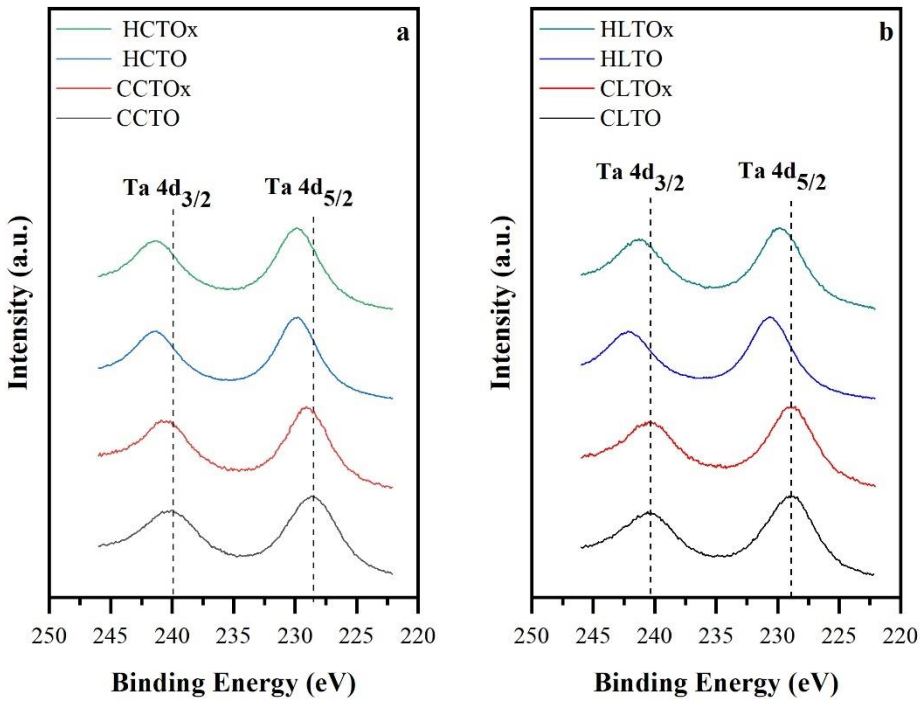

Figure 3.5 XPS binding energy spectra of Ta 4d **(a)** CCTOx and **(b)** CLTOx.

XPS analysis showed significant shifts in the binding energies of tantalum peaks after protonating material with hydrochloric acid (HCl). Compared to the untreated bulk material, the Ta 4d peaks (both 3/2 and 5/2) in the protonated material shifted to higher binding energies:

Ta $4d_{3/2}$: 239.9 eV (bulk) to 241.39 eV (protonated)

Ta $4d_{5/2}$: 228.8 eV (bulk) to 229.83 eV (protonated)

The Ta $4p_{3/2}$ peak also shifted from 403.3 eV in the untreated material to 404.1 eV in the protonated material, as shown in Figure 3.6. These peak shifts suggested structural changes [50] within the material after HCl treatment. Protons (H^+) replace cesium ions (Cs^+) in the interlayer after HCl treatment. The attractive force between oxygen and cesium ions is more substantial between oxygen and hydrogen [122].

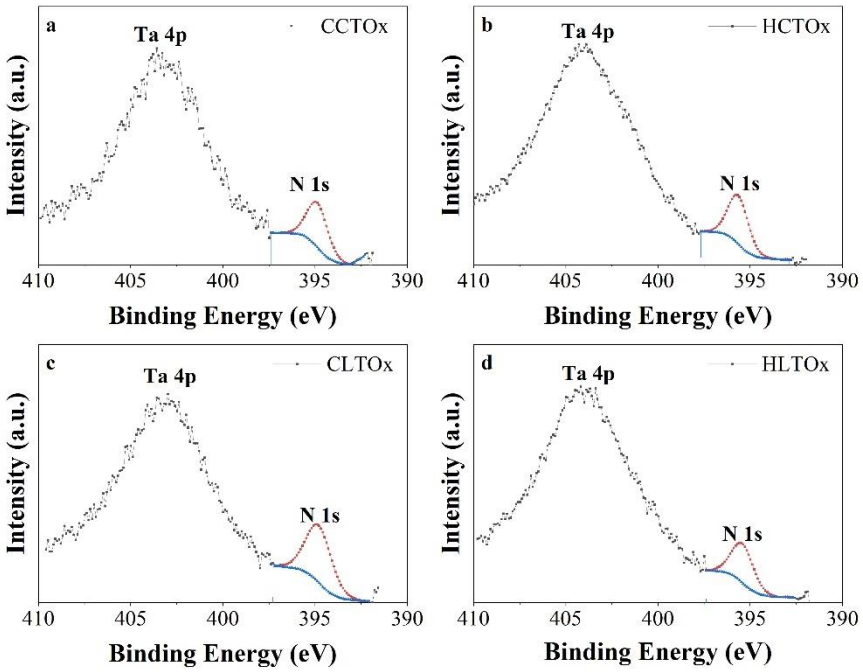

Figure 3.6 XPS binding energy spectra of Ta 4p and N 1s **(a)** CCTOx and **(b)** CLTOx.

The presence of the N 1s peak at 395.6 eV indicates explicitly the formation of a tantalum-nitrogen (Ta-N) bond within the lattice of the nanosheet, as illustrated in Figure 3.6. The peak of N 1s around 395.6 eV confirms the successful incorporation of nitrogen atoms into the material (nitrogen doping). The amount of nitrogen incorporated into the material was determined by analyzing the area under the N 1s peak in the XPS spectrum. According to the XPS results, 0.3 mol of nitrogen was replaced with oxygen for the CCTOx phase, and 0.2 mol of nitrogen was replaced with oxygen for the CLTOx phase. The closed formulas were determined as follows: $CsCa_2Ta_3O_{9.97}N_{0.3}$ and $CsLaTa_2O_{6.98}N_{0.2}$. Similar to the Ta 4d peaks discussed earlier, the O 1s spectra (refer to Figure 3.7) also shifted towards higher binding energies after protonating the material.

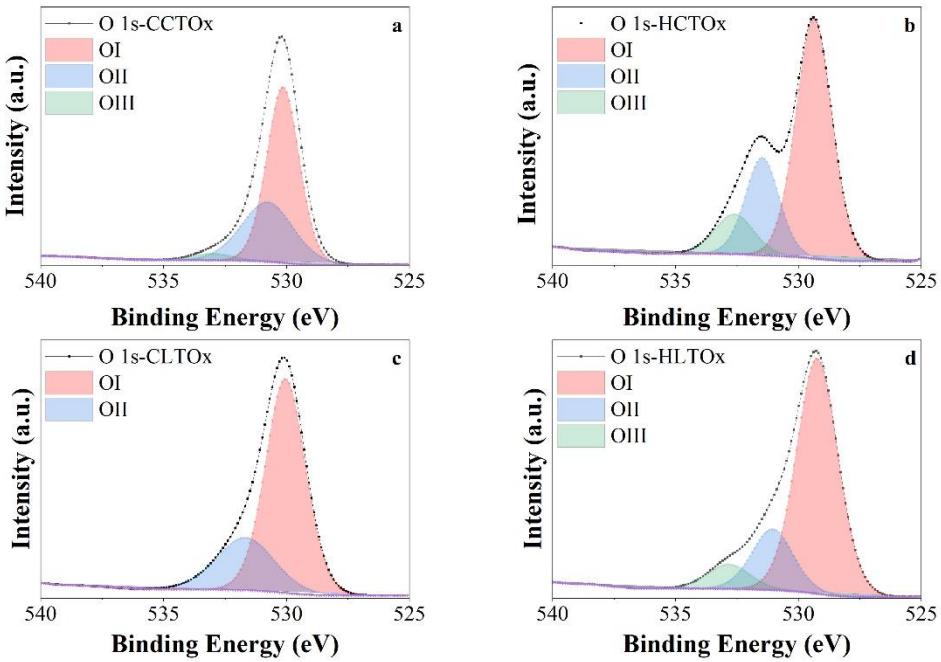

Figure 3.7 XPS binding energy spectra of O 1s **(a)** CCTOx and **(b)** CLTOx.

Deconvolution of the O 1s spectra revealed three distinct peaks [123]:

OI (529.5 eV): Lattice oxygen atoms bonded to the metal cations.

OII (531.1 eV): Oxygen defect sites with lower oxygen coordination (potentially oxygen vacancies) or oxygen of interlayer hydronium ions.

OIII (532.5 eV): Hydroxyl groups $(OH)^-$ likely from surface-adsorbed water molecules.

The protonation is believed to be responsible for the increased amount of hydroxyl groups (OIII) observed in the XPS spectra, as shown in Figure 3.7. This phenomenon can be attributed to two main factors: enhanced hydroxylation and water adsorption because the treatment enhances surface reactions and the peak intensity at the highest binding energy (OIII) [124].

Moreover, the valence band maximums (VBM) and conduction band minimums (CBM) for various materials (CCTO, CLTO, CCTOx, CLTOx, HCTO, HLTO, HCTOx,

HLTOx.) were calculated using XPS valence spectrum and energy band energies from UV-vis DRS as illustrated in Figure 3.8. The valence-band maximums from XPS valence spectrum of CCTO, CLTO, CCTOx, CLTOx, HCTO, HLTO, HCTOx, HLTOx were calculated to be −7.097, −6.930, −6.308, −6.180, −7.603, -7.937, -5.669 and -6.054 eV vs. vacuum or 2.657, 2.490, 1.868, 1.740, 3.163, 3.497 and 1.229 V vs. NHE, based on the relation $\boldsymbol{E\ (eV) = -4.44\text{-}E_{NHE}\ (V)}$ at pH=0, respectively. Considering each sample's band gap, the corresponding conduction band maximums were determined to be -1.756, -1.679, -0.190, -0.205, -1.213, -0.700, -0.839 and -0.386 V vs. NHE. Figure 3.8 illustrates the band energy diagram for the studied materials. As expected, nitrogen doping (N-doping) caused the valence band maximum (VBM) potential to shift upwards due to N 2P and O 2p orbital hybridization [125]. This upward shift in the VB translates to enhanced light absorption by the oxynitride samples.

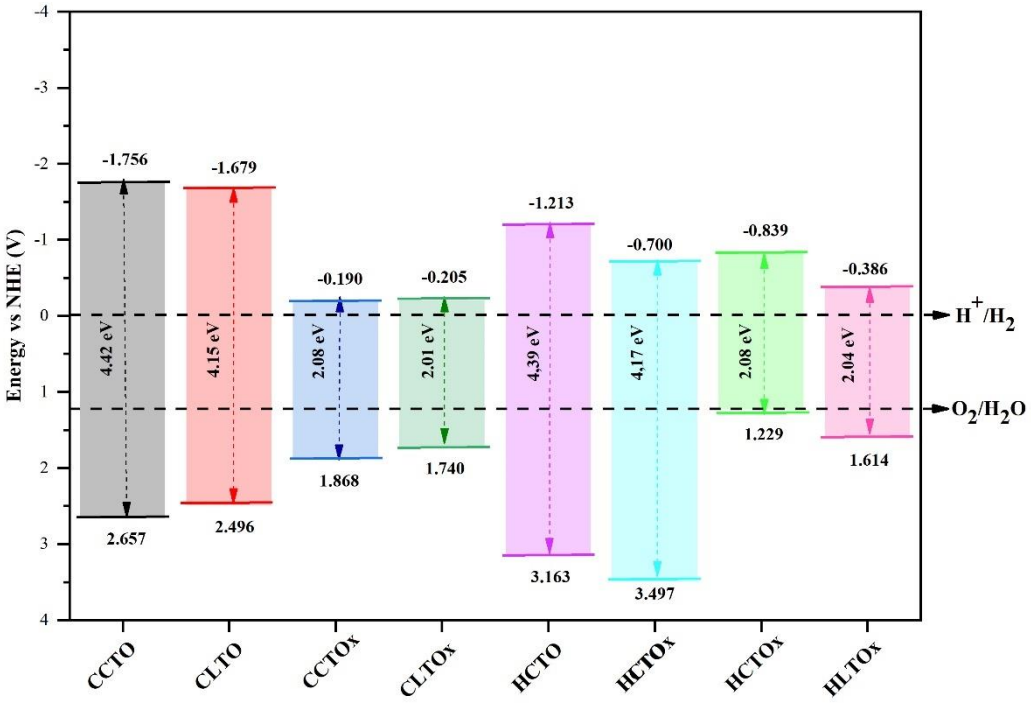

Figure 3.8 Schematic diagram of band energies for oxide, oxynitride and their protonation state from along with Kubelka-Munk function (obtained from DRS) and Valence-Band XPS Spectra.

Due to the improved light absorption, oxynitride materials become promising candidates for generating hydrogen (H_2) through photocatalysis, a light-activated process. The

suitability of a material for photocatalysis depends on the relative positions of its conduction band minimum (CBM) and valence band maximum (VBM) compared to the redox potential of the targeted reaction (hydrogen or oxygen generation in this case). Thermodynamically, more negative CBM indicates a stronger reduction reaction tendency, whereas a higher positive VBM potential indicates a stronger oxidation reaction driving force. Consequently, oxynitride samples exhibiting a more negative CBM demonstrated a higher hydrogen activity than oxide-based materials.

3.3.5 Inductively Coupled Plasma Mass Spectrometry (ICP-MS)

The Pd metal concentration loaded onto the structure's B site (Ta site) was investigated using Agilent 7700x inductively coupled plasma-mass spectrometry (ICP-MS). Table 3.1 illustrates the disparity between the theoretical and experimental weight percentage (wt.%) of Pd loading, determined by ICP-MS. This inconsistency may stem from factors such as non-uniform distribution, incomplete doping, limitations in measurement, or losses during processing. Despite discrepancies in the measured amount of Pd, ICP-MS confirms the incorporation of Pd into the material. However, accurately determining palladium via ICP-MS is challenging due to spectral interferences, highlighting the ongoing research interest in trace analysis of palladium within the ICP-MS community [126].

Table 3.1 Pd loading weight percent (wt.%) of tantalum-based layered perovskite by ICP-MS measurements.

Sample	Pd loading % (theoretical)	Pd loading % (ICP-MS)
1.5% Pd-CCTOx	0.523	0.120
1.5% Pd-CLTOx	0.428	0.260

3.3.6 Scanning electron microscopy (SEM)

Scanning electron microscopy images were analyzed using a Zeiss Ultra Plus field emission scanning microscope with 100.00 KX magnification at 5.00 kV. It was used to investigate the surface morphology of the samples, as shown in Figure 3.9. The pristine structures of CCTOx and CLTOx (Figure 3.9.and Figure 3.9.c) exhibited a lamellar

morphology. Despite the observed color change from white powder to orange after N doping (Figure 3.3), the layered morphology is largely preserved, with the crystal structure remaining intact, as confirmed by XRD results. Following protonation, the rectangular surface properties remained in HCTOx and HLTOx (Figure 3.9.b and Figure 3.9.e). However, a partial separation between the individual layers is observed, likely due to the incorporation of water molecules within the perovskite structure. After exfoliation, the individual layers become significantly more visible due to their atomic-scale thickness (Figure 3.9**.**c and Figure 3.9.e).

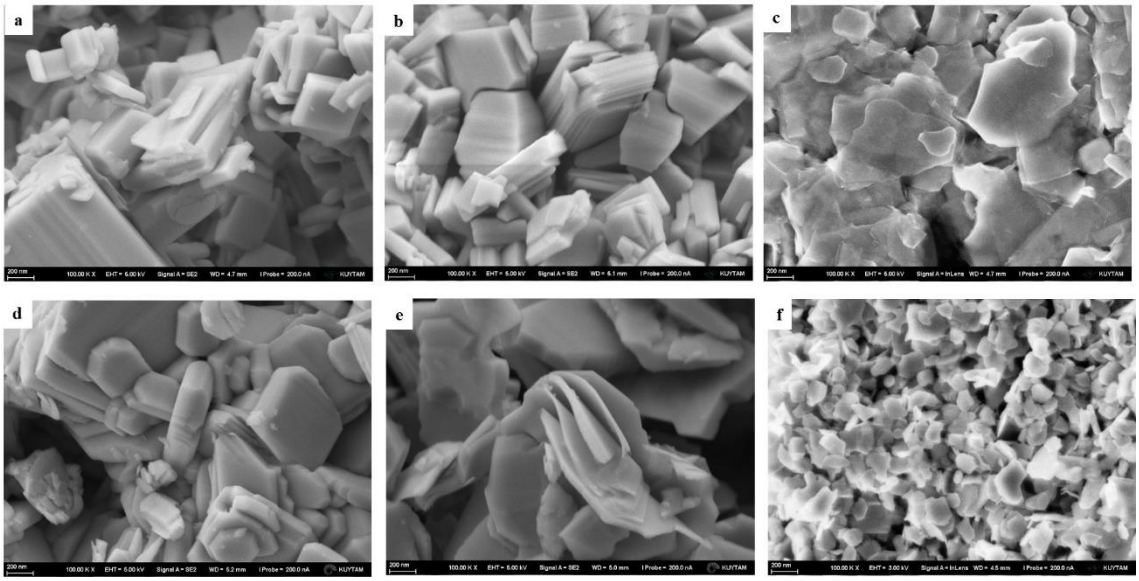

Figure 3.9 SEM images **(a)** CCTO, **(b)** HCTOx, **(c)** CTOx, **(d)** CLTO, **(e)** HLTOx, and **(f)** LTOx.

3.4 Results of Photoelectrochemical Experiments

3.4.1 Chronoamperometry (CA)

The transient photocurrent responses were conducted with a three-electrode system (WE: the synthesized photoelectrode, CE: Pt wire) at a potential of 1.0 V vs. SCE (sat'ed KCl) with a 300-watt Xe lamp. The three-electrode system is shown in Figure 3.10.

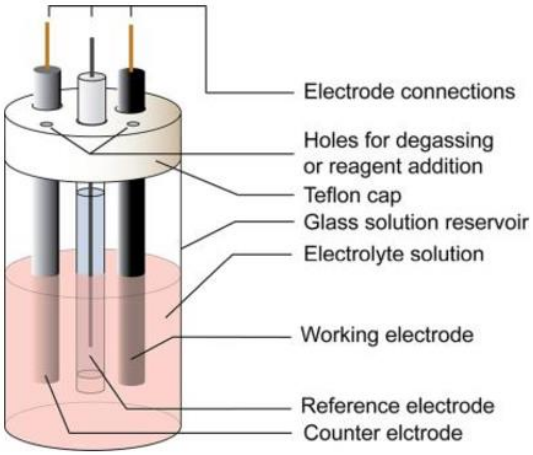

Figure 3.10 Illustration of a three-electrode system in a quartz cell.

The behavior of the photocurrent stability, charge transfer efficiency, and charge separation of the photoelectrode were investigated by analyzing the current behavior in chronoamperometry experiments. The observed systematic increase in the photocurrent density following the doping of nitrogen (N) and/or palladium (Pd) in oxynitride could be attributed to the enhanced concentration of charge carriers for all oxynitride samples. These dopants can alter the material's electronic structure, introducing additional charge carriers. Furthermore, N and/or Pd doping can also create shallow traps that temporarily immobilize photogenerated charge carriers. These shallow traps can be beneficial as they hinder the recombination of electron-hole pairs, extending the lifetime of the charges and facilitating their separation and migration upon photoexcitation. This improved charge carrier availability and extended lifetime ultimately led to increased photocurrent density [127]. The transient photocurrent response curve of pure and protonated powders and pure and exfoliated powders are given in Figure 3.11 and Figure 3.12, respectively.

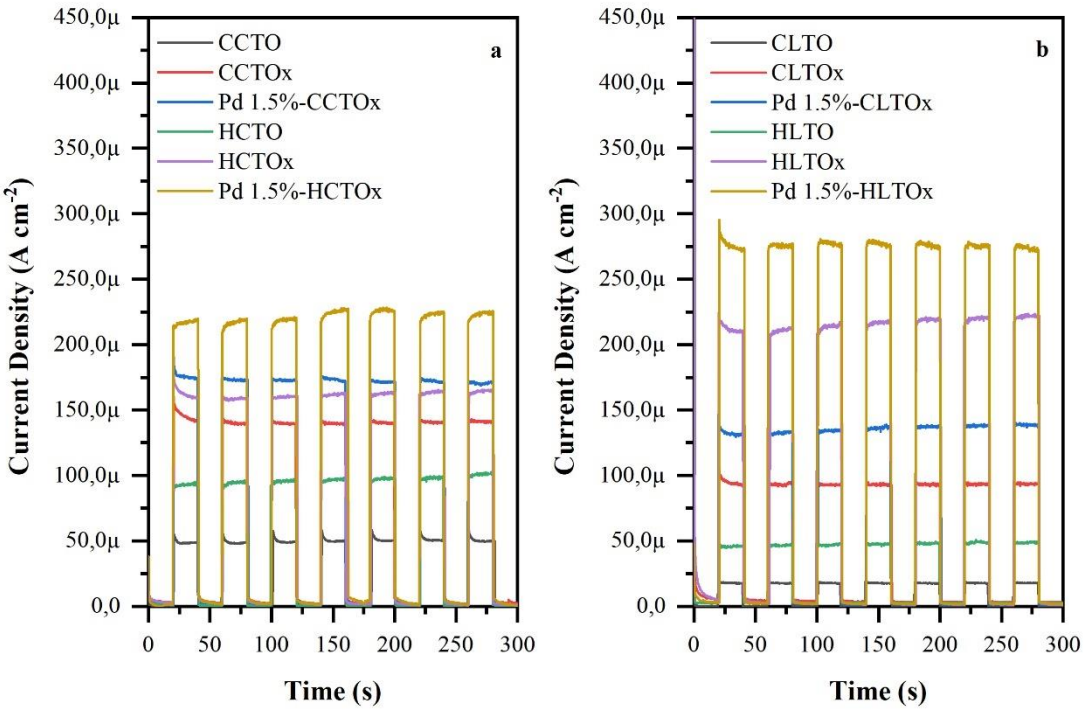

Figure 3.11 Chronoamperometry measurements of **(a)** original and protonated versions of both undoped, Pd and/or N-doped CCTO and **(b)** original and protonated versions of both undoped, Pd and/or N-doped CLTO at 1V vs SCE (sat'ed. KCl) under full spectrum.

Following the replacement of Cs^+ and H^+ ions in the oxynitride structure of two different phases, introducing hydronium ions (H_3O^+) and water molecules into the structure is believed to be responsible for the increased photocurrent. These H_3O^+ ions might act as proton donors, making separating electron-hole pairs generated by light absorption easier and making more charges available to contribute to the photocurrent. Compared to the photocurrent of DJ layered perovskites with n=2 and 3, there is more photocurrent after the proton exchange of the n=2 given than n=3 in Figure 3.11. The reason could be the position of the conduction band minimum significantly influencing the photocatalytic performance of tantalum-based layered perovskites, as reported by Wang et al. [112]. This information is in accordance with the results in the energy diagram obtained by combining the results of Valence-Band XPS Spectra and UV-vis DRS characterizations.

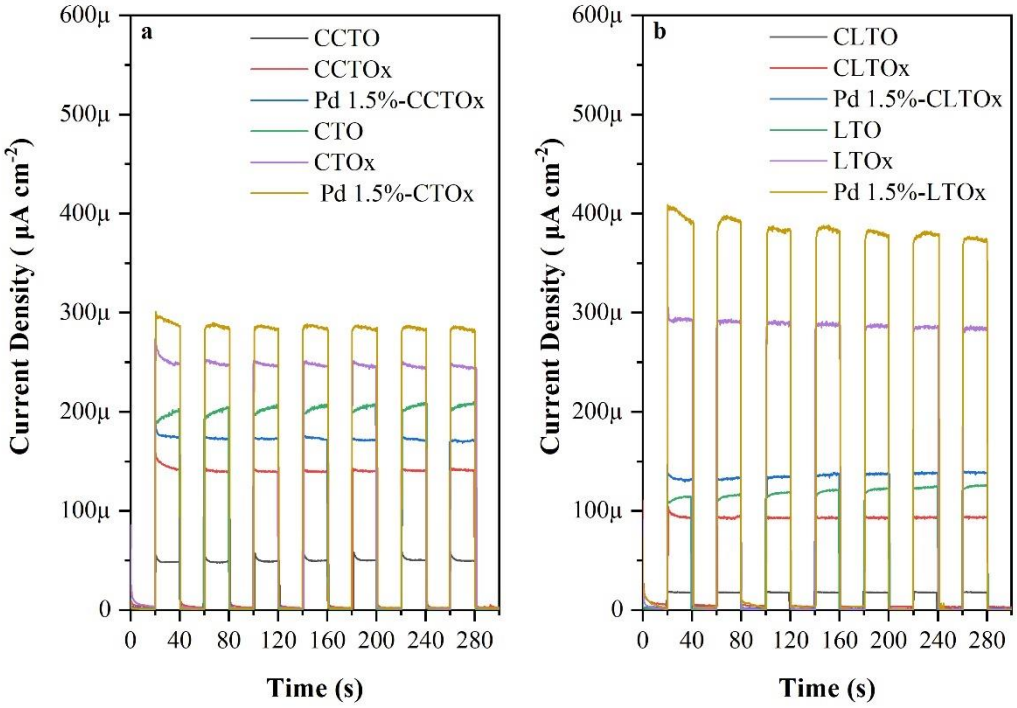

Figure 3.12 Chronoamperometry measurements of **(a)** original and exfoliated versions of both undoped, Pd and/or N-doped CCTO and **(b)** original and exfoliated versions of both undoped, Pd and/or N-doped CLTO at 1V vs SCE (sat'ed. KCl) under full spectrum.

The high photocurrent values of exfoliated samples observed in Figure 3.12 could be attributed to the fine atomic-level nanosheets, which minimize the probability of recombination by shortening the distance over which photo-excited species migrate. Additionally, these nanosheets provided more active sites due to their high surface area. The high surface area offered a significantly more prominent platform for light absorption and photocatalytic reactions, ultimately leading to a higher photocurrent.

3.4.2 Potentiostatic Electrochemical Impedance Spectroscopy (PEIS)

The Nyquist plots generated by EIS were utilized to conduct a more detailed investigation into the resistance encountered during interfacial charge transfer. The charge transfer resistance, Rct, is defined by the diameter of the semicircle. A smaller semicircle radius indicates an effective separation of photogenerated electron/hole pairs and a rapid interfacial charge transfer toward the electron donor or acceptor [128]. Figure 3.13 shows EIS spectra from 10^3 to 10^{-2} Hz with 0.01 mV amplitude at 1.0 V vs Hg/HgO in 0.5M

K_2SO_4. Compared to pure CLTOx and pure CCTOx, the semicircle size of exfoliated CLTOx and CCTOx has a minor arc diameter, as seen in Figure 3.13, suggesting a lower resistance against electron transfer. In addition, increasing the number of active sites on the surface due to the high surface area of exfoliated samples can offer more chances for carriers to participate in efficient transfer. Moreover, incorporating nitrogen and/or Pd dopants into semiconductor materials can boost conductivity, thereby diminishing resistance during charge transfer.

In the PEC experiment, it is thought that higher photocurrent in CA and a smaller semicircle radius in EIS measurements indicate increased hydrogen generation. This correlation could arise because a high photocurrent signifies more photogenerated electrons, and a smaller semicircle radius in EIS suggests faster charge transfer kinetics.

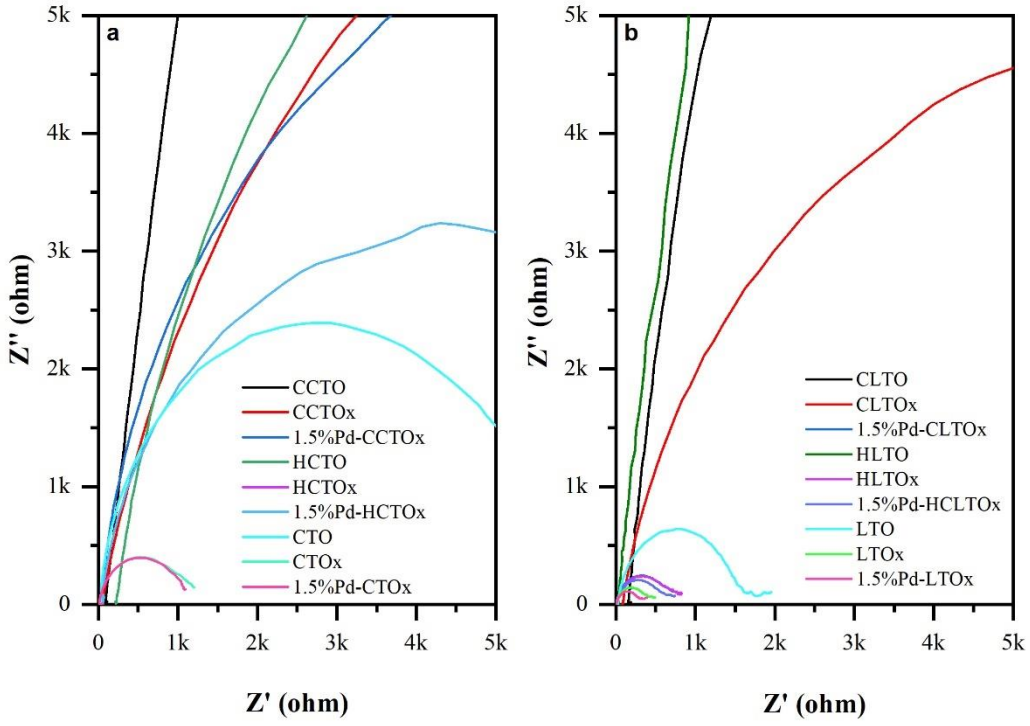

Figure 3.13 Nyquist electrochemical impedance spectra of undoped of original phase, protonated phase, and exfoliated phase and their N and Pd doped oxynitride derivatives of **(a)** $CsCa_2Ta_3O_{10}$ and **(b)** $CsLaTa_2O_7$.

3.5 Photocatalytic Hydrogen Production

Photocatalytic activities of bulk, protonated, and exfoliated $CsCa_2Ta_3O_{10}$ (CCTO) and $CsLaTa_2O_7$ (CLTO) were subsequently assessed by observing hydrogen production from

water in the presence of sacrificial agents (%10 methanol) under full spectrum as given in Figure 3.14 and filtered spectrum with AM 1.5G filter as given in Figure 3.15. Based on H_2 generation in the full spectrum illumination graph, the experiment observed a dramatic enhancement in hydrogen generation using nanosheets due to its higher surface area and shorter migration distance. Compared to the bulk material, 1.5% Pd-CTOx and 1.5% Pd-LTOx nanosheets produced over 50 and 30 times more hydrogen under full-spectrum light due to their higher surface area. BET analysis revealed that the surface area of their original structures was enhanced by a factor of ten. It is assumed that incorporating palladium into the oxynitride structure resulted in its dispersion as single atoms throughout the nanosheets. This improved distribution of Pd atoms, confirmed by ICP-MS, is believed to enhance the material's ability to generate hydrogen through photocatalysis. In addition, compared to the layered perovskite with n=3, compounds with n=2 demonstrated high activity, with the amount of evolved H_2 increasing steadily with reaction time. Therefore, the activity order observed was $[LaTa_2O_7]^- \approx 1.25 \times [Ca_2Ta_3O_{10}]^-$ (1000 ± 5 $\mu mol \cdot g^{-1}$ vs. 800 ± 5 $\mu mol \cdot g^{-1}$). The differences observed in HER activity can be attributed to several factors, including the material's band gap energy, photoelectrochemical properties, surface area, and defects in its structure.

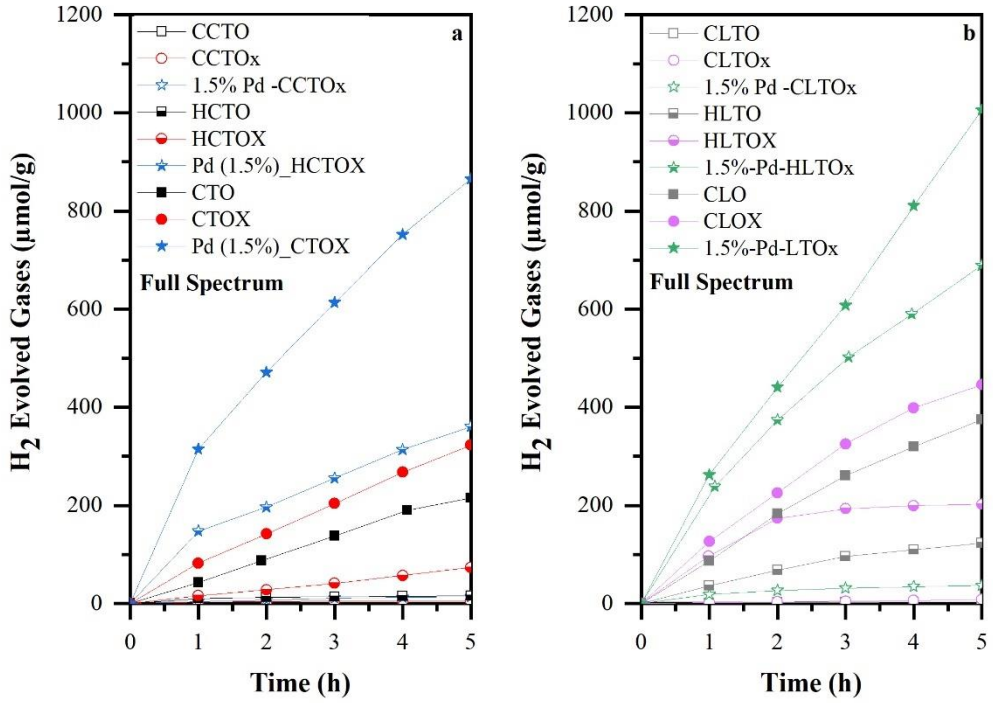

Figure 3.14 The photocatalytic HER of **(a)** $CsCa_2Ta_3O_{10}$ and **(b)** $CsLaTa_2O_7$ and their oxynitride and Pd doped oxynitride version for parent, protonated, and layered nanosheets form.

The photostability of the Pd-doped oxynitride nanosheet and protonated photocatalyst was evaluated via a 15-hour cyclic experiment monitoring hydrogen evolution using an A.M. 1.5G filter. The hydrogen accumulated in the cell was evacuated with Argon gas every 5 hours, and the experiment was started again with the same powder. Figure 3.15 displayed that the nanosheet and protonated doublet (Figure 3.15**.**b) and triplet tantalum-based (Figure 3.15.a) perovskite composition demonstrates remarkable stability for visible-driven photocatalytic applications.

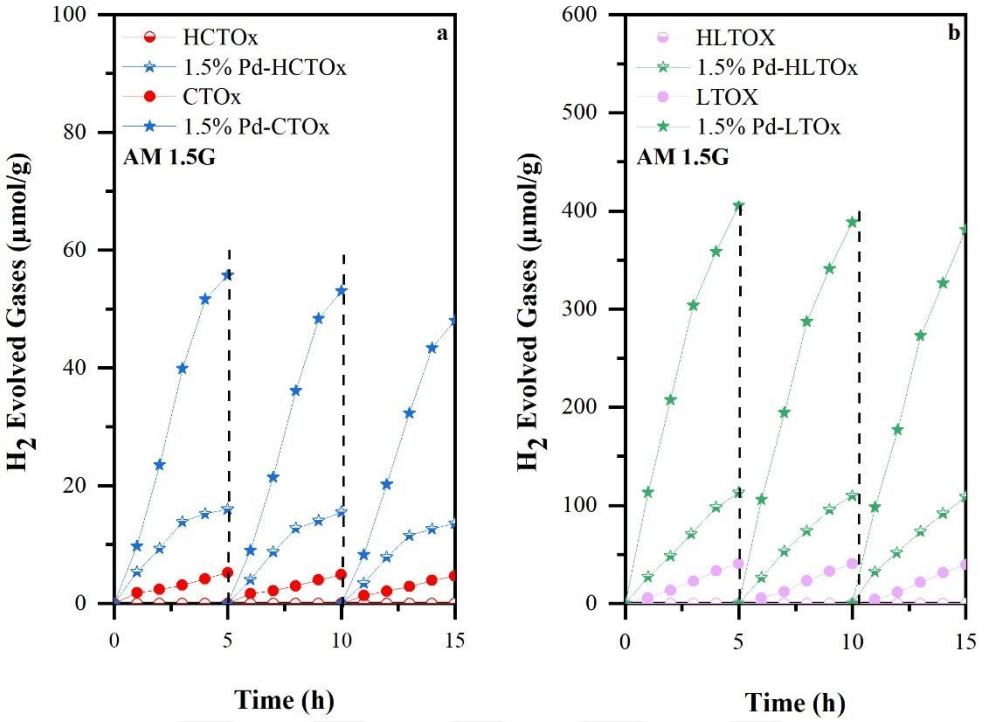

Figure 3.15 Stability test of photocatalytic HER of undoped and doped **(a)** protonated and nanosheet of three-layered tantalum oxynitride and **(b)** protonated and nanosheet of two layered oxynitride.

3.6 Conclusions

This chapter synthesized pristine doublet and triplet layered perovskite oxynitride and their Pd-doped counterparts via Pechini method. The effect of the doping strategy on photocatalytic hydrogen generation at the solar spectrum and photoelectrochemical behavior was investigated.

The XRD pattern of synthesized catalysts confirmed the tetragonal symmetry structure, with no impurity peaks detected. Besides XRD, Raman spectroscopy was used to identify structural variations in binary and ternary oxides and oxynitride systems. Raman spectroscopy results showed that new peaks appeared after nitridation, likely due to nitrogen atoms incorporated into the material's structure. These peaks disappeared when heated at 1073K, indicating they were related to nitrogen. The XPS results also approved the presence of the N 1s peak at 395.6 eV, indicating the formation of a tantalum-nitrogen (Ta-N) bond within the nanosheet lattice. However, XPS did not detect low

concentrations loading of palladium; thus, ICP-MS was used to confirm the presence of palladium in the material successfully. ICP-Ms results showed a smaller Pd doped than theoretical, possibly due to factors like non-uniform distribution or measurement limitations. However, accurately determining palladium remains challenging.

Further, no significant changes were observed in the overall morphology of the materials. When nitrogen with or without palladium (Pd) were added, SEM analysis revealed that all synthesized catalyst powders maintained a layer-like morphology. UV-vis diffuse reflectance spectroscopy examined the synthesized powders' absorption properties and bandgap energies. UV-vis DRS results showed that it had been observed that it reduces the bandgap to less than 3 eV, indicating effective performance in visible-driven photocatalysts.

The synthesized powders' photoelectrochemical properties were investigated using chronoamperometry (CA) and electrochemical impedance spectroscopy (EIS). This study utilized CA analysis to investigate the materials' photoelectrode stability, charge transfer efficiency, and charge separation. Incorporating nitrogen or palladium into the oxynitride structure enhanced photocurrent densities. Additionally, protonation improved photocurrent, likely due to a hydrated interlayer. Exfoliated samples exhibited exceptionally high photocurrent values due to atomic level thickness and higher surface area. Enhanced photocurrent behavior can be attributed to a decrease in the diffusion layer and an increased surface area. Analysis of resistance during interfacial charge transfer, conducted using EIS measurements, revealed better charge separation in exfoliated powders compared to pristine powders.

The study further evaluated the synthesized materials' photocatalytic hydrogen evolution activity. Bulk, protonated, and exfoliated forms of double and triple-layered oxynitrides were analyzed. The higher surface area of the exfoliated nanosheets led to a significant boost in hydrogen generation due to two main advantages of the nanosheets: a much larger number of active sites available for the reaction and a reduced chance of charge carriers recombining before they can be used. Notably, the nanosheets produced over 50 and 30 times more hydrogen production under full-spectrum light irradiation than the bulk material for double and triple-layered structures, respectively. Furthermore, the improved distribution of palladium atoms within the nanosheets is believed to contribute to enhanced photocatalytic hydrogen generation. Finally, the photostability of the most

promising materials – the nanosheets and the protonated photocatalyst – was assessed through a 15-hour cyclic experiment, demonstrating their reusability.

Chapter 4: Improved Hydrogen Generation via Singular-Atom Palladium Loaded Nanosheets Derived from Three Layered Dion Jacobson Layered Perovskites Oxide

4.1 Introduction

Solar hydrogen fuel, generated from water splitting via photocatalysis or photoelectrochemical process, offers significant potential as green energy and sustainable fuels instead of fossil fuels. Many photocatalysis have been synthesized on water splitting since Fujima Honda in 1972 [64]. Layered perovskite oxide (LPOs) has excellent potential for solar hydrogen energy in photocatalysis because of its flexible interlayer and tunable band structure. The flexibility framework allows the ion exchange of larger cations like Cs, Rb, and K between layers because the cations bond electrostatically with each perovskite slab. Due to their weak electrostatic van der Waals (vdW) forces, layered perovskite oxides (LPOs) exhibit favorable properties for "host-guest" chemistry. This allows LPOs to be exfoliated into two-dimensional nanosheets (NSs) and subsequently restacked to form three-dimensional, bonded perovskite structures. This 2D ultra-thin structure shortens the migration distance, where photo-induced charge particles participate in the surface reaction, thus increasing photocatalytic performance. The few atomic-level nanosheets make charge separation and transfer easier by reducing bulk and surface recombination [64], [129].

However, the water-splitting efficiency of photocatalysis still needs to improve. Some strategies enhance photo efficiency, such as controlling size and shape, surface modification, metal doping, co-catalyst, and exfoliation techniques. Metal doping is a more common trick than other strategies [64]. In this traditional metallization doping, while the metal nanoparticles improve photoactivity, not all metal atoms are equally active. Some may remain within the cluster or interact poorly with the semiconductor. Suppose all atoms are 100% used in the metal contribution. In that case, each atom can serve as a catalytic reaction center and increase photoactivity. It is called a single-atom catalyst site (SACs) [130]. While SACs are a promising approach for boosting photoactivity, there are still challenges like stable dispersion of single atoms and ensuring they efficiently interact with the surface [131]. The ultrathin-layered perovskite nanosheet

structure represents a significant advancement in heterogeneous catalysis. It enables the highly uniform dispersion of SACs, enhancing their catalytic activity and selectivity [73].

In light of the information mentioned above, the synthesis of single-site Pd doped in bulk-formed $CsCa_2Ta_3O_{10}$ and its protonated and nanosheet powders was reported, focusing on the effect of photocatalytic hydrogen production.

4.2 Experimental Procedure

The experimental part is explained in detail in chapter 2.

4.3 Result and Discussion

4.3.1 X-Ray diffraction Spectroscopy (XRD)

X-Ray diffraction Spectroscopy patterns obtained from the original structure (CCTO) and its modified structure (Pd-doped CCTO) are indicated in Figure 4.1.a. The synthesized $CsCa_2Ta_3O_{10}$ (Inorganic Crystalline Structure Database called ICSD #89011) [132] tantalum-based oxide has tetragonal symmetry with the P4/mmm space group in agreement with the literature [49]. The miller indices of XRD patterns were already given in Chapter 3.3.1. All powders have no impurity phases, not even for pallidum doping. The protonated mother phase and their Pd doped version have different space groups (I4/mmm) due to the exchange of Cs^+ with H^+. However, doped and undoped protonated samples indicated the same crystal structure, as shown in Figure 4.1.b.

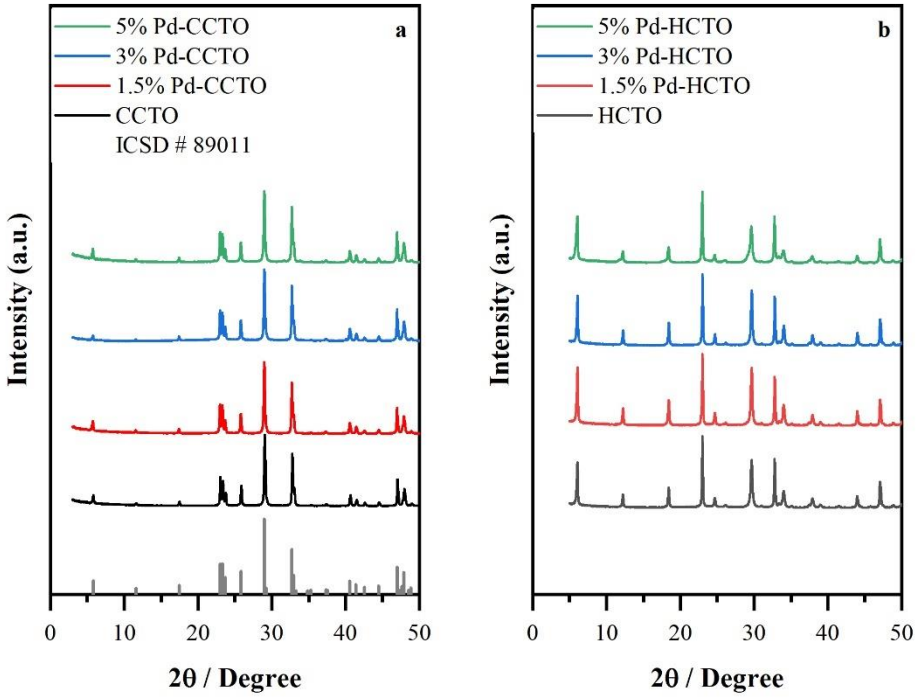

Figure 4.1 XRD pattern of **(a)** $CsCa_2Ta_3O_{10}$ (CCTO) and their Pd doped counterparts **(b)** $HCa_2Ta_3O_{10}$ (HCTO) and their Pd doped counterparts.

4.3.2 Raman Spectroscopy

The Raman spectra depicted in Figure 4.2.a show pure $CsCa_2Ta_3O_{10}$ and its Pd-doped variants at 1.5%, 3%, and 5% levels, while Figure 4.2.b displays their protonated counterpart ($HCa_2Ta_3O_{10}$). The initial spectra (Figure 4.2.a) show peaks around 930 cm^{-1} and 330 cm^{-1}, characteristic of Ta-O terminal bond vibrations in tantalum oxides. Importantly, these peaks are sensitive to the presence of interlayer species, potentially causing shifts or changes in intensity.

The proton exchange process led to some changes in the Raman spectra. For example, the peak at 930 cm^{-1} weakens and shifts to a higher wavenumber, while the peak at 330 cm^{-1} splits into two distinct peaks at 300 cm^{-1} and 335 cm^{-1} on the Raman Spectrum in Figure 4.2.b [119]. These changes are attributed to replacing Cs^+ ions with H^+ (protons) and introducing water molecules during the process, as confirmed by XPS analysis.

Besides that, the literature typically identifies only two Raman-active modes (B_1g at 647 cm^{-1} and Eg at 424 cm^{-1}) for the tetragonal phase of PdO crystals [133]. The presence of additional peaks in the spectra of protonated samples around 650 cm^{-1}, particularly at their surface, confirmed the existence of Pd intercalation of structure. However, the unmodified protonated phase naturally did not show the peak due to the B_1g vibration modes for the Pd-O bond.

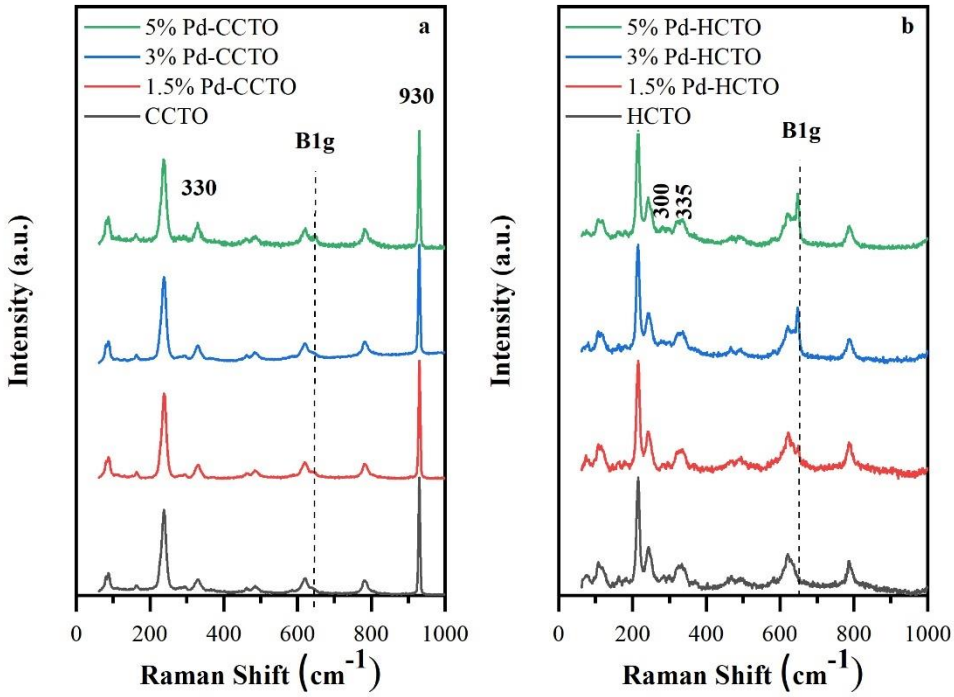

Figure 4.2 Raman Spectrum of **(a)** $CsCa_2Ta_3O_{10}$ and their Pd doped version **(b)** $HCa_2Ta_3O_{10}$ and their Pd doped version.

4.3.3 Ultraviolet-visible (UV-vis) Diffuse Reflectance Spectroscopy

The absorbance spectra of the samples were obtained using the Kubelka-Munk (KM) transformation of their diffuse reflectance spectra, as shown in Figure 4.3.a. The band gap energy (Eg) is estimated by extrapolating the linear portion of the transformed KM function (F(R)) versus the photon energy (hv) plot to the x-axis (energy). This extrapolation gives the band gap energy at the intersection of the extrapolation line with the x-axis on the KM curve.

It is known that the Ta-O-Ta bond angle is 180°. This bond angle efficiently transfers excited energy from oxygen to tantalum orbitals [134]. The introduction of palladium (Pd) atoms into the CCTO structure is thought to disrupt the original bond angle arrangement due to the formation of Pd-O-Pd bonds. These changes in bond angle geometry caused by Pd incorporation were expected to influence the material's light absorption and energy transfer characteristics. Consistent with this expectation, the results of the absorption spectrum show that Pd doping causes a slight shift in the absorption spectrum, leading to slightly improved light absorption properties.

Furthermore, the calculated band gap energies for the undoped and Pd-doped samples (1.5%, 3%, and 5% Pd ratios) of the pure crystal were 4.4 eV, 4.3 eV, 4.37 eV, and 4.42 eV, respectively, as shown in Figure 4.3.b. This slight band gap narrowing can be attributed to the emergence of new energy bands within the forbidden energy region. These newly formed bands are believed to originate from the 4d electrons of the palladium (Pd) atoms incorporated into the material. Furthermore, doping with Pd^{+2} ions, which have a lower positive charge than the original Ta^{5+} ions, results in the capture of electrons by the Pd^{2+} ions. These electron traps serve to reduce the probability of recombination with holes, potentially enhancing photocatalytic activity by controlling the number of free electrons. These results are in accordance with those obtained from chronoamperometry [135].

Protonation (HCTO) induced a red shift in the absorption edge compared to the non-protonated counterpart (CCTO). This indicated that HCTO absorbs light at slightly longer wavelengths. Similar behavior was also observed for Pd-doped materials. The absorption band edges for CCTO, 1.5% Pd-CCTO, HCTO, and 1.5% Pd-HCTO were approximately 272 nm, 274 nm, 276 nm, and 287 nm, respectively (Figure 4.3.a). Previous studies in [136] and [137] showed that the material's interlayer cations influence the overall band structure.. This variation (the exchange of Cs^+ located between the layered perovskite layers with H_3O^+ ions) is attributed to the differing interactions between these interlayer cations and the oxygen atoms directly opposite them within the interlayer space. Based on this knowledge, the observed differences in the light absorption profiles of the materials are thought to arise from these interactions between the interlayer atoms and the perovskite slab.

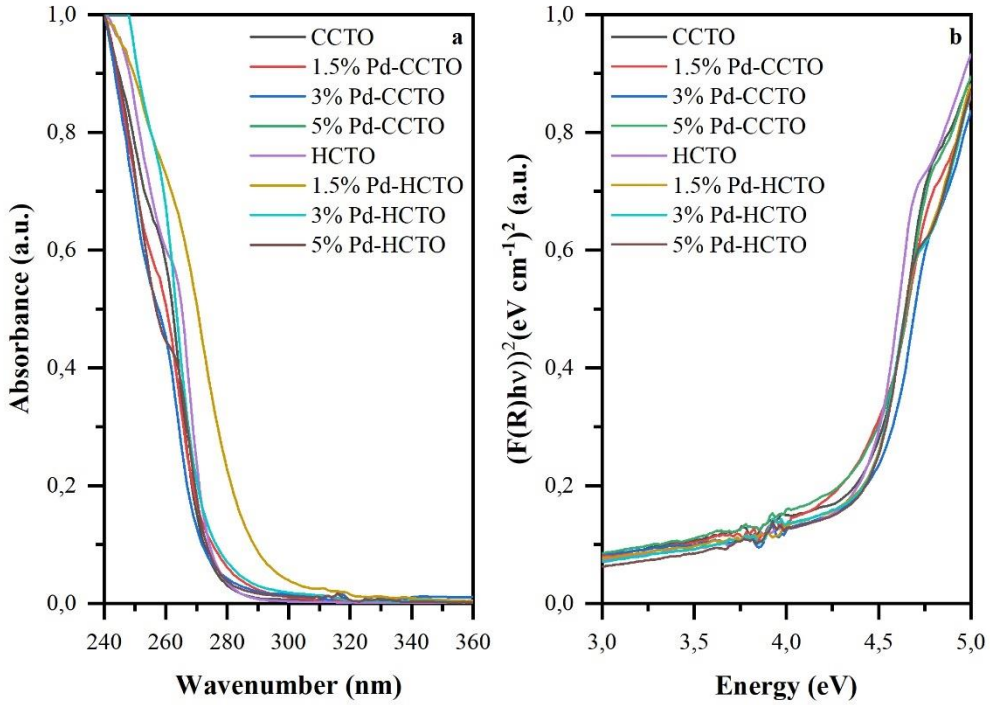

Figure 4.3 (a) UV-vis absorption spectra of pure and protonated of $CsCa_2Ta_3O_{10}$ (and their different loading of Pd-doped versions, and **(b)** Kubelka-Munk curve of pure and protonated of $HCa_2Ta_3O_{10}$ and their different loading of Pd-doped versions for calculation of band gap.

4.3.4 X-ray Photoelectron Spectroscopy (XPS)

XPS is a powerful tool for surface analysis because it can provide information about the elemental composition and oxidation state. The XPS analysis revealed that the tantalum atoms in these materials exist in a +5-oxidation state, as evidenced by the specific positions of the Ta 4d electron peaks, which are centered at around 239.9 eV and 228.8 eV for the Ta $4d_{3/2}$ and Ta $4d_{5/2}$ electrons, respectively, as illustrated in Figure 4.4.

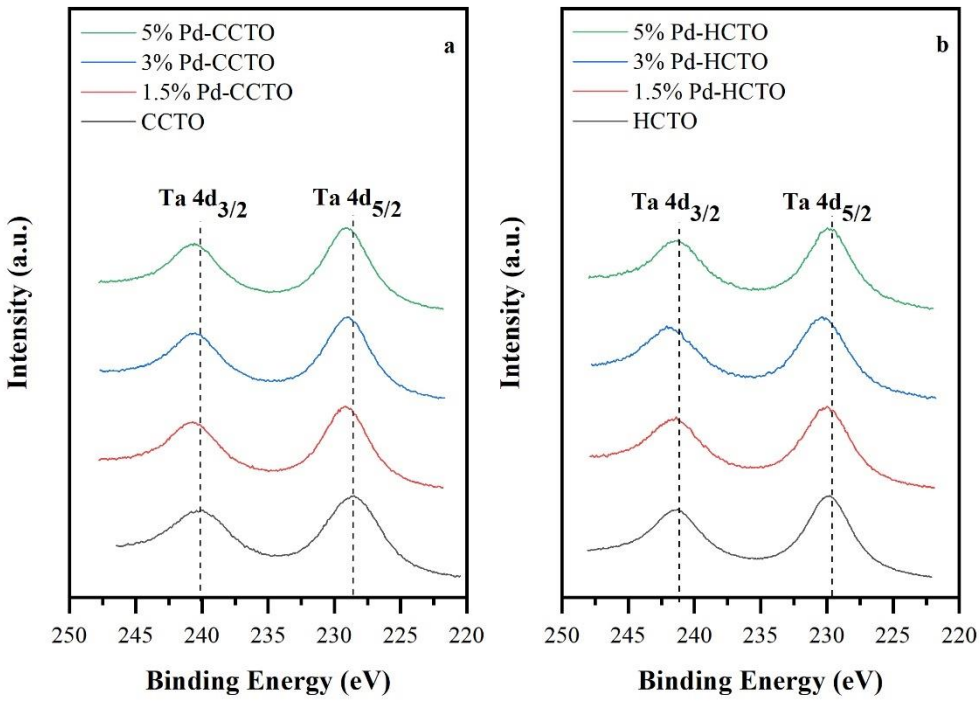

Figure 4.4 XPS binding energy spectra of Ta 4d **(a)** pure and 1.5%, 3% and 5% Pd doped of CCTO and **(b)** pure and 1.5%, 3% and 5% Pd doped of HCTO.

Based on Figure 4.4, when Pd (+2) replaces Ta (+5) in the lattice, the partially positive charge on the Pd atom and the introduction of new electronic states due to Pd doping can influence the electronic environment around neighboring Ta atoms, potentially leading to an increase in the effective nuclear charge (Z_{eff}) experienced by Ta 4d electrons. This, in turn, could result in a slight increase in their binding energy.

Moreover, The XPS analysis in Figure 4.4 revealed significant shifts in the binding energies of tantalum peaks after protonating material with 3M of hydrochloric acid. The Ta 4d peaks (both 3/2 and 5/2) in the protonated material shifted to higher binding energies. Due to stronger electrostatic interactions, these changes suggest structural changes within the material, with protons replacing cesium ions at interlayer regions. Furthermore, this result was also proved by XRD analysis, as shown in Figure 4.1, which showed that the XRD pattern of the protonated sample is different from that of the unmodified sample. The reason for this is stated to be due to the change of the space group [50]. Following the protonation and exfoliation process, a notable positive shift in binding energies related to unmodified samples was observed in the Ta $4d_{3/2}$ and Ta $4d_{5/2}$ peaks, with 239.9 eV and 228.4 eV, respectively as shown Figure 4.5 For protonated samples,

the binding energies of the Ta $4d_{3/2}$ and Ta $4d_{5/2}$ peaks were measured at 240.5 eV and 229.8 eV, while for exfoliated samples, they were recorded at 241.7 eV and 230.5 eV, respectively. When H^+ ions replace Cs^+ ions in interlayers, the Ta-O bond length contracts slightly, resulting in a stronger interaction between Ta and O and higher binding energy for Ta 4d electrons. The difference in charge and size between these ions also affects electron distribution, affecting the electrostatic interaction between Ta and O.

After exfoliation, nanosheet surface chemistry changes because the layers are separated into individual nanosheets. The surface O of nanosheets interacts with TPB^+ and H^+ on the surface, creating a weaker Ta-O bond. This strengthens the hold of electrons on Ta 4d electrons, increasing their binding energy observed in XPS.

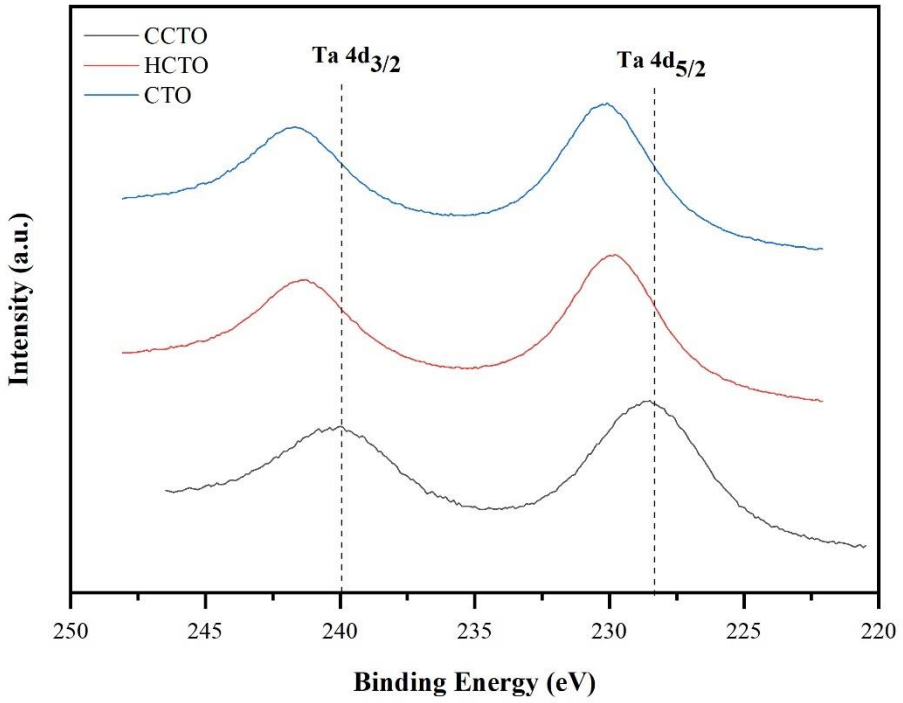

Figure 4.5 XPS binding energy spectra of Ta 4d pure, protonated, and exfoliated of CCTO.

As shown in Figure 4.6, XPS spectra successfully detected the presence of palladium (Pd) only at its highest dopant level of 5%. However, ICP-MS was used to detect the small concentrations of Pd (1.5% and 3%). The deconvoluted Pd 3d XPS spectrum reveals two peaks: one at around 335.1 eV corresponding to Pd $3d_{5/2}$ and another at around 340.3 eV

corresponding to Pd $3d_{3/2}$ based on 284.4 eV of C 1s [138]. These peak positions are consistent with a Pd $^{2+}$ oxidation state within the structure.

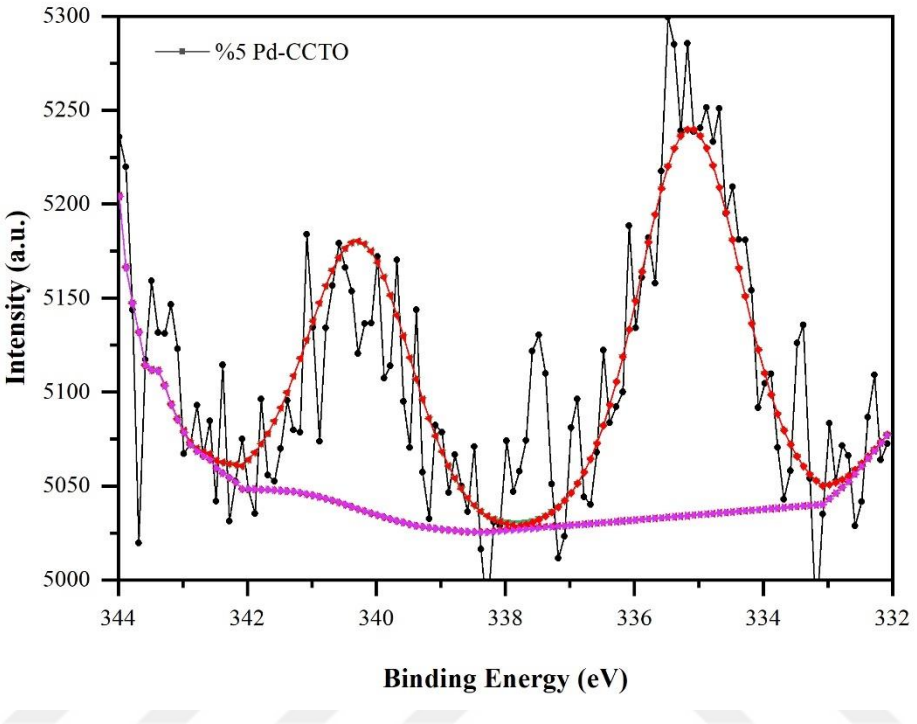

Figure 4.6 XPS binding energy spectra of Pd 3d pure for %5 Pd doped CCTO.

XPS valence band spectra and UV-vis diffuse reflectance spectroscopy (DRS) were combined to determine the valence band maximum (VBM) and conduction band minimum (CBM) of the materials. Figure 4.7 illustrates the electronic band structures for both undoped and doped states of the pure and protonated materials. Based on the electronic band structures of the samples, the CBM positions of the doped and undoped pristine and protonated samples were identified as suitable positions for hydrogen evolution. Compared to undoped versions, it was seen that Pd doping generally created a more favorable electronic structure by shifting the CBM to a more negative position. This negative shift drives the chemical reaction that converts protons (H^+) into hydrogen gas (H_2).

Interestingly, the 1.5% Pd-CCTO sample did not exhibit the typical negative CBM shift from Pd doping. This case can be explained that its smaller band gap and its higher VBM can cause a less negative CB position. However, a smaller band gap allows for easier

electron excitation within the material, potentially mitigating the disadvantage of a slightly less negative CBM. Another factor influencing the electronic structure is protonation. As illustrated in Figure 4.7, this process increases VBM but interestingly leads to a significant decrease in the CBM position along with a narrower band gap. Among the studied materials, the one containing 1.5% Pd after undergoing acid exchange exhibited the most negative CBM. This suggests that this material would be the most efficient for hydrogen generation due to the enhanced driving force provided by the negative CB for the desired chemical reaction. This finding is consistent with the photocatalytic HER results.

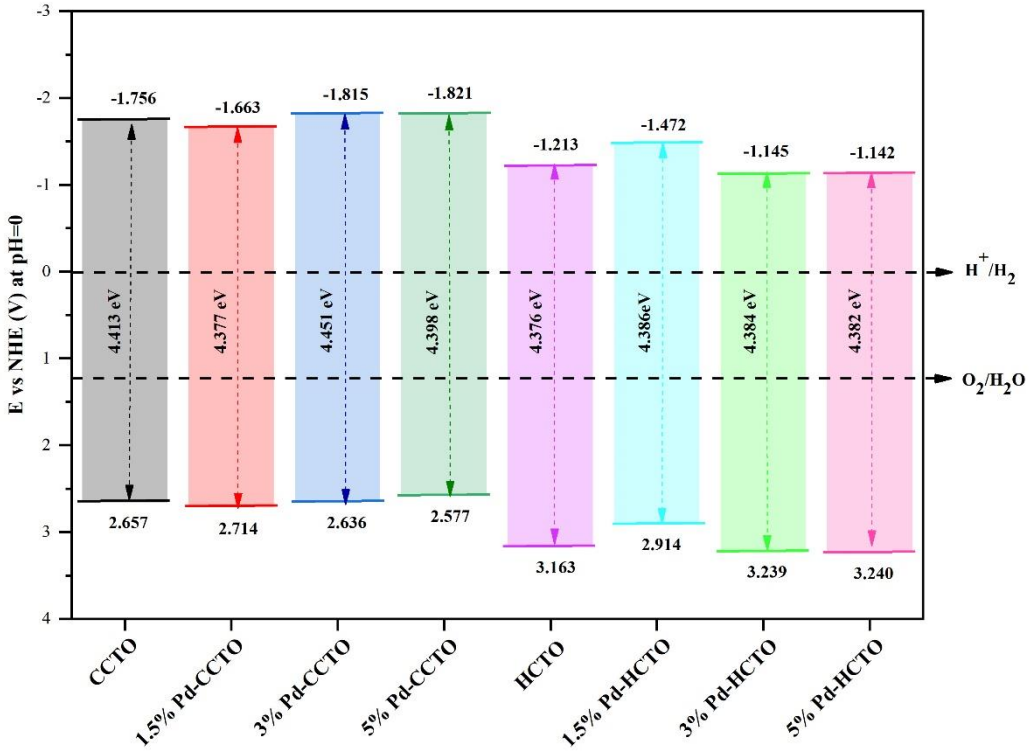

Figure 4.7 Schematic diagram of band energies for undoped and doped of CCTO and HCTO.

4.3.5 Scanning Electron Microscopy (SEM)

Scanning electron microscopy images were analyzed using a Zeiss Ultra Plus field emission scanning microscope with 100.00 KX and 500.00 KX (for exfoliated powder) magnification and 5.00 kV. It was used to investigate the surface morphology of the

samples. As shown in Figure 4.8, SEM analysis confirms the layered nature of all material versions. However, the layered structure appears significantly more pronounced in the exfoliated version compared to the non-exfoliated samples. This enhanced visibility is likely due to the atomic-level thinness of the exfoliated material, allowing for a clearer observation of the individual layers.

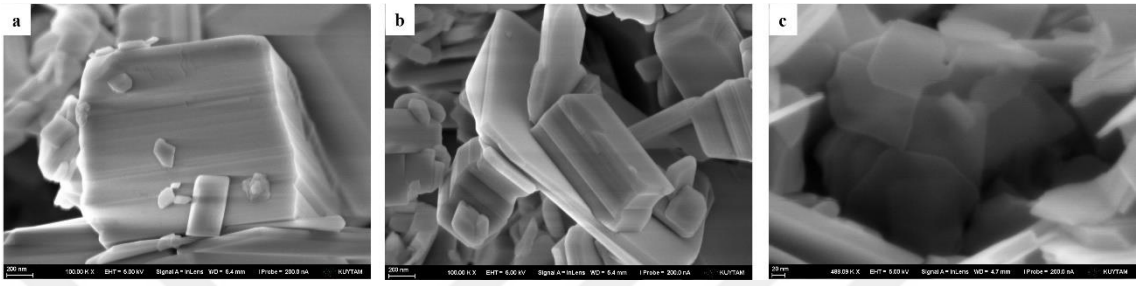

Figure 4.8 SEM images $CsCa_2Ta_3O_{10}$ of **(a)** original, **(b)** protonated, and **(c)** re-stacked version.

SEM images were analyzed with 200.00 KX magnification and 5.00 kV. Figure 4.9 illustrates that SEM analysis revealed no metallic Palladium particles in the doped catalyst. This observation aligns with the results from XPS analysis, which likely did not detect signals for metallic Pd. The morphology of the Pd-doped samples remained similar to their undoped counterparts. Consequently, Pd atoms have likely been incorporated into the material's structure as isolated single atoms rather than forming separate metallic Pd clusters.

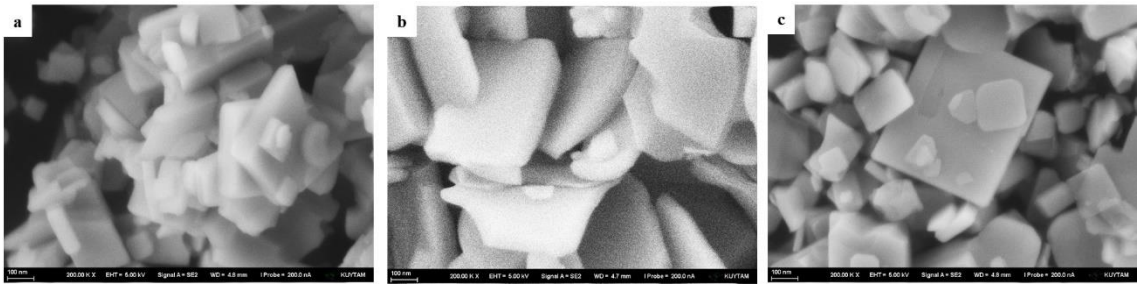

Figure 4.9 SEM images $CsCa_2Ta_3O_{10}$ doped with **(a)** %1.5 Pd, **(b)** %3 Pd, and **(c)** %5 Pd.

4.3.6 Inductively Coupled Plasma Mass Spectrometry (ICP-MS)

ICP-MS was used to quantify the palladium (Pd) amount incorporated into the material's B-sites (Ta sites). As shown in Table 4.1, the difference between the theoretical and experimentally measured Pd weight percentages (wt.%) obtained by ICP-MS increases

with higher theoretical Pd loadings. This discrepancy likely arises from factors like uneven Pd distribution, incomplete doping during synthesis, limitations of the measurement technique, or losses during material processing. Nevertheless, despite these variations in the measured Pd content, ICP-MS analysis confirms the low levels of Pd incorporated into the material.

Table 4.1 Pd loading weight percent (wt. %) of tantalum based layered perovskite by ICP-MS measurements.

Sample	Pd loading % (theoretical)	Pd loading % (ICP-MS)
1.5% Pd-CLTO	0.525	0.203
3% Pd-CLTO	1.053	0.712
5% Pd-CLTO	1.764	0.786

4.3.7 The Brunauer-Emmett-Teller (BET) analysis

Table 4.2 summarizes the specific surface areas of the bulk $CsCa_2Ta_3O_{10}$, exfoliated $[Ca_2Ta_3O_{10}]^-$, and 1.5% Pd doped exfoliated powder, determined using the BET theory. As illustrated in Figure 4.8, the exfoliation process significantly increases the surface area of the powder compared to the non-exfoliated counterpart. This increase is roughly tenfold. The greater the surface area, the higher the number of active sites accessible for reactions, leading to improved catalyst efficiency [139]. This result was consistent with the photocatalytic hydrogen generation experiment.

Table 4.2 Specific surface areas of $CsCa_2Ta_3O_{10}$**,** $[Ca_2Ta_3O_{10}]^-$**,** $[Ca_2Ta_{3-x}Pd_xO_{10}]^-$

Sample	Specific Surface Area / $m^2 g^{-1}$
CCTO	2.3830
CTO	21.7117
1.5% Pd- CTO	22.4620

4.4 Results of Photoelectrochemical Experiments

4.4.1 Chronoamperometry (CA)

Chronoamperometry was employed to evaluate photocurrent generation, monitor photocurrent stability investigate charge separation. Chronoamperometry (CA) was employed to evaluate photocurrent generation, monitor photocurrent stability, and investigate charge separation. CA results are presented in Figure 4.10, where the photocurrent densities of all the analyzed samples were evaluated under full spectrum at a constant potential of 1V vs. SCE (Sat'ed KCl). The experiment noted a consistent rise in photocurrent density, ranging from original to exfoliated structure. Moreover, the Substitution of Pd with Ta allowed the creation of an isolated atom site on the surface, creating single-atom active sites on the surface. This introduction of isolated active sites is believed to be responsible for the increased photocurrent.

Furthermore, introducing protons and water molecules in the bulk form can improve photocurrent by separating electron-hole pairs, acting as Brønsted-Lowry acid donors [140], and reducing electron-hole attraction, thereby increasing photogenerated charges as given in Figure 4.10.a. Additionally, ultrathin nanosheet materials exhibit a shorter charge travel distance due to their high surface area [141]. This minimization of the distance that photogenerated electron-hole pairs can travel reduces the probability of recombination and is predicted to lead to an increase in photocurrent ultimately in Figure 4.10.b.

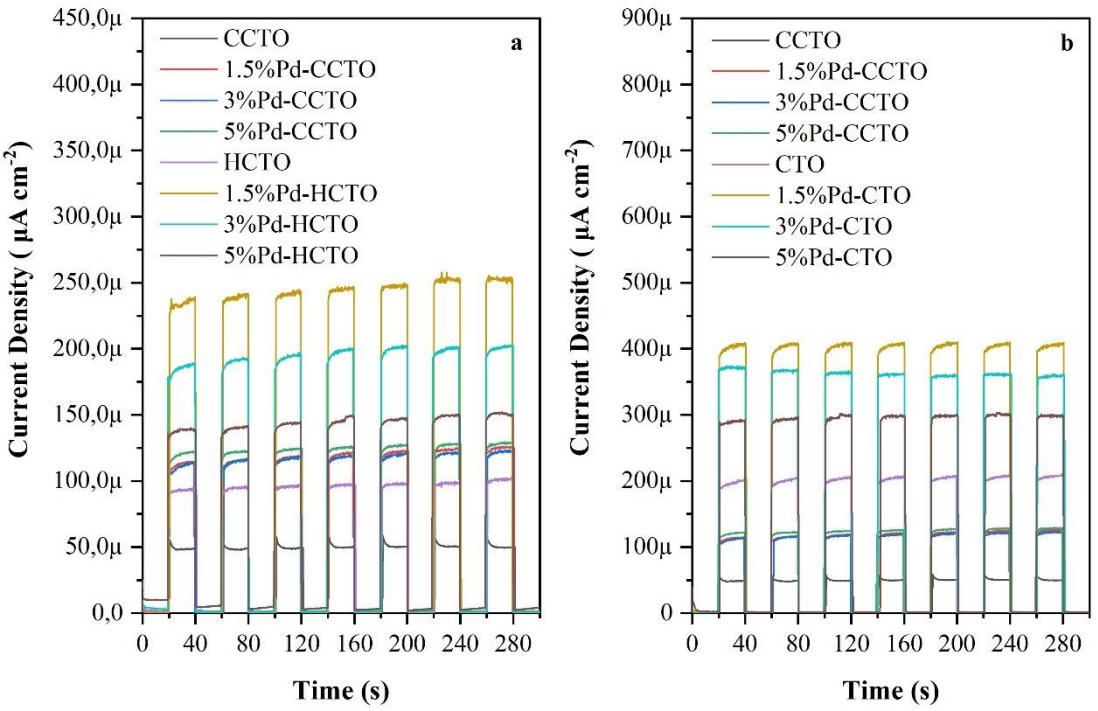

Figure 4.10 Chronoamperometry measurements of **(a)** original and protonated versions of both undoped and doped Pd CCTO and **(b)** original and exfoliated versions of both undoped and Pd doped CCTO at 1V vs SCE (sat'ed. KCl) under full spectrum.

A comparison of the photocurrent of samples with different Pd dopant amounts and phases is shown in Figure 4.11 below. According to this result, the photocurrent decreases with the increase in Pd. Nevertheless, all Pd dopes produced more photocurrent for all cases of pure phase.

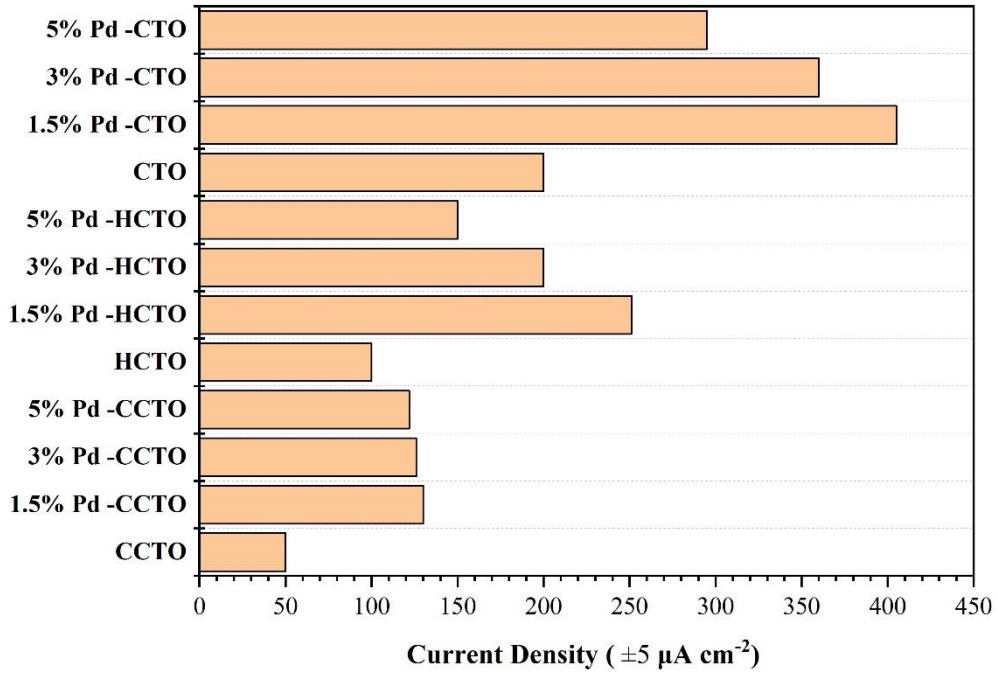

Figure 4.11 Photocurrent values of nonmodified, protonated, and exfoliated derivatives of all doped and undoped.

4.4.2 Potentiostatic Electrochemical Impedance Spectroscopy (PEIS)

Electrochemical Impedance Spectroscopy (EIS) with Nyquist plots is a valuable technique for investigating the electrochemical behavior at the interface between an electrolyte and an electrode [142]. The characteristic semicircle observed in the Nyquist plot provides insights into the charge transfer resistance at the interface. A larger semicircle diameter typically indicates a higher charge transfer resistance caused by decreased free electrons [143]. The EIS results indicated that the pure phases of the material exhibited high resistance due to the limited availability of mobile charge carriers, as illustrated in Figure 4.12. It is hypothesized that doping with Pd introduces additional electronic states within the bandgap, potentially increasing the concentration of mobile electrons and conductivity [144].

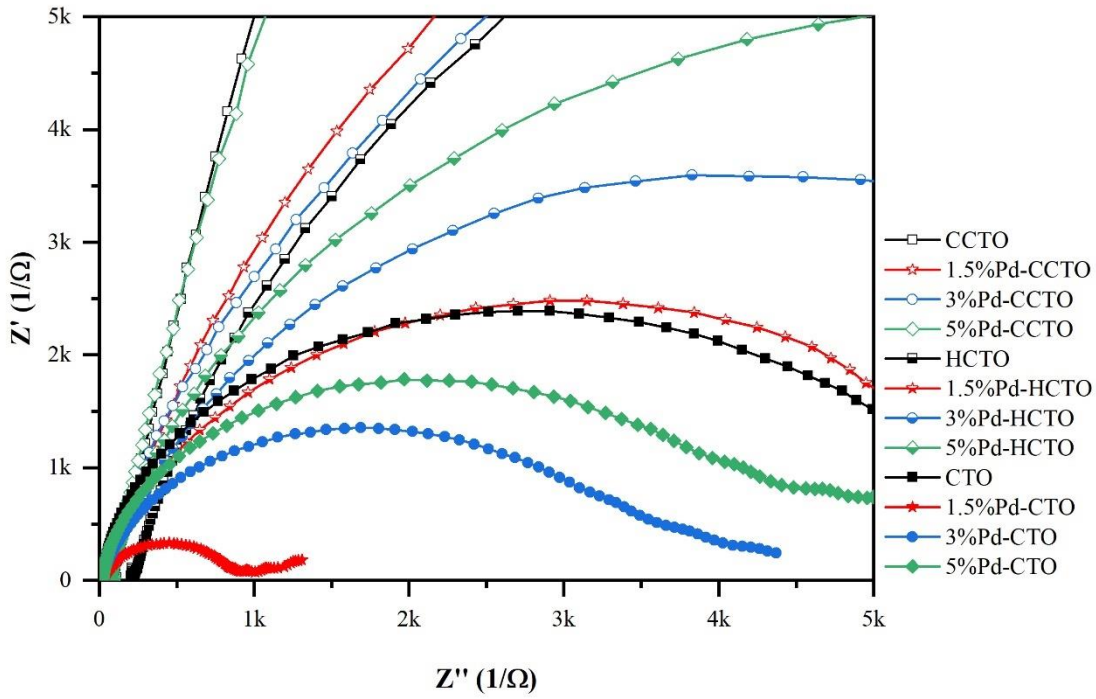

Figure 4.12 Nyquist Electrochemical impedance spectra of undoped of original phase, protonated phase, and exfoliated phase and their Pd doped counterparts.

4.5 Photocatalytic Hydrogen Production

Figure 4.13 depicts the results of a study exploring the photocatalytic generation of hydrogen gas using different forms of $CsCa_2Ta_3O_{10}$ (CCTO). The experiment utilized full-spectrum irradiation for five hours to evaluate the performance of undoped CCTO compared to its doped and derivative variants. The samples included bulk, protonated, and exfoliated variants of CCTO. Deionized (DI) water with 10% methanol served as the reaction medium, with methanol acting as a hole scavenger. Notably, no additional co-catalyst was employed in this experiment, as the introduction of palladium (Pd) dopants within the CCTO structure was believed to provide co-catalytic functionality. The results revealed that unmodified CCTO exhibited limited efficiency, producing only 1.3 micromoles of hydrogen gas per gram (µmol/g). Structural modifications, however, demonstrably enhanced performance. Protonation, a process involving the introduction of protons, yielded a significant improvement, with the protonated HCTO variant

generating 16 µmol/g of hydrogen gas. Similarly, the exfoliated CTO exhibited a further increase in hydrogen production, reaching 210 µmol/g.

In pursuit of further performance optimization, all samples – undoped, protonated, and exfoliated – underwent an additional modification involving palladium (Pd) doping. This strategy involved substituting tantalum (Ta) atoms within the CCTO structure with Pd atoms. The 1.5% Pd-doped and restacked samples (1.5% Pd CTO) were the most efficient hydrogen production materials, exhibiting a nearly four-fold improvement compared to the unmodified CTO, as shown in Figure 4.13. Additionally, doping with Pd at concentrations of 3% and 5% resulted in substantial enhancements in hydrogen production. These Pd-doped variants presented similar production levels exceeding those of the undoped counterpart by factors of the nearest 3.6 and 3 times, respectively.

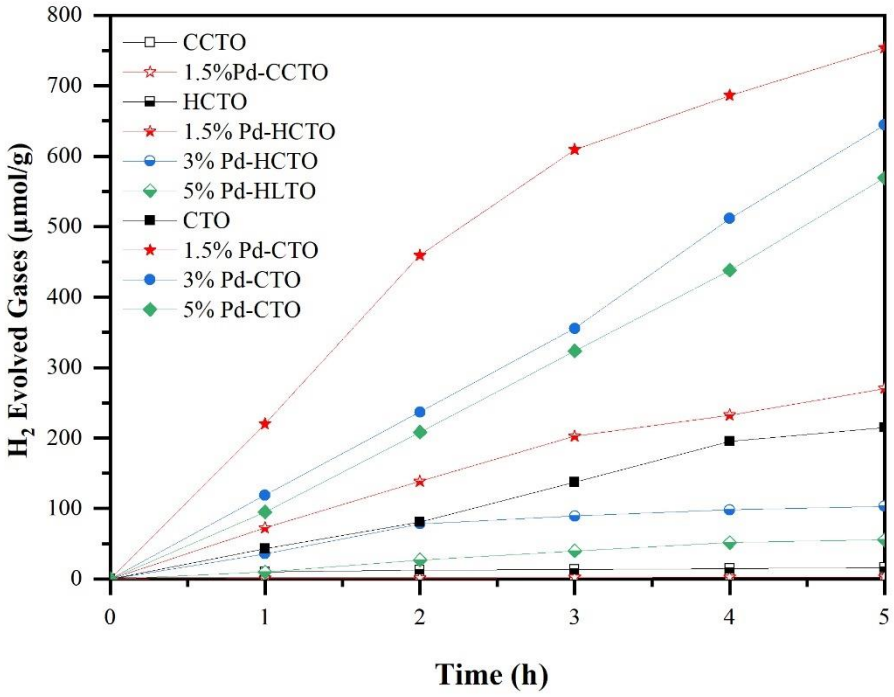

Figure 4.13 The photocatalytic hydrogen evolution activity of undoped and doped $CsCa_2Ta_3O_{10}$ in the form of parent, protonated, and layered nanosheets.

In light of these findings, a 1.5% Pd addition represented the optimal level. It is hypothesized that as the Pd concentration increases, a decline in efficiency is likely due to the formation of defect regions or the aggregation of particles within the structure.

Figure 4.14 likely visually represents this relationship between the photocatalytic hydrogen production capacity and the photocurrent density observed in the PEC experiment. Based on the literature, a higher photocurrent signifies the generation of more free electrons within the material, which can then participate in the HER reaction [145]. When the results were examined, it was seen that the material with the highest hydrogen production was the material that gave the highest photocurrent.

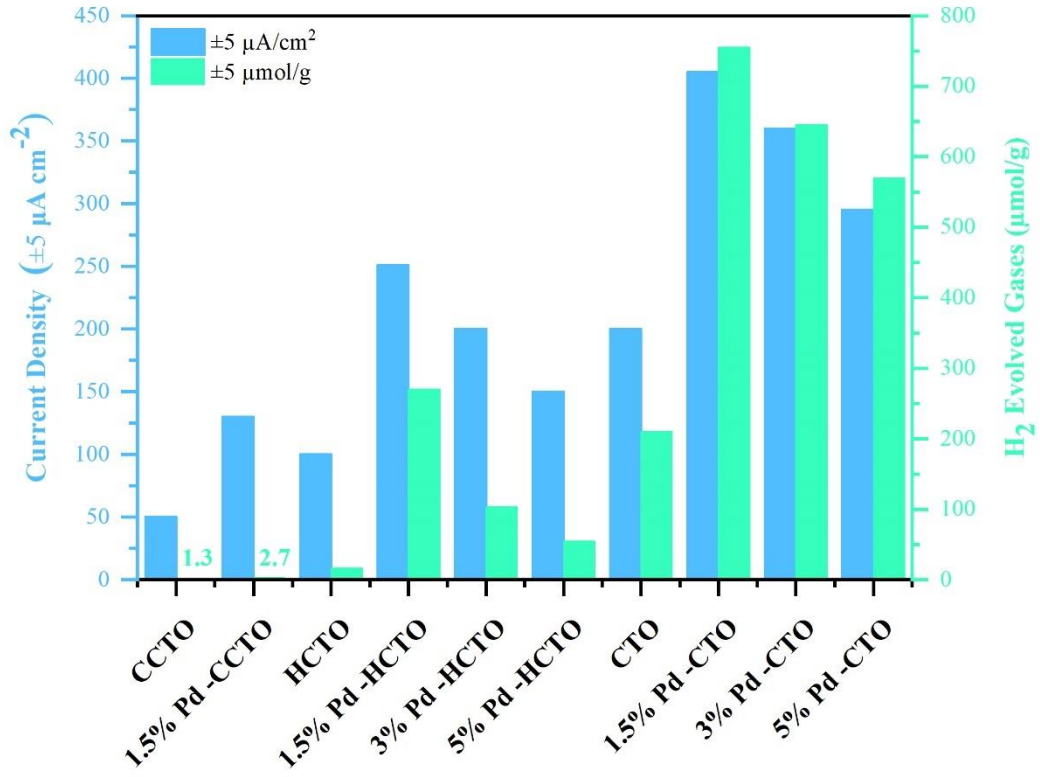

Figure 4.14 The relation between the photocatalytic hydrogen production capacity and photocurrent density in the photoelectrochemical experiment for undoped and doped CCTO and their different forms.

The investigation assessed the stability of CCTO in its bulk, protonated, restacked powder, and 1.5% Pd-doped derivative forms over a fifteen-hour experiment. To further evaluate the reusability of the photocatalyst and stability of the photocatalyst's hydrogen production over multiple uses, a separate three-cycle experiment was conducted (Figure 4.15). Before each cycle, the accumulated hydrogen gas within the reaction cell was evacuated with argon. Subsequent stability testing demonstrated that the photocatalyst

powder exhibited consistent hydrogen production levels even after undergoing three consecutive cycles. This observation indicates the potential for the material to be reused.

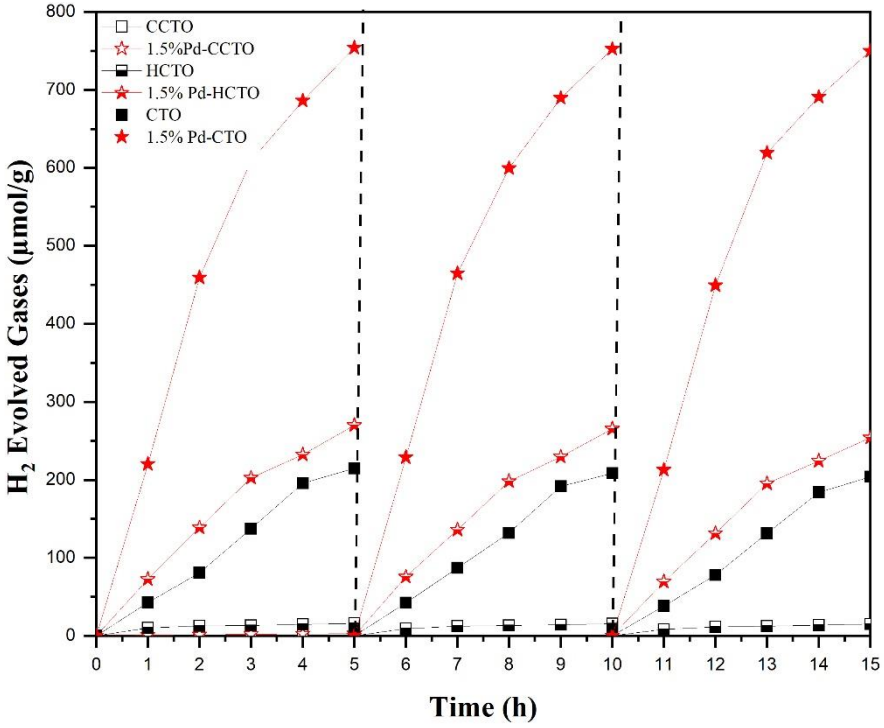

Figure 4.15 Stability test of photocatalytic hydrogen evolution for $CsCa_2Ta_3O_{10}$ (CCTO) and 1.5% Pd- $CsCa_2Ta_3O_{10}$ along with other derivations (protonated HCTO or exfoliated CTO)

4.6 Conclusions

This chapter describes the successful synthesis of $CsCa_2Ta_3O_{10}$ (CCTO) and its Pd-doped counterparts (1.5%, 3%, and 5%) using the Pechini method. A protonated version ($HCa_2Ta_3O_{10}$) was obtained through a proton exchange process involving Cs^+ and H^+. The exfoliation process was applied to the protonated powder following proton exchange to produce its nanosheet variant.

The synthesized materials were comprehensively characterized using various techniques to understand their structural and morphological properties, optoelectronic behavior, and photoelectrochemical performance. X-ray diffraction (XRD) confirmed the successful synthesis of all doped and undoped CCTO samples without impurities. Raman

spectroscopy corroborated the expected crystal structure of CCTO and its Pd-doped variants, which were identified by characteristic vibration peaks consistent with reported literature values. Additional peaks around 650 cm^{-1} in the protonated samples suggest successful Pd intercalation within the structure.

Scanning electron microscopy (SEM) analysis revealed the layered nature of all CCTO variants. In particular, the exfoliated form exhibited a more pronounced layered morphology compared to the non-exfoliated counterparts. No metallic Pd particles were observed, consistent with the XPS results. This suggests the incorporation of Pd as isolated single atoms within the structure rather than as separate clusters.

X-ray photoelectron spectroscopy (XPS) analysis confirmed all samples' +5-oxidation state of Ta atoms. While Pd doping caused minimal changes in binding energy, protonation shifted these values slightly, reflecting altered electron distribution and electrostatic interactions. While XPS analysis could not directly detect low levels of Pd, inductively coupled plasma mass spectrometry (ICP-MS) successfully quantified palladium (Pd) even at this study's lowest doping concentration of 1.5%.

The photoelectrochemical properties of the samples were examined using chronoamperometry (CA) and electrochemical spectroscopy (EIS). The results indicated a consistent rise in photocurrent density, with the highest values observed for the exfoliated structure. This increase is likely due to the shorter charge travel distance in ultrathin nanosheet materials with high surface area, as demonstrated by BET analysis. The reduction in distance minimizes the probability of recombination and leads to increased photocurrent. Substituting Pd with Ta allowed the creation of isolated atom sites on the surface, resulting in increased photocurrent. A comparison of samples with different Pd dopant amounts revealed that photocurrent decreases with increasing Pd content. However, all Pd-doped samples produced more photocurrent compared to the pure-phase samples in all cases. EIS provided complementary information on charge transfer resistance at electrode-electrolyte interfaces. The higher resistance observed in the pure phases suggests that the mobile charge carriers are limited, while the introduction of Pd might enhance the concentration and conductivity of the electrons.

This study also evaluated the photocatalytic production of hydrogen gas from a 10% methanol-water mixture, using gas chromatography to quantify the hydrogen produced.

The study found that unmodified CCTO exhibited limited efficiency, but structural modifications improved performance. Protonation and exfoliation of CCTO led to significant increases in hydrogen production. The 1.5% Pd-doped and restacked samples exhibited the most efficient hydrogen production, a nearly four-fold improvement compared to the unmodified CTO. The highest photocurrent density was observed in the material with the highest hydrogen production. The study also assessed the stability of CCTO in its bulk, protonated, restacked powder, and 1.5% Pd-doped derivative forms.

Chapter 5: Improved Hydrogen Generation via Singular-Atom Palladium Loaded Nanosheets Derived from Two Layered Dion Jacobson Layered Perovskites Oxide

5.1 Introduction

As fossil fuels threaten the environment, new materials are being developed to replace them for sustainability. One of the most studied material types in the literature is photocatalysts, considering their appeal to working with solar power. Among these photocatalysts, layered perovskite oxides (LPOs) have desired properties such as their flexible interlayer, allowing exfoliation into nanosheets, and their tunable band gap. The modifiable interlayer of these LPOs results from the electrostatically bonded cations in the interlayer. By proton exchange with acids that replace the interlayer cations with protonated water molecules [146]. The proton exchange step further enhances the photocatalytic performance with the captured water molecules in the interlayer. Exfoliation with sterically big/hindered cations such as tetrabutylphosphonium hydroxide (TBPOH), and tetrabutylammonium hydroxide (TBAOH), LPOs can be turned into 2D NSs. Exfoliated NSs are the end goal in this process as they have maximum surface area and short migration distance for electrons to participate in the surface reactions. The short migration distance provided by NSs also helps to reduce the recombination of the electrons thus, increasing the rate of electrons participating in the surface reactions.

A critical way of enhancing photocatalytic activity is by single-atom catalysts (SACs), introduced by Zhang et al. in 2011[147]. This method of doping metals into the material is superior to doping metals as co-catalysts as it helps to utilize more metal atoms in photocatalytic reactions by using more of them as reaction sites. SACs doping is crucial to be more sustainable as the noble metals used as dopants for photocatalytic reactions are scarce and expensive. Another advantage of SACs doping is that when the layered perovskite is exfoliated, dopant atoms in the interior part of the bulk material are also exposed to participate in surface reactions. By having few-layered NS structures, nearly all of the dopant atoms can be made to participate in photocatalytic reactions.

Building on the findings discussed earlier, this study investigated the use of palladium (Pd) as single-atom catalysts (SACs) with varying doping levels within the tantalum (Ta) sites of three different materials: CLTO, HLTO, and LTO. The research focused on evaluating their photocatalytic efficiency for hydrogen production. The results revealed that 1.5% Pd-doped LTO significantly outperformed the other materials, generating 2.5 times more hydrogen than its protonated version and 30 times more hydrogen than undoped protonated crystal.

5.2 Experimental Procedure

The experimental part is explained in detail in chapter 2.

5.3 Result and Discussion

5.3.1 X-Ray diffraction Spectroscopy (XRD)

Figure 5.1.a presents the X-ray diffraction patterns of two materials: the original $CsLaTa_2O_7$ and its palladium-doped counterpart (Pd-doped CLTO). The XRD pattern of synthesized undoped and doped CLTO samples perfectly matched the reported structure for a two-layered tantalum-based oxide. This material exhibits tetragonal symmetry with a P4/mmm space group, as documented in the literature [62]. XRD analysis reveals no impurity phases in samples, including those with palladium doping. Following proton exchange, the crystal symmetry of the original material and its palladium-doped variant undergoes alteration. This change is evident in the transition to space group I4/mmm [148], as depicted in Figure 5.1.b.

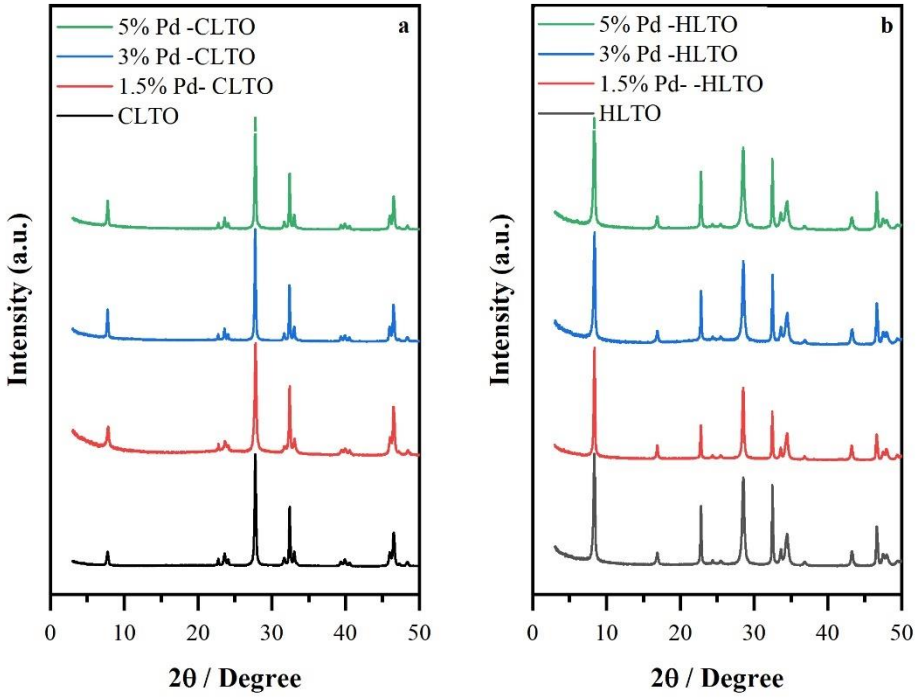

Figure 5.1 : XRD pattern **(a)** $CsLaTa_2O_7$ (CLTO) and their Pd doped counterparts (b) $HLaTa_2O_7$ (HLTO) and their Pd doped counterparts.

5.3.2 Raman Spectroscopy

Raman spectroscopy is an analysis technique that utilizes light scattering to analyze a material's unique properties based on the specific frequencies at which its chemical bonds vibrate [149]. When elements are doped into the material, they can modify their chemical surroundings, impacting bond strength and vibrational frequencies. The introduced element can lead to shifts in existing Raman peaks or the presence of entirely new peaks in the spectrum, as shown in Figure 5.2. In this case, the addition of Pd resulted in new peaks around 650 cm^{-1} and 427 cm^{-1}, which can be attributed to the B_1g and Eg vibrational modes of the tetragonal phase of Pd-O [150]. This observation strongly suggests the incorporation of palladium into the structure. Furthermore, the exchange of Cs^+ with H_3O^+ caused a shift of the peak at 920 cm^{-1} to a higher wavenumber with weakened intensity. This shift likely occurs because the change in interlayer species alters the bonding environment and vibrational frequencies within the material.

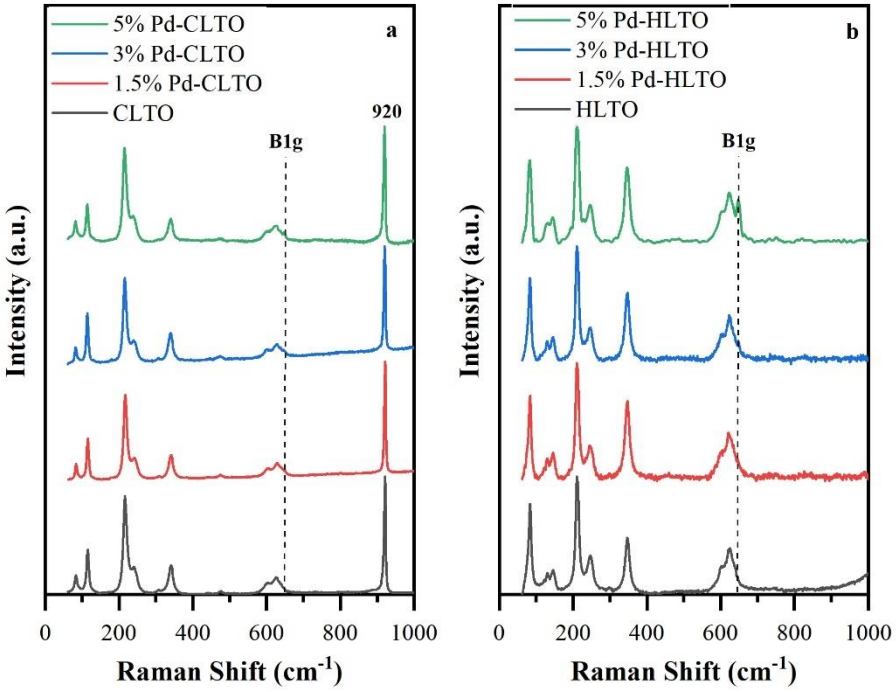

Figure 5.2 Raman Spectrum of **(a)** $CsLaTa_2O_7$ and their Pd doped version **(b)** $HLaTa_2O_7$ and their Pd doped version.

5.3.3 Ultraviolet-visible (UV-vis) Diffuse Reflectance Spectroscopy

The materials' absorbance properties and bandgap energies were characterized using UV-vis diffuse reflectance spectroscopy. Figure 5.3.a illustrates the absorption spectra of the pristine sample and the protonated variant. The absorption spectrum of the pristine sample exhibits an edge at approximately 290 nm, while the protonated variant displays an edge at 310 nm. These observations indicate that proton exchange has increased slightly the absorption behavior. These absorption edges are believed to be caused by electrons jumping from oxygen (O 2p) orbitals in the material's valence band to tantalum (Ta 5d) orbitals in the conduction band [49]. The Tauc method helped calculate materials' band gap energies (Eg). This method relies on UV-vis absorption data and involves plotting a transformed Kubelka-Munk function, $[F(R)hv]^{(1/\eta)}$, against the energy of light particles (photons, hv). In this case, the parameter η is set to 2, as it corresponds to an indirect transition between electronic bands [151]. In Tauc plots, the band gap energy of each material is determined at the point where the extrapolated linear portions of the absorption

curve (y-axis) and the energy axis (x-axis) intersect. Based on the calculated band energies shown in Figure 5.3.b, the bandgap energies for CLTO, 1.5%-Pd CLTO, 3%-Pd CLTO, 5%-Pd CLTO, HLTO, 1.5%-Pd HLTO, 3%-Pd HLTO, and 5%-Pd HLTO were calculated to be 4.169, 4.149, 4.182, 4.187, 4.197, 4.063, 4.073, and 4.000 eV, respectively. Since the Pd loading caused a minimal red shift on the absorbance spectrum (Figure 5.3.a), it did not significantly affect the band gap narrowing.

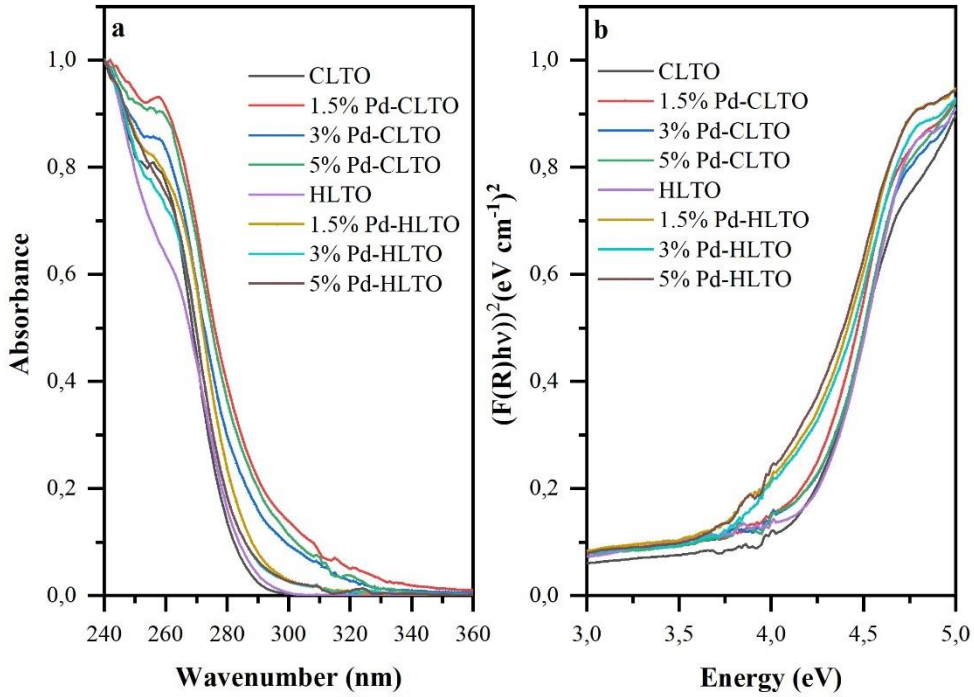

Figure 5.3 (a) UV-vis absorption spectra of pure and protonated of $CsLaTa_2O_7$ and their different loading of Pd-doped versions, and **(b)** Kubelka Munk curve of pure and protonated of $CsLaTa_2O_7$ and their different loading of Pd-doped versions for calculation of band energies.

5.3.4 X-ray Photoelectron Spectroscopy (XPS)

Ta 4d spectra were deconvoluted into two peaks. 239.9 eV ($4d_{3/2}$) and 228.8 eV ($4d_{5/2}$) in Figure 5.4**.** Also, these peaks are attributed to electrons belonging to Tantalum atoms that are present in a +5 oxidation state. After Pd doping, these peak centers moved slightly to higher binding energies. The movement suggests that Palladium atoms have been added to the structure of the crystal [152]. Moreover, the protonation process caused an increase in binding energies due to a change of space group and hydrogen bonding between oxygen and hydrogen.

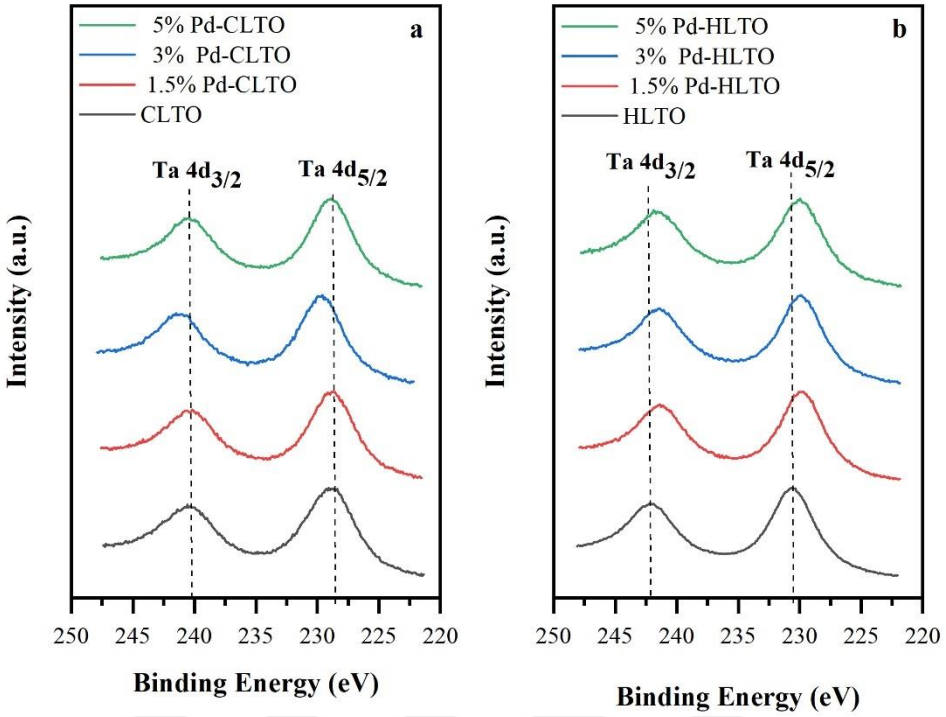

Figure 5.4 XPS binding energy spectra of Ta 4d (a) pure and 1.5%, 3% and 5% Pd doped of CLTO and (b) pure and 1.5%, 3% and 5% Pd doped of HLTO.

The O 1s peaks were observed in the crystal structure asymmetry, and the analysis of these peaks through Gaussian fitting revealed two or three distinct contributions corresponding to different oxygen chemical states. Regarding Figure 5.5, the lowest peak at 529 eV typically originates from O^{2-} ions or lattice oxygen. The peaks at higher energies, around 530.0 eV, are attributed to oxygen-deficient regions, such as oxygen vacancies. The highest peaks at 531 eV are associated with chemisorbed oxygen on the surface structure. As illustrated in Figure 5.4, a comparable shift was observed for tantalum (Ta 4d) electrons. Similarly, the analysis of oxygen (O 1s) electrons in the protonated material revealed a shift towards higher binding energies than their bulk version.

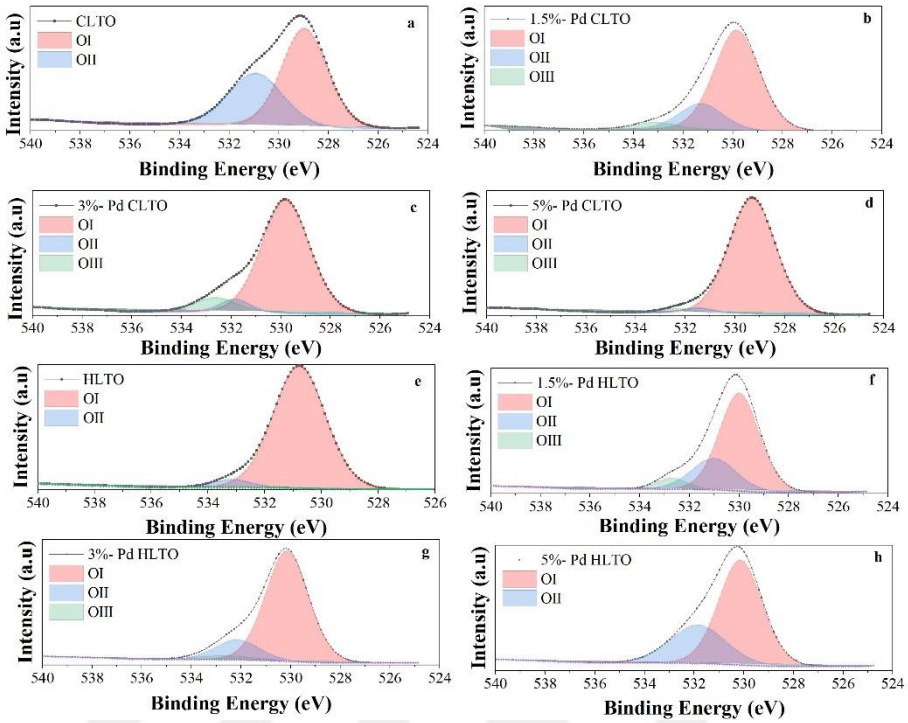

Figure 5.5 XPS binding energy spectra of O 1s **(a)** CCTO **(b)** 1.5% Pd-CLTO, **(c)** 3% Pd-CLTO, **(d)** 5% Pd-CLTO, **(e)** HLTO, **(f)** 1.5% Pd-HLTO, **(g)** 3% Pd-HLTO and **(h)** 5% Pd-HLTO.

Figure 5.6 illustrates the Pd 3d X-ray photoelectron spectroscopy analysis for 5% Pd-doped CLTO. The Pd 3d spectra were analyzed to reveal two distinct peaks: one at 335 eV corresponding to Pd $3d_{5/2}$ and another at 340 eV corresponding to Pd $3d_{3/2}$.These peaks confirmed that it was in the +2-oxidation state concerning 284.4 eV of C 1s. No typical diffraction peaks of Pd were detected for 3% and 1.5% Pd-doped CLTO catalysts. Therefore, inductively coupled plasma mass spectrometry served as an analytical tool to verify the incorporation of palladium within the crystal lattice at lower doping levels (below 5%) within the crystal structure.

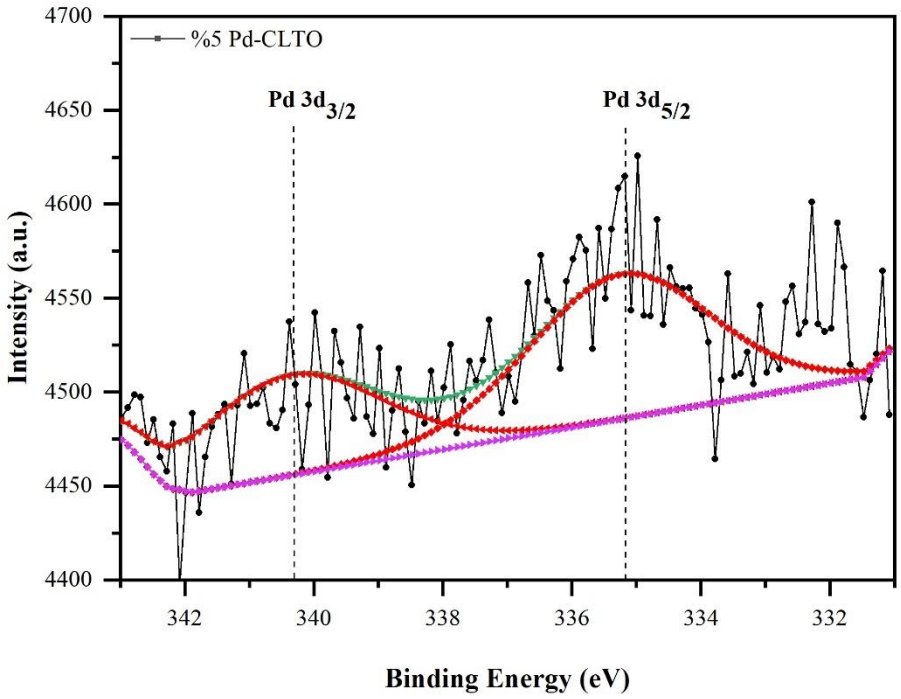

Figure 5.6 XPS binding energy spectra of Pd 3d pure for %5 Pd doped CLTO.

Figure 5.7 shows the energy levels for both undoped and noble doped catalysts before and after protonation. Kubelka-Munk analysis using UV-vis DRS to determine the bandgap and measurement of the VBM using XPS was used together to create the material's electronic structure. Among all the analyzed catalysts, the protonated sample containing 1.5% Pd exhibits the most negative conduction band maximum (CBM) position, as evident in Figure 5.7. A more negative CBM position is known to enhance hydrogen production efficiency. The observation from this analysis is in excellent agreement with the outcomes of the photocatalytic experiments, making the connection between a material's electronic structure and its ability to generate hydrogen even more straightforward.

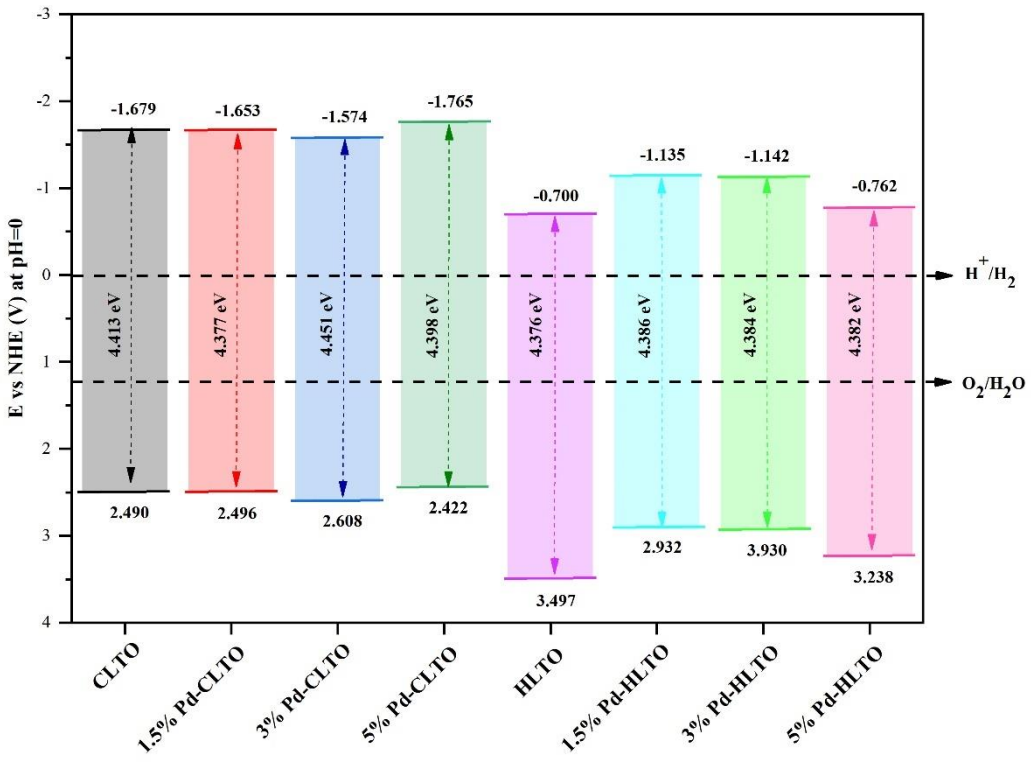

Figure 5.7 Schematic diagram of band energies for undoped and doped of CLTO and HLTO

5.3.5 Scanning Electron Microscopy (SEM)

SEM was employed to examine the surface morphology of the samples. The instrument used was a Zeiss Ultra Plus field emission scanning microscope, capable of magnifications up to 100.00 KX at an acceleration voltage of 5 kV. As illustrated in Figure 5.8, the analysis confirms that all material variations possess a layered structure. Furthermore, this layered characteristic is considerably more pronounced in the exfoliated version (Figure 5.8.c) compared to the non-exfoliated samples (Figure 5.8.a). This enhanced visibility is likely a consequence of the atomic-scale thinness of the exfoliated material, allowing for more apparent observation of the individual layers.

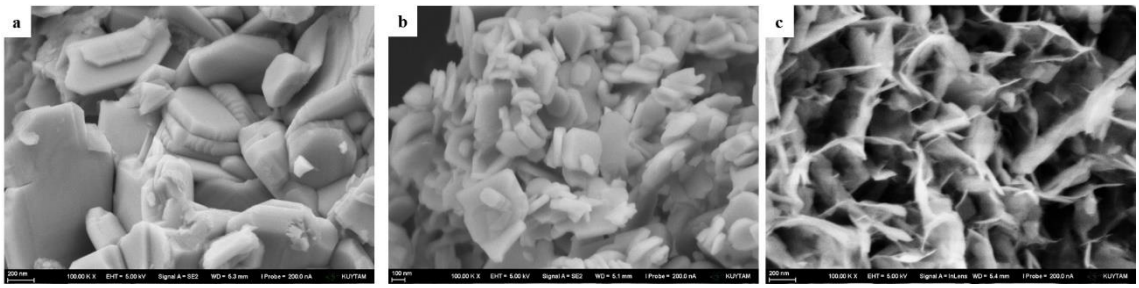

Figure 5.8 SEM images $CsLaTa_2O_7$ of (a) original, (b) protonated, and (c) re-stacked version.

Figure 5.9 displays the evidence for successful palladium (Pd) incorporation. No metallic Pd particles were observed within the noble doped catalyst, which aligns well with the XPS results that likely lacked signals for metallic Pd. This suggests that the Pd-doped samples' morphology, shape, and structure remained similar to their undoped counterparts. Consequently, these observations are collectively believed that Pd atoms are likely incorporated into the material's structure as isolated single atoms rather than forming separate metallic Pd clusters.

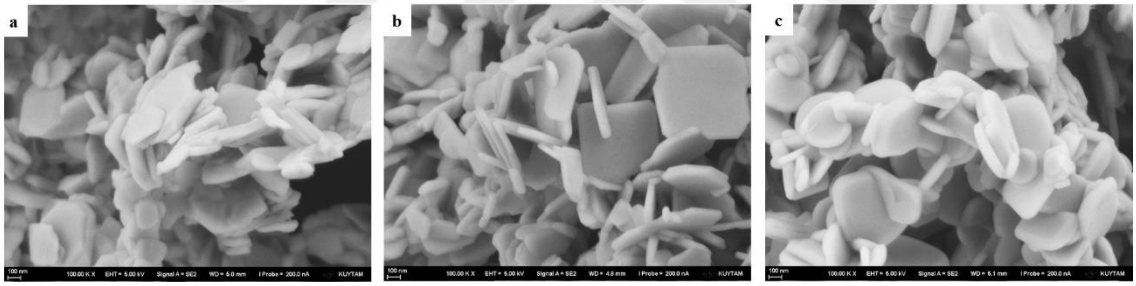

Figure 5.9 SEM images $CsLaTa_2O_7$ doped with **(a)** %1.5 Pd, **(b)** %3 Pd, and **(c)** %5 Pd.

5.3.6 Inductively Coupled Plasma Mass Spectrometry (ICP-MS)

The incorporation of palladium (Pd) metal into the material's B-sites (Ta sites) was quantified using Agilent 7700x inductively coupled plasma-mass spectrometry (ICP-MS). Table 5.1 shows that the difference between the theoretical and experimentally determined Pd weight percentages (wt.%) by ICP-MS increases with higher theoretical Pd loadings. This discrepancy might be due to uneven Pd distribution, incomplete doping, measurement limitations, or losses during material processing. However, despite these discrepancies in the measured Pd amount, ICP-MS analysis confirms the low levels of Pd incorporation into the material.

Table 5.1 Pd loading weight percent (wt. %) of tantalum based layered perovskite by ICP-MS measurements.

Sample	Pd loading % (theoretical)	Pd loading % (ICP-MS)
1.5% Pd-CLTO	0.429	0.150
3% Pd-CLTO	0.861	0.622
5% Pd-CLTO	1.442	0.675

5.3.7 The Brunauer-Emmett-Teller (BET) analysis

Brunauer-Emmett-Teller (BET) analysis was employed to quantify the specific surface areas of the powdered samples. As anticipated, the study revealed a significant increase in surface area following the exfoliation process. This enhanced surface area can directly contribute to accelerated rates of surface reactions, which are crucial for photocatalytic activity.

The photocatalytic experiments described in Section 5.5 corroborated this notion. Results indicated that reassembled powders, likely possessing higher surface areas due to the exfoliation process, produced more hydrogen than their non-reassembled counterparts. Table 5.2 summarizes the specific surface areas of the original $CsLaTa_2O_7$, exfoliated $LaTa_2O_7$, and 1.5% Pd doped exfoliated $LaTa_2O_7$.

Table 5.2 Specific surface areas of $CsLaTa_2O_7$, $[LaTa_2O_7]^-$, $[LaTa_{2-x}Pd_xO_7]^-$

Sample	Specific Surface Area / $m^2\,g^{-1}$
CLTO	1.2813
LTO	11.7917
1.5% Pd-LTO	17.2088

5.4 Results of Photoelectrochemical Experiments

5.4.1 Chronoamperometry (CA)

Chronoamperometry is a powerful technique for investigating the behavior of charge carrier particles resulting in light irradiation [153]. This method involves measuring the

electrical current flowing through the system as a function of time, usually while applying pulsed light illumination. As illustrated in Figure 5.10, the exfoliated samples displayed a significantly higher initial photocurrent than the protonated and original materials.

This remarkable performance can be attributed to two key factors associated with the exfoliated nanosheets. First, their high surface area offers a significantly greater number of active sites for light absorption and charge generation [154]. Second, the ultrathin nature of these materials leads to a shorter charge carrier diffusion length [155]. This reduced distance that photogenerated electron-hole pairs need to travel before recombination minimizes recombination losses and promotes efficient charge separation and transfer. These factors collectively contribute to the superior photocurrent response observed in the exfoliated samples.

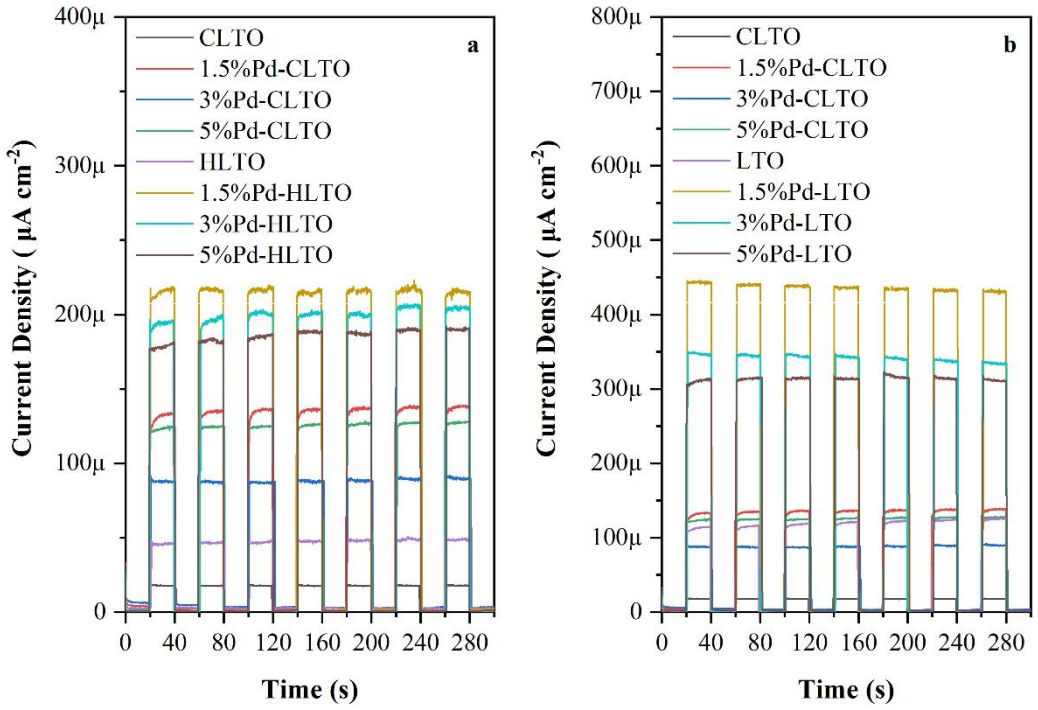

Figure 5.10 Chronoamperometry measurements of **(a)** original and protonated versions of undoped and Pd doped CLTO and **(b)** original and exfoliated versions of undoped and Pd doped CLTO at 1V vs. SCE (sat'ed. KCl) under the full spectrum.

The 1.5% Pd-doped LTO sample showed promising results, as shown in Figure 5.11, suggesting this might be the optimal doping concentration. As observed in CA measurements for the optimal doping concentration, efficient charge separation is crucial for reducing water to hydrogen in photocatalytic applications.

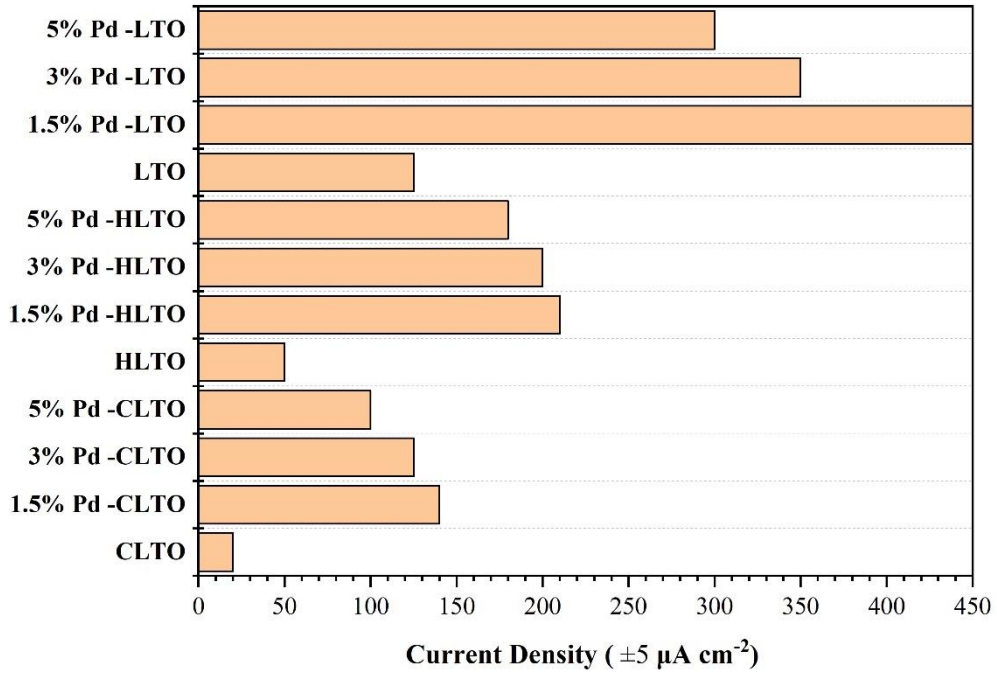

Figure 5.11 Photocurrent values of nonmodified, protonated, and exfoliated derivatives of all doped and undoped.

5.4.2 Potentiostatic Electrochemical Impedance Spectroscopy (PEIS)

Nyquist plots were used to investigate charge transfer kinetics. The diameter of the semicircular feature within this electrochemical impedance spectroscopy Nyquist plot reflects the resistance to electron transfer at the boundary between the electrode and the electrolyte solution [156]. Typically, a smaller semicircle diameter indicates faster charge transfer and more efficient separation of photogenerated electron-hole pairs. In light of this information, nanomaterials with an ultra-thin structure exhibited the lowest charge transfer resistance than their conjugates of the other bulk and protonated states Figure 5.12**.** The short distance that photogenerated charges need to travel facilitates their effective separation. Notably, the 1.5% Pd-doped nanosheet sample exhibits a significantly smaller semicircle arc than the undoped and others with $[Ca_2Ta_3O_{10}]^-$ counterparts. The observed decrease in the arc diameter signifies an enhancement in the charge transfer kinetics at the interface between the photoelectrode and the electrolyte for the 1.5% Pd-doped sample, indicating a more efficient transfer of photogenerated charge carriers than other doped ratios.

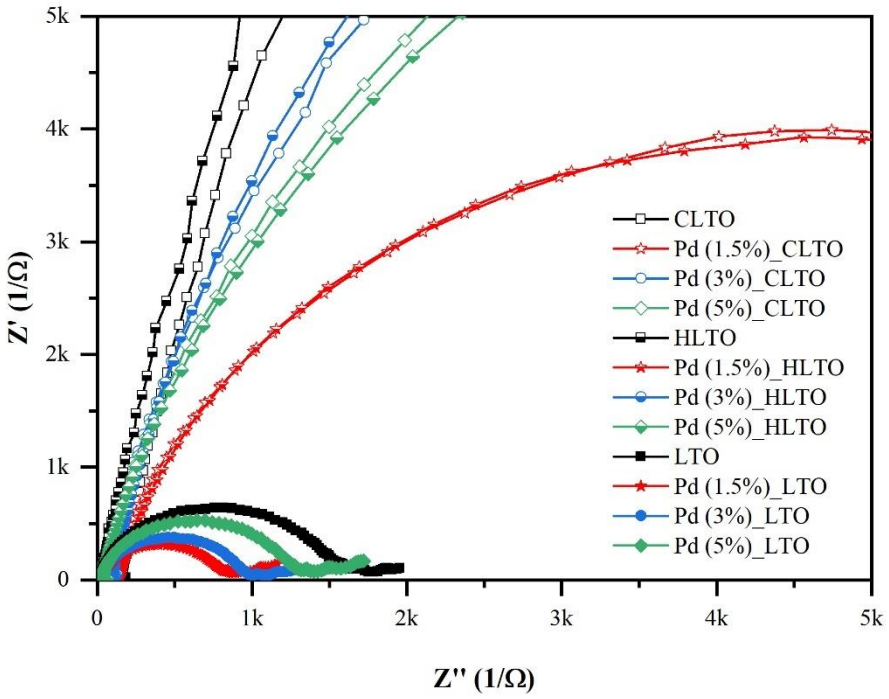

Figure 5.12 Nyquist Electrochemical impedance spectra of undoped of original phase, protonated phase, and exfoliated phase of CLTO and their Pd doped derivatives.

.

5.5 Photocatalytic Hydrogen Production

Figure 5.13 shows the results of photocatalytic hydrogen evolution experiments employed under full-spectrum irradiation for 5 hours to compare the performance of undoped and doped $CsLaTa_2O_7$ (CLTO) and their derivatives in DI water with 10% methanol as a hole scavenger without co-catalyst. While CLTO shows promise for using light to split water and make hydrogen gas, the unmodified version could have been more efficient. It only produced 3.5 micromoles of hydrogen gas per gram (3.5 µmol/g.). Changing the material by adding protons or making it plate-like (protonated and exfoliated versions) resulted in improvements, producing 147 µmol/g and 500 µmol/g. respectively. To further enhance the performance, all samples (undoped, protonated, and exfoliated) underwent an additional modification. This involved introducing palladium (Pd) atoms as dopants, substituting for tantalum (Ta) atoms within the material's structure. After the doping strategy, 1.5% Pd doped restacked samples (1.5% Pd LTO) had the best performance on hydrogen generation, almost ten times than mother phase derivations.

Doping the material with palladium (Pd) at 3% and 5% ratios also significantly increased hydrogen production compared to the bulk undoped versions. Notably, the 3% and 5% Pd-doped samples exhibited six times and four times higher hydrogen production, respectively (in units of µmol/g).

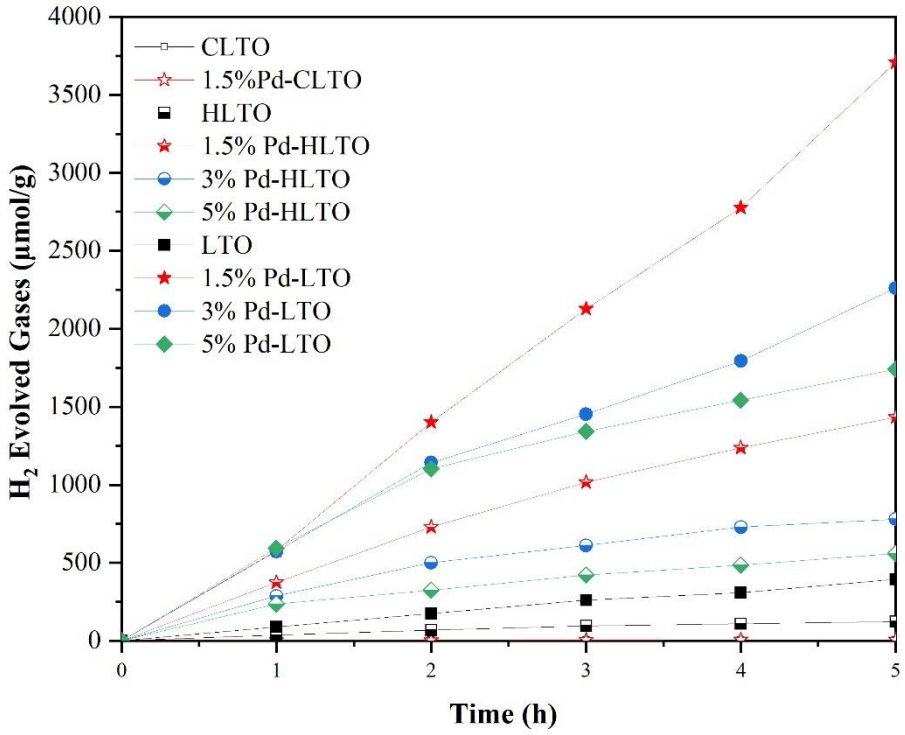

Figure 5.13 The photocatalytic hydrogen evolution activity of undoped and doped $CsLaTa_2O_7$ in the form of parent, protonated, and layered nanosheets**.** The photocatalytic hydrogen evolution activity of undoped and doped. The experiment was conducted in a 5 ml quartz cell under full-spectrum illumination from a 300 W Xenon lamp with 10% v/v methanol as a hole scavenger without co-catalyst.

In a photoelectrochemical (PEC) system for hydrogen evolution (HER), a higher photocurrent is typically interpreted as a higher rate of HER. The higher photocurrent signifies the generation of more free electrons within the material [157], which can then participate in the HER reaction. Figure 5.14 shows the relation between the photocatalytic hydrogen production capacity and photocurrent density in the photoelectrochemical experiment.

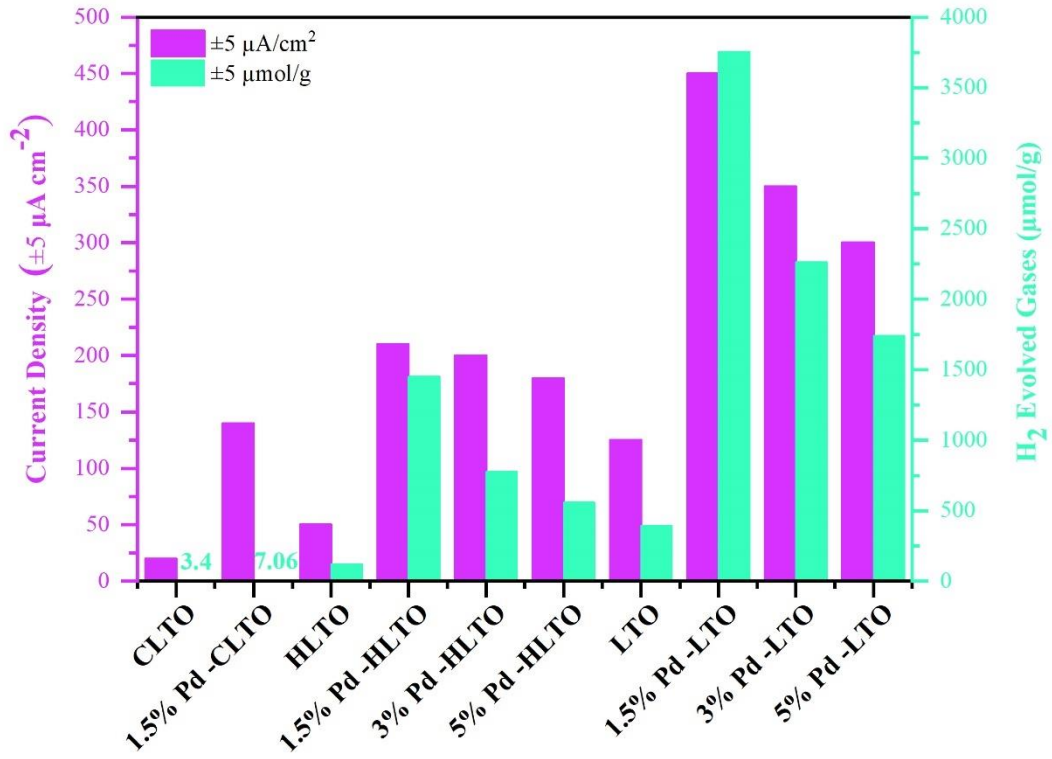

Figure 5.14 The relation between the photocatalytic hydrogen production capacity and photocurrent density in the photoelectrochemical experiment.

The study evaluated the performance of CLTO's bulk, protonated, and restacked powders and 1.5% Pd-doped CLTO derivatives over a 5-hour experiment. Figure 5.15 displays the stability experiment. The test revealed that the photocatalyst powder maintained consistent hydrogen production levels even after three consecutive cycles, demonstrating its reusability.

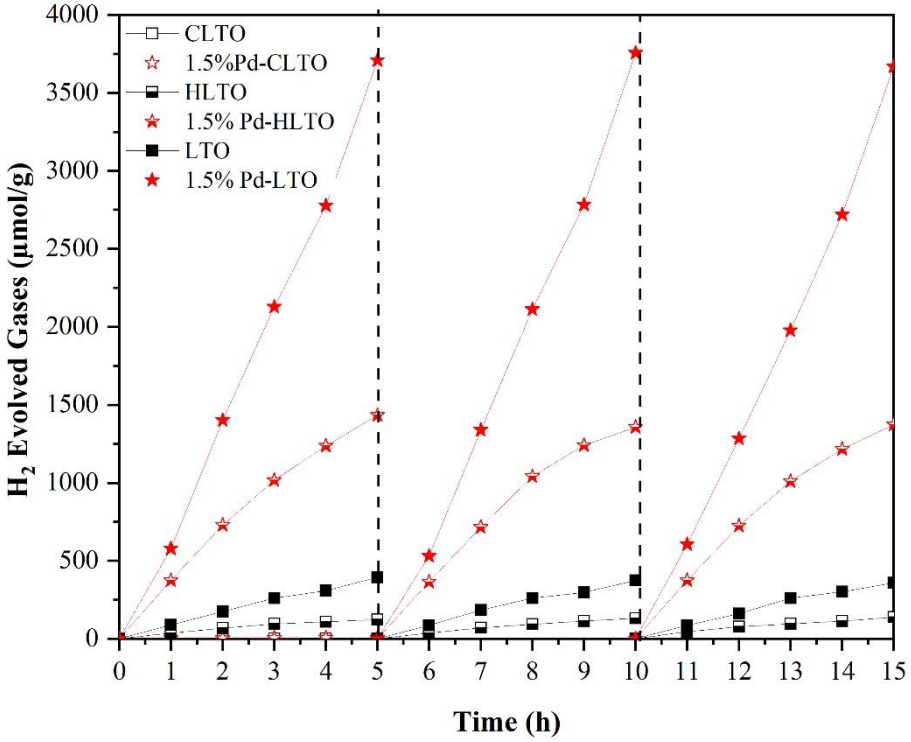

Figure 5.15 Stability test of photocatalytic hydrogen evolution for $CsLaTa_2O_7$ (CLTO) and 1.5% Pd- $CsLaTa_2O_7$ (CLTO) along with other derivations (protonated HLTO or exfoliated LTO)

5.6 Conclusions

This study investigates the structural, morphological, and photocatalytic properties of palladium (Pd)-doped $CsLaTa_2O_7$ (CLTO) and its derivatives. XRD analysis revealed the successful synthesis of CLTO and Pd-doped CLTO, with no evidence of impurity phases. Interestingly, proton exchange leads to a transition in crystal symmetry, as revealed by XRD. Raman spectroscopy further corroborates the successful incorporation of palladium into the material, supported by XPS and ICP-MS analyses.

UV-VIS spectroscopy was employed to analyze the materials' light absorption properties and band gap energies. The Tauc method determined the absorption edges at 290 nm and 310 nm for untreated and treated acid-exchanged samples. Forbidden energies were determined using the Kubelka-Munk function, revealing the minimal influence of Pd loading on band gap narrowing. XPS analysis of the Ta 4d peaks revealed a shift to higher binding energies upon Pd doping, suggesting the successful incorporation of Pd atoms

into the CLTO crystal lattice. Pd 3d XPS analysis for 5% Pd-doped CLTO revealed distinct peaks corresponding to metallic Pd in the +2-oxidation state. Notably, no characteristic diffraction peaks were observed for 3% and 1.5% Pd-doped samples, likely due to their lower Pd content. ICP-MS was a complementary technique to confirm Pd presence for these lower doping levels.

SEM revealed a layered structure for all material variations. However, the exfoliated version exhibited a more pronounced layered morphology due to its atomic-scale thinness. Chronoamperometry, a technique used to study the behavior of light-generated charge carriers, demonstrated that the exfoliated nanosheets exhibited a higher initial photocurrent due to their larger surface area and ultrathin nature, promoting efficient charge separation and transfer with minimal recombination losses. Notably, the 1.5% Pd-doped LTO sample displayed promising results, suggesting an optimal doping concentration for efficient photocatalytic applications. Nyquist plots provided evidence for the enhanced mobility of charge carriers and their efficient separation in ultra-thin nanomaterials, a key factor for efficient photocatalytic activity., with Pd-doped nanosheets showing enhanced charge transfer kinetics at the photoelectrode-electrolyte interface.

The photocatalytic performance was conducted through hydrogen evolution experiments under light irradiation, using deionized water with 10% methanol as the sacrificial agent. While undoped CLTO exhibited some hydrogen production activity (3.5 micromoles of hydrogen per gram of catalyst), significant improvement was observed upon introducing protons or creating a flake-like morphology. It was notable that doping with Pd atoms further enhanced photocatalytic activity. Among all the samples, the 1.5% Pd-doped restacked sample demonstrated the best hydrogen generation performance, exceeding that of the pristine CLTO by nearly tenfold. Additionally, the photocatalyst maintained consistent hydrogen production levels even after three consecutive cycles, highlighting its reusability.

In conclusion, this study successfully synthesized Pd-doped $CsLaTa_2O_7$ derivatives and characterized their structural, morphological, and photocatalytic properties. The incorporation of Pd and the creation of specific morphologies were found to improve the photocatalytic hydrogen evolution performance. The 1.5% Pd-doped restacked sample emerged as the most promising photocatalyst, demonstrating high activity and reusability.

These findings pave the way for developing efficient and durable photocatalysts for hydrogen production from solar energy.

Chapter 6: Improved Hydrogen Generation via Singular-Atom Tin Loaded Nanosheets Derived from Two Layered Dion Jacobson Layered Perovskites Oxide

6.1 Introduction

Overusing fossil fuels significantly threatens sustainable development and worsens environmental issues. Light-activated photocatalysis is a promising technology because it utilizes renewable solar energy to convert water into its constituent elements, oxygen, and hydrogen. Metal oxides with Pt as a co-catalyst are highly used in photocatalytic hydrogen evolution reactions (HER), but their high cost prevents them from being industrialized. It is necessary to develop affordable catalysts with outstanding catalytic performance if this technology is to advance.

The single-atom catalyst (SACs) concept was first presented by Zhang et al. in 2011 [158]. SACs are a metal uniformly distributed on the surface or attached to the framework, thereby expanding atom utilization, and creating a positive activity tendency. This concept makes it a budget-friendly process because each atom can be used as a catalytic reaction center. Most SACs have remarkable catalytic performance, mainly when adsorbed on two-dimensional (2D) substrates [159]. Because the high surface area of NSs allows the dispersal of individual metal atoms and maximizes the accessibility of all metal atoms to reactants. In 2023, T. Üstünel et al. exfoliated bulk-layered titanates (LTs) into few-layer sheets. The exfoliated LTs reported significant photocatalytic activity enhancement (~3.5 mmol/g H_2 in 30 min) by loading at 20 ppm of Sn single atoms, surpassing conventional TiO_2-based photocatalyst [160]. Besides, using Tin as a co-catalyst is a helpful strategy for photocatalysis applications because it is more cost-effective than noble metals like Ru, Pd, and Pt [161]. Y. Akınay, in 2021, synthesized 3D Sn-doped Sb_2O_3 catalysts to investigate effects on the electrocatalytic hydrogen evolution reaction in an acidic medium. The study aims to develop and synthesize low-cost catalysts instead of noble metals that can be used in different pH ranges to produce molecular hydrogen through the hydrogen evolution reaction. Their results documented that

chronoamperometric studies demonstrated high electrode stability and excellent HER performance of the 3D rod-like Sn: Sb_2O_3 particles [162].

This chapter synthesized single-atom Sn-loaded layered tantalate nanosheets by exfoliating a layered perovskite oxide ($CsLaTa_2O_7$) through proton exchange and two-step intercalation. Sn was used as a single atom doped in the Ta site at 0.75%, 1.5%, 3%, and 5% doping ratios. Moreover, there was no need for additional co-catalysis to increase the amount of hydrogen production because of the added Sn at the synthesis stage, which acted as co-catalysis. The study used various techniques to analyze synthesized nanoparticles' structural and catalytic properties, including XRD, XPS, SEM, HRTEM, UV, CA, and PEIS measurements. The study also reports on the effect of single-atom Sn doping on the production of photocatalytic HER.

6.2 Experimental Procedure

The experimental part is explained in detail in chapter 2.

6.3 Result and Discussion

6.3.1 X-Ray diffraction Spectroscopy (XRD)

XRD patterns for the pure and Sn-doped $CsLaTa_2O_7$ (CLTO) layered oxides are illustrated in Figure 6.1.a. XRD analysis revealed that the synthesized samples exhibited a pattern that aligns perfectly with the reported structure in the literature [50]. The XRD diffraction patterns also found no additional peaks in samples related to the impurity phase even after Sn doped occupied Ta sites (B site) in the host perovskite layer. This observation provides good evidence for the high crystallinity of Sn-doped or undoped CLTO samples. The X-ray diffraction (XRD) pattern of the protonated structure differs from that of the unmodified version due to changes in the space group, as illustrated in Figure 6.1.b. The peak ascribed to the (001) plane at 7.95º was shifted to slightly higher angles with entering hydronium ion between the layers because the ionic radius of Cs^+ (0.176 nm) is slightly larger than that of H_3O^+ (0.100 nm) shown below Figure 6.1.b.

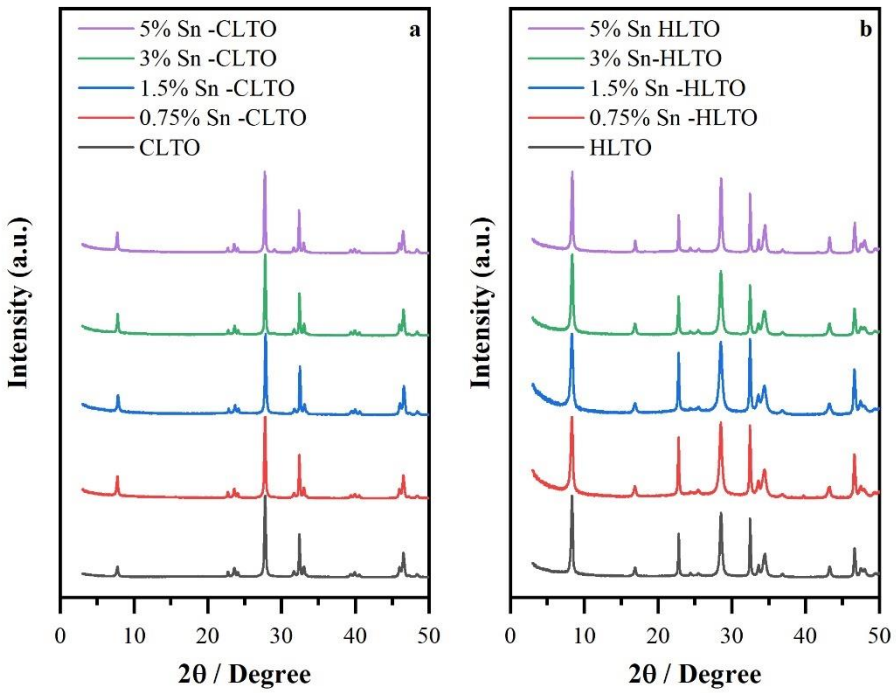

Figure 6.1 XRD pattern **(a)** $CsLaTa_2O_7$ (CLTO) and their Sn doped counterparts **(b)** $HLaTa_2O_7$ (HLTO) and their Sn doped counterparts.

6.3.2 Ultraviolet-visible (UV-vis) Diffuse Reflectance Spectroscopy

UV-vis diffuse reflectance spectra were measured in the absorbance spectrum of synthesized powders, as shown in Figure 6.2.a. The observed band edge of the pristine powder is around 300 nm. Increasing Sn loading leads to a slight red shift in the absorption edge compared to the undoped sample, suggesting a possible decrease in the band gap energy of the material with Sn doping. The band gap energy was calculated using a UV-vis spectrometer based on the relationship between the Kubelka-Munk function (F(R)) and the photon energy (hv) of the incident light. The calculated band energies of CLTO, 0.75% Sn-CLTO, 1.5% Sn-CLTO, 3% Sn-CLTO, 5% Sn-CLTO, HLTO, 0.75% Sn HLTO, 1.5% Sn HLTO, 3% Sn-HLTO, and 5% Sn HLTO can be listed as follows 4.169, 3.910, 4.121, 3.883, 3.867, 4.197, 3.883, 3.859, 3.838, and 3.834 eV, respectively. Additionally, it can be observed that protonation can affect the band gaps of catalysts in Figure 6.2.b. This effect is likely due to forming a more delocalized electron cloud within the material. The delocalized electrons can potentially cause a rearrangement of the electronic energy levels, leading to a decrease in the overall band gap energy.

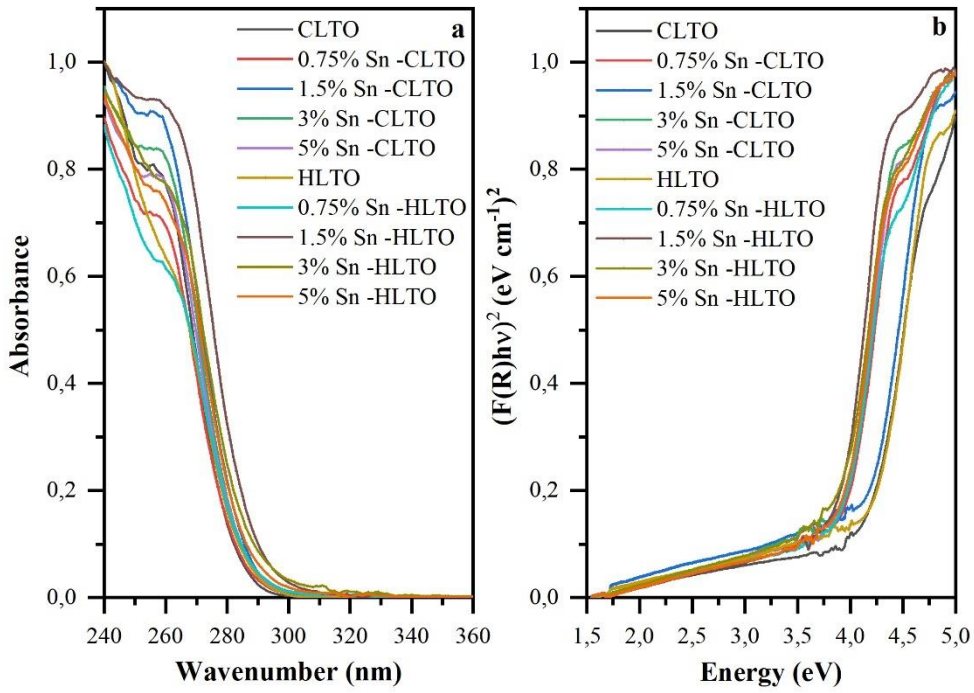

Figure 6.2 (a) UV-vis absorption spectra of pure and protonated of $CsLaTa_2O_7$ and their Sn doped counterparts, and **(b)** Transformation of diffuse reflectance data using the KM curve of pure and protonated of $CsLaTa_2O_7$ and their Sn doped counterparts.

6.3.3 X-ray Photoelectron Spectroscopy (XPS)

Deconvolution of the Ta 4f spectra in Figure 6.3.a, which separates overlapping peaks, showed a clear double peak structure. The positions of these peaks centered at 25.2 eV and 27.2 eV and corresponded to Ta $4f_{7/2}$ and Ta $4f_{5/2}$ peaks, respectively [163]. The specific positions of these peaks indicate that the Tantalum atoms in $CsLaTa_2O_7$ possess a +5-oxidation state (Ta^{5+}). XPS illustrates that the binding energies of these peaks in Figure 6.3.a gradually decrease with increasing Sn doping compared to undoped CLTO. The observed shifts in both Ta and Sn binding energies indicate a charge transfer between these elements. This charge transfer is attributed to the difference in electronegativity between Ta (1.5) and Sn (1.96) [164]. This electron transfer can modify the electronic structure of Sn-doped CLTO. The shift in the Ta 4f peak position also suggests a change in the local bonding environment around Ta. This change could be due to factors like the incorporation of Sn, potentially leading to the formation of Ta-O-Sn bonds. Figure 6.3.b. illustrates the XPS spectrum of Sn 3d, revealing two separate peaks representing Sn electrons' 3d5/2 and 3d3/2 spin-orbit components. These peaks positioned at 485.7 eV

and 494.3 eV, respectively, signify Sn existing in the +2-oxidation state [165]. XPS was employed to quantify the atomic percentage of Sn incorporated into the doped material. The analysis may have also considered the derived atomic percentage of Tantalum (Ta), assuming Sn substitutes for Ta in the material. Based on the XPS analysis, the measured Sn concentrations are as follows: 0.65%, 2.30%, 4.50%, and 8.44% from low concentration to high ones.

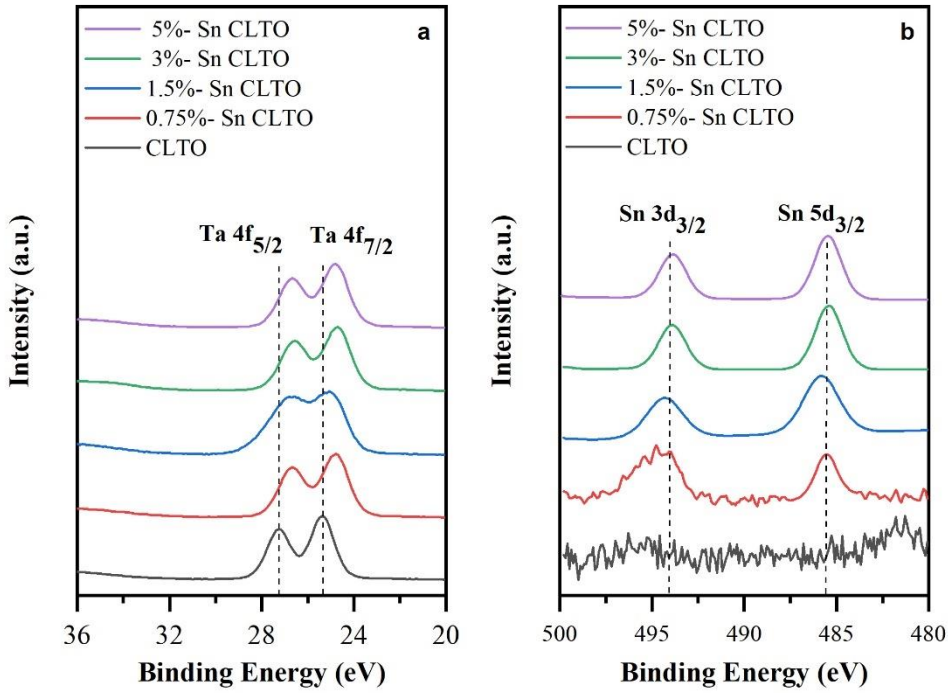

Figure 6.3 (a) XPS spectra of Ta 4f and **(b)** Sn 3d for Sn doped and undoped of $CsLaTa_2O_7$.

The band energy diagram in Figure 6.4 was constructed based on calculations that combined XPS valence band spectra and the energy band gap using UV-vis DRS. These calculations allowed for the determination of the conduction band position. Based on XPS analysis, tin in the +2-oxidation state has two more valence electrons than Tantalum in the +5 state. Sn can act as an electron donor when incorporated into the lattice, introducing additional electrons into the material. These extra electrons can occupy energy levels closer to the conduction band, effectively pushing the CBM down in energy.

The conduction band position shifted towards a more positive value for the analyzed protonated catalysts than their original versions. It is believed to be caused by protonation,

which leads to an increase in the valence band maximum (VBM) and a decrease in the band gap energy.

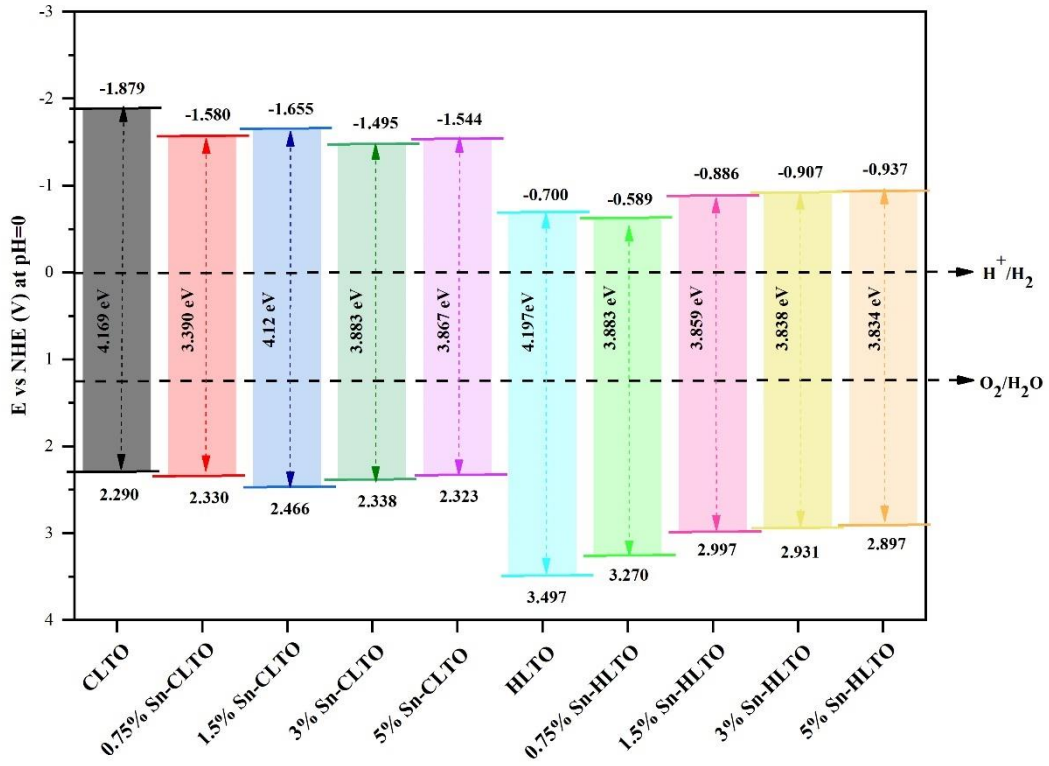

Figure 6.4 Schematic diagram of band energies pattern for Sn doped and undoped of $CsLaTa_2O_7$ and their protonated counterparts from along with Kubelka-Munk function (obtained from DRS) and Valence-Band XPS Spectra

6.3.4 Scanning Electron Microscopy (SEM)

SEM was used to investigate the surface morphology of the catalyst, using a high magnification of 100.00 K X and an acceleration voltage of 5 kV. As illustrated in Figure 6.5, the SEM analysis confirms a layered structure for all material variations. This observation is significant because it suggests that the overall morphology of the catalyst remains unchanged mainly after doping. However, a slight tendency towards accumulation was observed with a tin loading exceeding 3%. SEM analysis also revealed no metallic tin on the catalyst surface morphology, which aligns with the XPS findings,

indicating the absence of signals for metallic Sn. This result implies that tin has replaced tantalum, incorporating it into the material's structure.

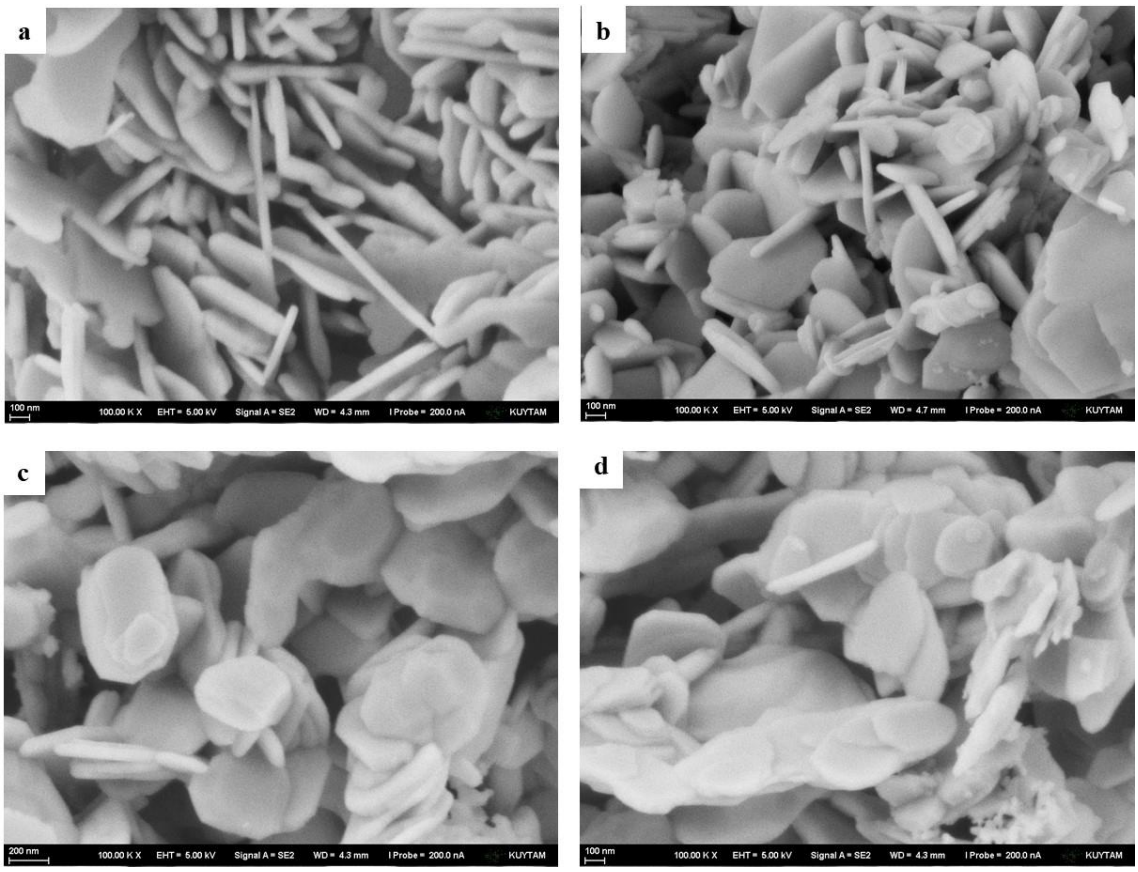

Figure 6.5 SEM images $CsLaTa_2O_7$ doped with **(a)** 0.75% Sn, **(b)** 1.5% Sn, **(c)** 3% Sn, and **(d)** 5% Sn.

6.3.5 The Brunauer-Emmett-Teller (BET) analysis

Brunauer-Emmett-Teller (BET) analysis was employed to quantify the specific surface areas of the powdered samples. As expected, the study revealed a significant increase in the surface area of the powder after exfoliation. This enhanced surface area, as shown in Table 6.1**,** can potentially accelerate catalytic surface reactions. Furthermore, the photocatalytic experiments in section 6.5 demonstrated that reassembled powders exhibited higher hydrogen production than their non-assembled counterparts.

Table 6.1 Specific surface areas of $CsLaTa_2O_7$, $[LaTa_2O_7]^-$, $[LaTa_{2-x}Sn_xO_7]^-$

Sample	Specific Surface Area / $m^2\ g^{-1}$
CLTO	1.2813
LTO	11.7917
1.5% Sn- LTO	31.8814

6.4 Results of Photoelectrochemical Experiments

6.4.1 Chronoamperometry (CA)

Transient photocurrent spectroscopy investigated photocurrent behavior dynamics under constant voltage under full spectrum illumination. Upon illumination, 2D materials generally exhibit a significant increase in photocurrent compared to bulk and protonated counterparts in Figure 6.6.

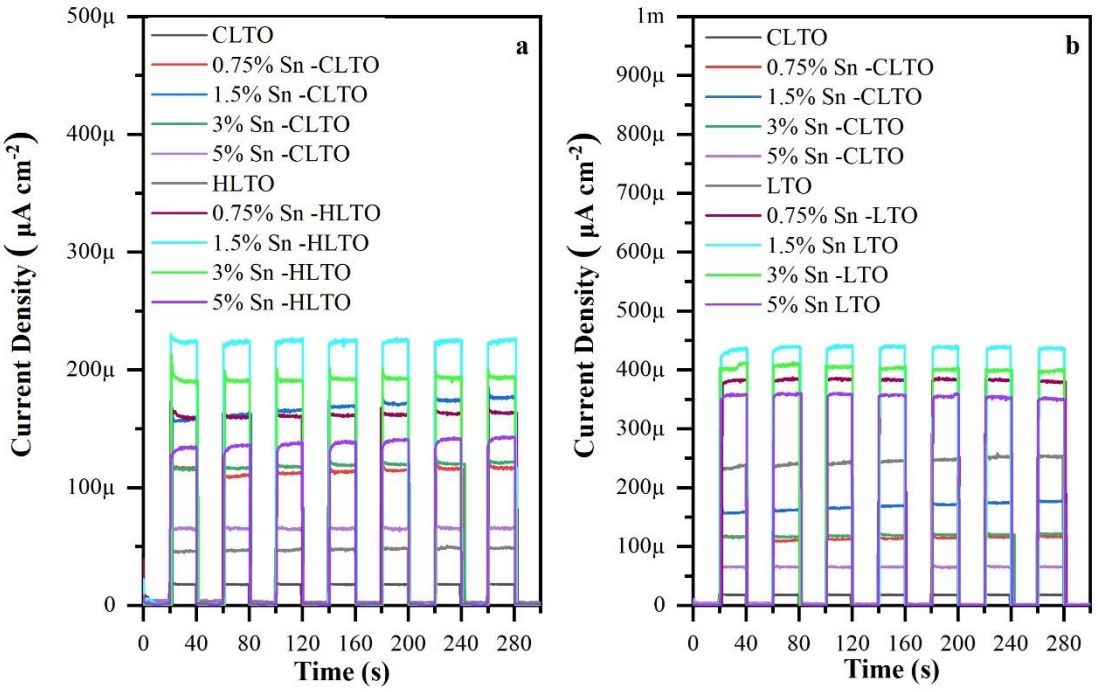

Figure 6.6 Chronoamperometry measurements of (a) original and protonated versions of both undoped and doped Sn CLTO and (b) original and exfoliated versions of both undoped, Sn CLTO at 1V vs SCE (sat'ed. KCl) under full spectrum

This enhancement can be attributed to three key factors: minimized diffusion length, high active sites, and reduced recombination losses [40]. The photocurrent density positively correlated with Sn incorporation up to a concentration of 1.5%. Beyond this point, further Sn loading resulted in a decrease in photocurrent density. This observation suggests an optimal Sn concentration of 1.5% for maximizing photocurrent generation. Moreover, the nanosheets' large surface area and potentially well-defined structure are thought to provide ideal sites for the uniform distribution of isolated Sn^{2+} dopant sites [166]. These isolated dopant sites serve two essential purposes: firstly, they can increase the carrier density within the material. Secondly, they can improve the separation of photogenerated charge carriers. It is believed that this ultimately leads to more efficient utilization of light-generated charges, enhancing the Sn-doped nanosheets' overall photoelectrochemical (PEC) performance. Notably, nanosheet structures exhibited the highest photocurrent densities (400, 485, 380, and 350 μA/cm² for increasing Sn content of 0%, 0.75%, 1.5%, and 3%, respectively) in Figure 6.7.

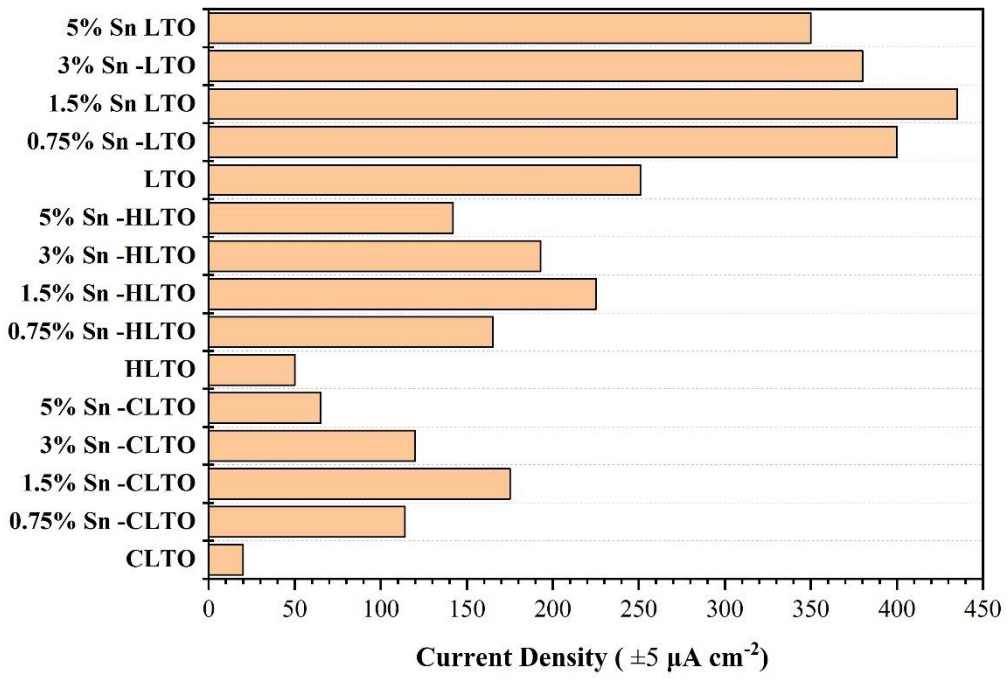

Figure 6.7 Photocurrent values of nonmodified, protonated, and exfoliated derivatives of all doped and undoped Sn.

This enhancement can be attributed to the creation of single atomic Sn sites on the nanosheet framework due to Sn doping. Figure 6.7 presents the photocurrent density for each of the synthesized powders. The data clearly demonstrates a positive effect of the structural change from bulk to nano form on charge separation efficiency.

6.4.2 Potentiostatic Electrochemical Impedance Spectroscopy (PEIS)

PEIS has analyzed the charge transfer processes at the electrode-electrolyte interface and used it to understand how Sn doped or undoped influences the PEC performance of bulk, protonated, and nanosheet forms. When the material was transformed into thin sheets (exfoliated), both undoped and doped versions showed less resistance to the flow of electrical charges compared to the original bulk material. This improvement can be seen by the smaller size of the semicircle diameter in Figure 6.8 because a smaller semicircle radius in an EIS measurement indicates a lower resistance to the flow of electrical charges within the material [167]. The reduced charge transfer resistance observed in the nanosheets is likely attributed to their high surface area and ultrathin thickness. These features result in a shorter diffusion length for charge carriers within the material. Besides that, it is believed that Sn acted as a single atomic atom behavior on nanosheet material, especially. The combined effects of increased carrier concentration and reduced scattering all contribute to decreased charge resistivity upon doping with isolated atoms. This translates to more efficient movement of photogenerated charges within the material, which is crucial for enhancing photocatalytic or photoelectrochemical performance. In summary, Nyquist EIS indicated a decrease in the diameter of the semicircle arc in the Nyquist plots with increasing Sn content (up to the optimal 1.5% concentration) in Figure 6.8. This decrease indicated a lower charge transfer resistance at the interface, supporting improved charge separation and transport.

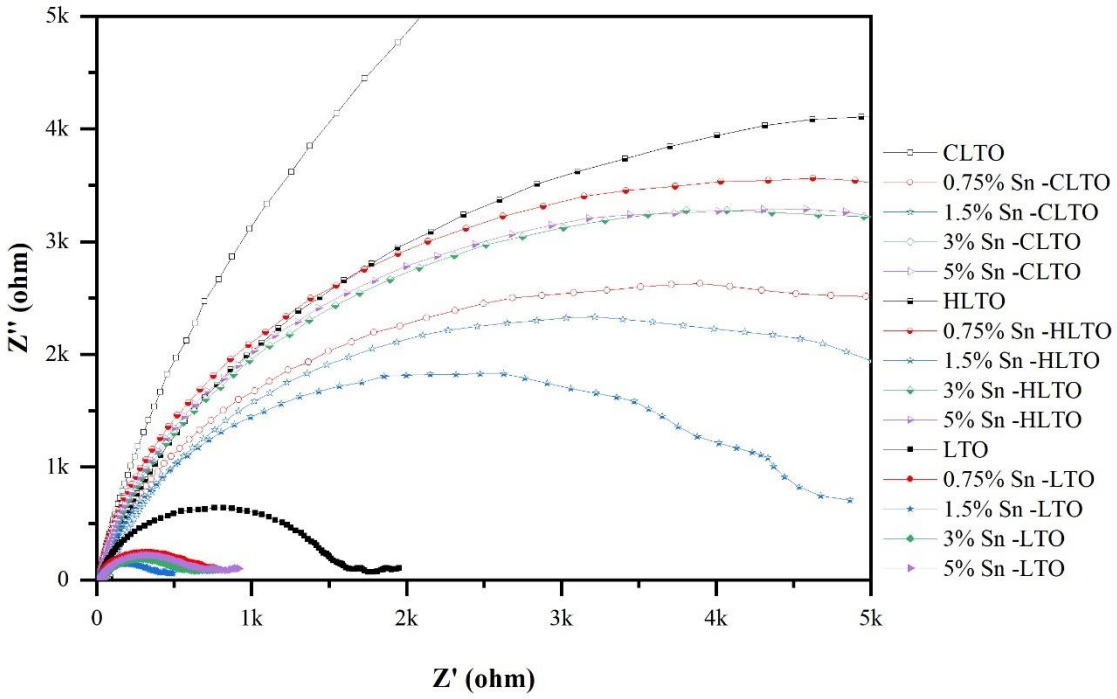

Figure 6.8 Nyquist Electrochemical impedance spectra of undoped of original phase, protonated phase, and exfoliated phase of CLTO and their Sn doped derivatives.

6.5 Photocatalytic Hydrogen Production

Figure 6.9 shows the results of photocatalytic hydrogen evolution experiments conducted under full-spectrum irradiation for 5 hours to compare the H_2 evolution activity of undoped and Sn-doped $CsLaTa_2O_7$ (CLTO) and their derivatives in DI water with 10% methanol as a hole scavenger. No co-catalysts were used. The CLTO material, in its undoped parent form, exhibited low photocatalytic HER efficiency (3.5 µmol/g). Similarly, low efficiencies were observed for the protonated (147 µmol/g) and exfoliated (500 µmol/g) derivatives compared to modified ones. However, all protonated samples exhibited a dramatically increased photocatalytic HER activity compared to their parent counterparts. This enhancement could be attributed to a higher concentration of hydronium ions (H_3O^+) and water molecules between the layers of the material. These hydronium ions can act as proton donors, facilitating the generation of H_2 from the photogenerated holes.

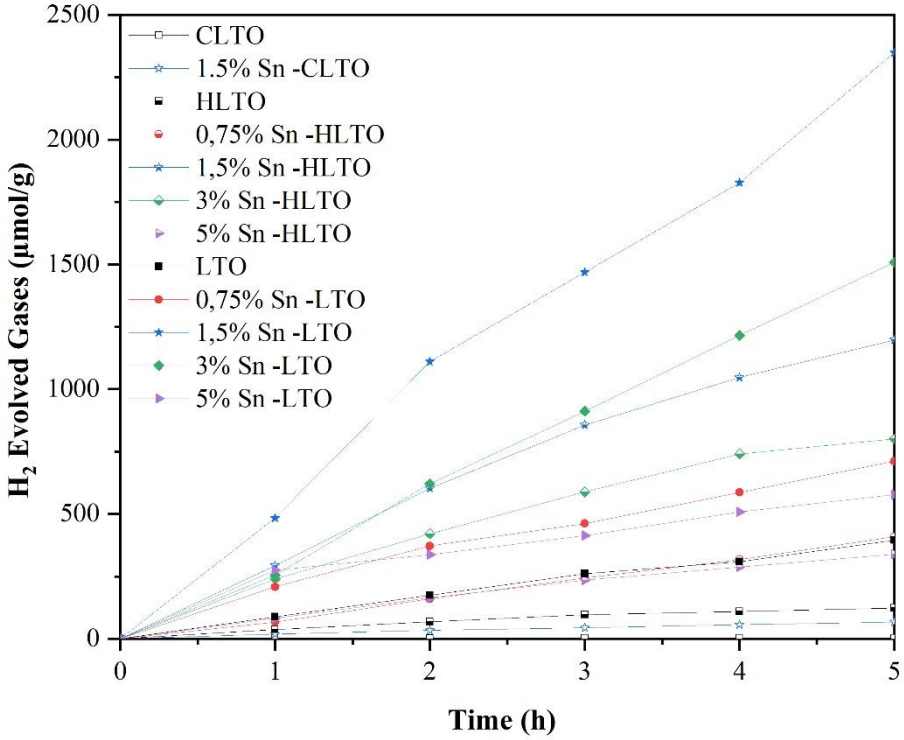

Figure 6.9 The photocatalytic hydrogen evolution activity of undoped and doped $CsLaTa_2O_7$ in the form of parent, protonated, and layered nanosheets. The experiment was conducted in a 5 ml quartz cell under full-spectrum illumination from a 300 W Xenon lamp with 10% v/v methanol as a hole scavenger without co-catalyst.

Additionally, the presence of water molecules might improve the transport of protons within the material, further promoting H_2 evolution. Moreover, all exfoliated photocatalysts indicated significantly improved H_2 production by creating a larger surface area for light absorption and interaction with water molecules, increasing active sites for efficient photocatalytic reactions, and reducing migration distance by resulting in thinner layers or smaller particles, allowing more charges to contribute to H_2 production. Furthermore, Sn intercalation as single atomic sites significantly enhanced the photocatalytic activity of these parent materials. Figure 6.10 presents the H_2 production amount (µmol/g) of all catalysis materials synthesized with or without Sn doping. The amounts of H_2 obtained from protonated photocatalyst were 123 µmol/g, 452 µmol/g, 1198 µmol/g, 800 µmol/g and 340 µmol/g for undoped and doped 0,75%, 1.5%, 3% and 5% doped Sn HLTO samples after 5 hours, respectively. The amounts of H_2 obtained

from exfoliated photocatalyst were 394 µmol/g, 712 µmol/g, 2278 µmol/g, 1508 µmol/g and 578 µmol/g for undoped and doped 0,75%, 1.5%, 3% and 5% doped Sn LTO samples after 5 hours, respectively. In light of these results, protonation with 1.5% Sn doping resulted in nearly ten times more H_2 production than the undoped parent material. Exfoliated photocatalyst with 1.5% Sn doping resulted in almost six times more H_2 production than the undoped parent material. These findings suggest that a combination of protonation, exfoliation, and optimal Sn doping levels can significantly enhance the photocatalytic HER activity of $CsLaTa_2O_7$-based materials. In conjunction with the PEC results, it can be considered that a higher photocurrent generally means a higher rate of hydrogen evolution. As a result, a higher photocurrent is thought to provide more free electrons, typically leading to a higher rate of hydrogen evolution in a PC system for HER. The relevant photocurrent and HER results are shown in **Figure 6.10**.

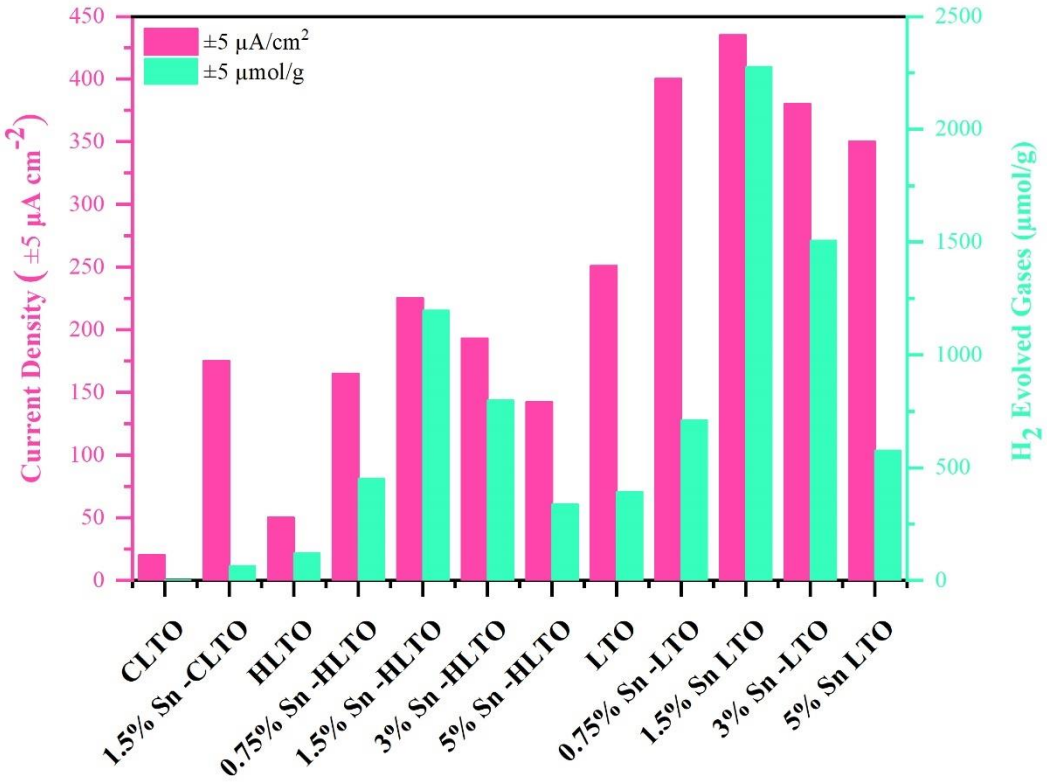

Figure 6.10 Comparison of photocatalytic hydrogen production capacity and photocurrent density in photoelectrochemical experiment.

Stability testing was employed to evaluate how well the HER performance of CLTO's bulk, protonated, and restacked powders and 1.5% Sn doped CLTO's derivatives samples (undoped, doped, protonated, etc.) are during the experiment duration of 5 hours in Figure 6.11. Also, it was given to provide insights into the material's overall durability under

reaction conditions. Stability test of photocatalytic hydrogen evolution activity for $CsLaTa_2O_7$ (CLTO) and 1.5% Sn- $CsLaTa_2O_7$ (CLTO) along with other derivations (e.g., protonated HLTO or exfoliated LTO) was conducted over three runs. Each run began with the quartz cell evacuated with Argon (Ar) to remove residual hydrogen. In summary, the photocatalyst powder maintained nearly the same level of hydrogen production even after being used for three consecutive cycles. This reusability is crucial for practical applications, as it reduces waste and lowers the long-term cost of hydrogen generation.

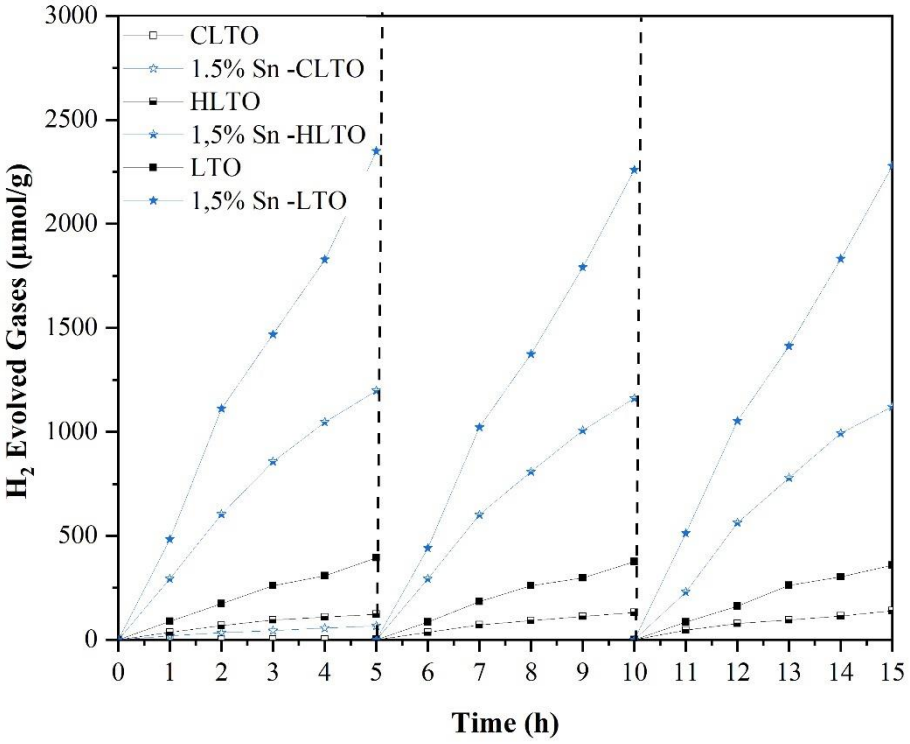

Figure 6.11 Stability test of photocatalytic hydrogen evolution for $CsLaTa_2O_7$ and 1.5% Sn- CLTO along with protonated and exfoliated counterparts.

6.6 Conclusions

This research examined how single site Sn doped two-layered tantalum perovskite oxide materials perform in the photocatalytic generation of hydrogen, explicitly focusing on their ability to do so. These materials were synthesized using the Pechini method, followed by protonation and two-step exfoliation to create the nanosheet structure.

X-ray diffraction (XRD) analysis confirmed that Sn incorporated into the tantalum sites did not cause significant structural changes. All synthesized powders subjected to tin doping show their XRD patterns closely resembling that of the standard $CsLaTa_2O_7$ (CLTO), indicating the formation of a single phase before and after the treatment.

Scanning electron microscopy (SEM) revealed that the original and protonated materials maintained a plate-like morphology. Ultraviolet-visible (UV-Vis) spectroscopy and KM plots were employed to determine the materials' optical band gap and absorbance properties. Incorporating increasing amounts of tin into the material causes a slight red shift in this absorption edge. This red shift suggests a potential decrease in the band gap energy of the material with Sn doping. It might create an additional energy level within the structure, allowing it to absorb lower-energy light.

The introduction of Sn to the structure has been proven through XPS analysis. The result illustrates that X-ray Photoelectron Spectroscopy (XPS) analysis confirmed two distinct peaks observed in the Sn 3d region at 485.7 eV and 494.3 eV, corresponding to the Sn $3d_{5/2}$ and Sn $3d_{3/2}$ spin-orbit components, respectively. These peaks confirmed the presence of Sn in the +2-oxidation state (Sn^{2+}).

The study found that powdered samples' surface areas increased after exfoliation, potentially accelerating catalytic surface reactions and demonstrating higher hydrogen production. The study further investigated the photocurrent response of the 2D materials under simulated full-spectrum light irradiation. Notably, the results revealed that a Sn concentration of 1.5% yielded the highest photocurrent generation, suggesting this material's optimal doping level. The study also found that Sn-doped improved photocatalytic or photoelectrochemical performance in bulk, protonated, and nanosheet forms.

The study analyzed the photocatalytic hydrogen evolution (HER) activity of undoped and Sn-doped CLTO and their counterparts in DI water with 10% methanol. Results showed that protonated samples increased HER activity due to higher concentrations of hydronium ions and water molecules. Exfoliated photocatalysts improved H_2 production due to high surface area, which was proved by BET analysis (approximately ten times fold in surface area), and Sn intercalation enhanced their activity. Stability testing showed consistent hydrogen production levels even after three cycles.

Among all samples, the 1.5% Sn-doped exfoliated catalyst achieved the highest hydrogen production (2500 μmol/g), nearly six times more than the undoped parent material. The 1.5% Sn CLTO, HLTO, and LTO counterparts displayed superior photoelectrochemical behavior. PEC results revealed that the protonated 1.5% Sn-doped material exhibited the highest photocurrent density and the lowest charge transfer resistance. These desirable electrochemical characteristics are believed to play a significant role in its superior performance for hydrogen production.

Moreover, the fact that 1.5% Sn-HLTO possesses the most negative conduction band potential among others in Figure 6.4 samples is another noteworthy observation. A more negative conduction band potential signifies a greater tendency for the material to donate electrons. The favorable electronic property, suitable conduction band position, and high surface area are considered critical factors for efficient hydrogen generation, as they facilitate the transfer of electrons to protons for hydrogen evolution.

Efficient hydrogen generation can be attached to three crucial factors: a supportive photoelectrochemical property, a suitable conduction band position, and a high surface area. These factors are assumed to work synergistically to facilitate the transfer of electrons from the photocatalyst to protons, ultimately enhancing the hydrogen evolution reaction.

Chapter 7: Conclusions

This research project investigated Dion-Jacobson-type tantalum-based layered oxides for their potential in photocatalytic hydrogen evolution reactions. The objective was to evaluate and identify the crucial factors influencing their performance. In addition, various material modifications to synthesized pristine catalysts were investigated to enhance their photocatalytic efficiency. Specifically, the effects of doping as a single active site and the exfoliation process for forming an atomic-scale surface were examined.

In the literature, various photocatalysis materials have been studied for photocatalytic hydrogen production. Among these materials, layered perovskite oxide has been a hot topic for over ten years because of its flexible layer, tunable electronic structure, and the probability of easy modification of crystal structure [64], [168], [169]. However, such a tantalum-based layered photocatalyst has yet to be fabricated to enhance photocatalytic performance. Herein, five different catalysts were produced, were well-designed, and characterized to generate hydrogen from water splitting.

Herein, the objective of the study in Chapter 3 was to gain insight into the conversion of $A'[A_{n-1}B_nO_{3n+1}]$ into $A'[A_{n-1}B_nO_{3n-x+1}N_x]$ and to correlate the physicochemical properties of ammonolysis powders with the resulting photocatalytic H_2 evolution activity. A close correlation was found between the nitrogen loading to the oxygen site in the lattice and high photocatalytic activity, as evidenced by the hydrogen evolution rate under AM 1.5G illumination. Notably, the formation of nanosheets from bulk counterparts led to a notable enhancement in photocatalytic activity. The triplet tantalum-based oxynitride perovskite exhibited an increase from 0.2 µmol/g to 6 µmol/g from bulk to nanosheet structure, and the doublet tantalum-based oxynitride perovskite showed a rise from 1 µmol/g to a remarkable 20 µmol/g from bulk to nanosheet structure.

Chapter 4 investigated the synthesis and photocatalytic performance of $CsCa_2Ta_3O_{10}$ materials doped with palladium at concentrations of 1.5%, 3%, and 5%. Following synthesis, these materials underwent protonation treatment to enhance their photocatalytic activity for the hydrogen evolution reaction. This enhancement is likely due to the formation of a hydrated interlayer structure. Notably, the nanosheet counterparts exhibited a significant increase in hydrogen evolution compared to their bulk and non-protonated counterparts. This improvement can be attributed to the nanosheets'

higher surface area and atomic-scale thickness. It is known that nanosheets serve as an ideal platform for the uniform distribution of single atomic palladium sites. Based on these structural, optical, morphological characterization, and photoelectrochemical analysis results, it is believed that the isolated Pd sites dispersed uniformly across the nanosheet structure function as efficient catalytic centers, leading to the observed enhancement in HER performance. In particular, the 1.5% Pd-doped nanosheets exhibited considerable enhancements in hydrogen evolution, superior photoelectrochemical performance, and a more negative conduction band maximum compared to other samples.

The synthesis and photocatalytic performance of $CsLaTa_2O_7$ materials was examined in different Pd loading (1.5%, 3%, and 5%) in Chapter 5 and various Sn loading (0.75%, 1.5%, 3%, and 5%) in Chapter 6. The protonation and exfoliation processes were applied to increase their photocatalytic activity. Based on photocatalytic outcomes in Chapter 5, pristine bulk, protonated, and exfoliated catalysts produced 4 (µmol/g), 123 (µmol/g), and 394 (µmol/g) hydrogen gas, respectively. Remarkably, Pd-doped exfoliated samples $[LaTa_2O_7]^-$ exhibited better photocatalytic performance (3750 µmol/g for 1.5%, 2250 µmol/g for %3, and 1750 µmol/g for %5). The material also presented superior photoelectrochemical properties as a consequence of a shorter diffusion distance, a high surge area, a low charge transfer resistance, and high photocurrent stability under pulse illumination. Chapter 6 explores tin-doped exfoliated catalysts, demonstrating their remarkable hydrogen production capacity and competing with palladium (Pd). This is a significant finding, considering the cost-effectiveness of tin compared to Pd. Based on this efficiency-cost relationship, tin-doped materials are strong candidates for ideal photocatalysts. The doped and undoped derivatives of the electronic band structures of all pure and protonated samples synthesized in this thesis are summarized in Table 7.1.

Table 7.1 Band energies diagram of all the synthesized powder

Samples	**VBM vs. NHE**	**CBM vs. NHE**	**E_g, vs. eV**
CCTO	2.657	-1.756	4.42
HCTO	3.163	-1.213	4.39
CCTOx	1.868	-0.190	2.08
HCTOx	1.229	-0.839	2.08
1.5% Pd-CCTO	2.714	-1.663	4.377

3% Pd-CCTO	2.636	-1.815	4.351
5% Pd-CCTO	2.577	-1.821	4.398
1.5% Pd-HCTO	2.914	-1.472	4.386
3% Pd-HCTO	3.239	-1.145	4.384
5% Pd-HCTO	3.240	-1.142	4.382
CLTO	2.496	-1.679	4.15
HLTO	3.497	-0.700	4.17
CLTOx	1.740	-0.205	2.01
HLTOx	1.614	-0.386	2.04
1.5% Pd-CLTO	2.496	-1.653	4.377
3% Pd-CLTO	2.608	-1.574	4.451
5% Pd-CLTO	2.422	-1.765	4.398
1.5% Pd-HLTO	2.932	-1.135	4.386
3% Pd-HLTO	3.930	-1.142	4.384
5% Pd-HLTO	3.238	-0.762	4.382
0.75% Sn-CLTO	2.330	-1.580	3.390
1.5% Sn-CLTO	2.466	-1.655	4.120
3% Sn-CLTO	2.338	-1.495	3.883
5% Sn-CLTO	2.323	-1.544	3.867
0.75% Sn-HLTO	3.270	-0.589	3.883
1.5% Sn-HLTO	2.997	-0.886	3.859
3% Sn-HLTO	2.931	-0.907	3.838
5% Sn-HLTO	2.897	-0.937	3.834

The Table 7.1 indicates that the CBM of all synthesized materials was suitable for hydrogen evolution. Furthermore, in oxide nitride materials, band energies were lower than 3 eV, suggesting that they are effective catalysts in the visible regions. It has been demonstrated that these materials are actively working.

Further research can focus on optimizing these materials through modifications to achieve even higher performance. Future research could investigate the potential of these materials in broader photocatalytic applications. This could involve testing them with various two-metal dopants to assess their performance in CO_2 reduction alongside

hydrogen evolution. Additionally, exploring more cost-effective metal doping strategies, mainly focusing on single-atom dopants like tin used in this study, presents a promising avenue for future research.

Bibliography

[1] Y. Okamoto, S. Ida, J. Hyodo, H. Hagiwara, and T. Ishihara, 'Supporting Information Synthesis and Photocatalytic Activity of Rhodium-Doped Calcium Niobate Nanosheets for Hydrogen Production from a Water/Methanol System without Cocatalyst Loading'.

[2] REN21, 'RENEWABLES 2020 GLOBAL STATUS REPORT'. Accessed: Mar. 04, 2024. [Online]. Available: https://www.ren21.net/gsr-2020

[3] S. Yu, J. Liu, X. Hu, and P. Tian, 'Does development of renewable energy reduce energy intensity? Evidence from 82 countries', *Technological Forecasting and Social Change*, vol. 174, p. 121254, Jan. 2022, doi: 10.1016/j.techfore.2021.121254.

[4] R. Marschall and L. Wang, 'Non-metal doping of transition metal oxides for visible-light photocatalysis', *Catalysis Today*, vol. 225, pp. 111–135, Apr. 2014, doi: 10.1016/j.cattod.2013.10.088.

[5] H. Song, S. Luo, H. Huang, B. Deng, and J. Ye, 'Solar-Driven Hydrogen Production: Recent Advances, Challenges, and Future Perspectives', *ACS Energy Lett.*, vol. 7, no. 3, pp. 1043–1065, Mar. 2022, doi: 10.1021/acsenergylett.1c02591.

[6] X. Zheng *et al.*, 'Recent advances in photocatalytic hydrogen evolution of AgIn5S8-based photocatalysts', *Interdisciplinary Materials*, vol. 2, no. 5, pp. 669–688, 2023, doi: 10.1002/idm2.12120.

[7] Y. Hu *et al.*, 'Layered perovskite oxides and their derivative nanosheets adopting different modification strategies towards better photocatalytic performance of water splitting', *Renewable and Sustainable Energy Reviews*, vol. 119, p. 109527, Mar. 2020, doi: 10.1016/j.rser.2019.109527.

[8] E. Kalamaras, M. M. Maroto-Valer, M. Shao, J. Xuan, and H. Wang, 'Solar carbon fuel via photoelectrochemistry', *Catalysis Today*, vol. 317, pp. 56–75, Nov. 2018, doi: 10.1016/j.cattod.2018.02.045.

[9] 'Understanding the Nernst Equation and Other Electrochemical Concepts: An Easy Experimental Approach for Students | Journal of Chemical Education'. Accessed: Apr. 20, 2024. [Online]. Available: https://pubs.acs.org/doi/10.1021/ed2007179

[10] K. Maeda, 'Photocatalytic water splitting using semiconductor particles: History and recent developments', *Journal of Photochemistry and Photobiology C: Photochemistry Reviews*, vol. 12, no. 4, pp. 237–268, Dec. 2011, doi: 10.1016/j.jphotochemrev.2011.07.001.

[11] R. Marschall, '50 Years of Materials Research for Photocatalytic Water Splitting', *European Journal of Inorganic Chemistry*, vol. 2021, no. 25, pp. 2435–2441, 2021, doi: 10.1002/ejic.202100264.

[12] H. Zhang, J. Liu, T. Xu, W. Ji, and X. Zong, 'Recent Advances on Small Band Gap Semiconductor Materials (≤2.1 eV) for Solar Water Splitting', *Catalysts*, vol. 13, no. 4, Art. no. 4, Apr. 2023, doi: 10.3390/catal13040728.

[13] J. Ma, J. Fu, L. Sun, J. Cheng, and J.-F. Li, 'Photoelectrochemical-driven nitrogen reduction to ammonia by a V o -SnO_2 /TiO_2 composite electrode', *Nanoscale*, 2024, doi: 10.1039/D4NR00060A.

[14] I. R. Hamdani and A. N. Bhaskarwar, 'Recent progress in material selection and device designs for photoelectrochemical water-splitting', *Renewable and Sustainable Energy Reviews*, vol. 138, p. 110503, Mar. 2021, doi: 10.1016/j.rser.2020.110503.

[15] 'Photo-electrochemical hydrogen generation from water using solar energy. Materials-related aspects - ScienceDirect'. Accessed: Mar. 04, 2024. [Online]. Available: https://www.sciencedirect.com/science/article/pii/S0360319902000228

[16] W. Yang *et al.*, 'Ferroelectric Polarization-Enhanced Photoelectrochemical Water Splitting in TiO_2–$BaTiO_3$ Core–Shell Nanowire Photoanodes', *Nano Lett.*, vol. 15, no. 11, pp. 7574–7580, Nov. 2015, doi: 10.1021/acs.nanolett.5b03988.

[17] C. Avcıoğlu, S. Avcıoğlu, M. F. Bekheet, and A. Gurlo, 'Photocatalytic Overall Water Splitting by $SrTiO_3$: Progress Report and Design Strategies', *ACS Appl. Energy Mater.*, vol. 6, no. 3, pp. 1134–1154, Feb. 2023, doi: 10.1021/acsaem.2c03280.

[18] Y. Fan *et al.*, 'Photocatalytic Overall Water Splitting by $SrTiO_3$ with Surface Oxygen Vacancies', *Nanomaterials (Basel)*, vol. 10, no. 12, p. 2572, Dec. 2020, doi: 10.3390/nano10122572.

[19] F. T. Wagner and G. A. Somorjai, 'Photocatalytic hydrogen production from water on Pt-free $SrTiO_3$ in alkali hydroxide solutions', *Nature*, vol. 285, no. 5766, pp. 559–560, Jun. 1980, doi: 10.1038/285559a0.

[20] 'Structure Characterization and Tuning of Perovskite-Like $NaTaO_3$ for Applications in Photoluminescence and Photocatalysis - Hu - 2009 - Journal of the American Ceramic Society - Wiley Online Library'. Accessed: Mar. 04, 2024. [Online]. Available: https://ceramics.onlinelibrary.wiley.com/doi/full/10.1111/j.1551-2916.2008.02869.x

[21] H. Hayashi, Y. Hakuta, and Y. Kurata, 'Hydrothermal synthesis of potassium niobate photocatalysts under subcritical and supercritical water conditions', *Journal of Materials Chemistry*, vol. 14, no. 13, p. 2046, 2004, doi: 10.1039/b400130n.

[22] G. Li, Z. Yi, Y. Bai, W. Zhang, and H. Zhang, 'Anisotropy in photocatalytic oxidization activity of $NaNbO_3$ photocatalyst', *Dalton Transactions*, vol. 41, no. 34, p. 10194, 2012, doi: 10.1039/c2dt30593c.

[23] L. Yang *et al.*, 'Ferroelectric spontaneous polarization assisted TiO_2@$BaTiO_3$@Ag photoanode for efficient photoelectrochemical water splitting via BaTiO3 phase regulation', *International Journal of Hydrogen Energy*, vol. 55, pp. 997–1006, Feb. 2024, doi: 10.1016/j.ijhydene.2023.12.132.

[24] K. C. Christoforidis and P. Fornasiero, 'Photocatalytic Hydrogen Production: A Rift into the Future Energy Supply', *ChemCatChem*, vol. 9, no. 9, pp. 1523–1544, 2017, doi: 10.1002/cctc.201601659.

[25] C. J. Fu, Q. Ma, L. Gao, and S. Li, 'Recent Advances in Perovskite Oxides Electrocatalysts: Ordered Perovskites, Cations Segregation and Exsolution', *ChemCatChem*, vol. 15, no. 11, p. e202300389, 2023, doi: 10.1002/cctc.202300389.

[26] T. Ishihara, 'Inorganic Perovskite Oxides', in *Springer Handbook of Electronic and Photonic Materials*, S. Kasap and P. Capper, Eds., in Springer Handbooks. , Cham: Springer International Publishing, 2017, pp. 1–1. doi: 10.1007/978-3-319-48933-9_59.

[27] J. Zhu *et al.*, 'Perovskite Oxides: Preparation, Characterizations, and Applications in Heterogeneous Catalysis', *ACS Catal.*, vol. 4, no. 9, pp. 2917–2940, Sep. 2014, doi: 10.1021/cs500606g.

[28] L. Lyu, S. Cho, and Y.-M. Kang, 'Recent advances in perovskite oxide electrocatalysts for Li–O2 batteries', *EES. Catal.*, vol. 1, no. 3, pp. 230–249, May 2023, doi: 10.1039/D3EY00028A.

[29] I. R. de Larramendi *et al.*, 'Designing Perovskite Oxides for Solid Oxide Fuel Cells', in *Perovskite Materials - Synthesis, Characterisation, Properties, and Applications*, IntechOpen, 2016. doi: 10.5772/61304.

[30] Y. Pan *et al.*, 'Direct evidence of boosted oxygen evolution over perovskite by enhanced lattice oxygen participation', *Nat Commun*, vol. 11, no. 1, p. 2002, Apr. 2020, doi: 10.1038/s41467-020-15873-x.

[31] J. Suntivich, K. J. May, H. A. Gasteiger, J. B. Goodenough, and Y. Shao-Horn, 'A Perovskite Oxide Optimized for Oxygen Evolution Catalysis from Molecular Orbital Principles', *Science*, vol. 334, no. 6061, pp. 1383–1385, Dec. 2011, doi: 10.1126/science.1212858.

[32] 'Functional Role of Fe-Doping in Co-Based Perovskite Oxide Catalysts for Oxygen Evolution Reaction | Journal of the American Chemical Society'. Accessed: Mar. 09, 2024. [Online]. Available: https://pubs.acs.org/doi/10.1021/jacs.8b12101

[33] 'Perovskite Oxides as Electrocatalysts for Hydrogen Evolution Reaction | ACS Omega'. Accessed: Mar. 09, 2024. [Online]. Available: https://pubs.acs.org/doi/10.1021/acsomega.1c07203

[34] J. Dai *et al.*, 'Single-phase perovskite oxide with super-exchange induced atomic-scale synergistic active centers enables ultrafast hydrogen evolution', *Nat Commun*, vol. 11, no. 1, p. 5657, Nov. 2020, doi: 10.1038/s41467-020-19433-1.

[35] V.-H. Nguyen *et al.*, 'Perovskite oxide-based photocatalysts for solar-driven hydrogen production: Progress and perspectives', *Solar Energy*, vol. 211, pp. 584–599, Nov. 2020, doi: 10.1016/j.solener.2020.09.078.

[36] K. Kawashima, M. Hojamberdiev, H. Wagata, K. Yubuta, K. Domen, and K. Teshima, 'Protonated Oxide, Nitrided, and Reoxidized $K_2La_2Ti_3O_{10}$ Crystals: Visible-Light-Induced Photocatalytic Water Oxidation and Fabrication of Their Nanosheets', *ACS Sustainable Chem. Eng.*, vol. 5, no. 1, pp. 232–240, Jan. 2017, doi: 10.1021/acssuschemeng.6b01344.

[37] K. Kawashima *et al.*, 'Understanding the effect of partial N_3^--to-O_2^- substitution and H^+-to-K^+ exchange on photocatalytic water reduction activity of Ruddlesden–Popper layered perovskite $KLaTiO_4$', *Molecular Catalysis*, vol. 432, pp. 250–258, May 2017, doi: 10.1016/j.mcat.2017.01.004.

[38] D. Arney, L. Fuoco, J. Boltersdorf, and P. A. Maggard, 'Flux Synthesis of $Na_2Ca_2Nb_4O_{13}$: The Influence of Particle Shapes, Surface Features, and Surface Areas on Photocatalytic Hydrogen Production', *Journal of the American Ceramic Society*, vol. 96, no. 4, pp. 1158–1162, 2013, doi: 10.1111/jace.12122.

[39] S. NISHIMOTO, Y. OKAZAKI, M. MATSUDA, and M. MIYAKE, 'Photocatalytic H_2 evolution by layered perovskite $Ca_3Ti_2O_7$ codoped with Rh and Ln (Ln = La, Pr, Nd, Eu, Gd, Yb, and Y) under visible light irradiation', *Journal of the Ceramic Society of Japan*, vol. 117, no. 1371, pp. 1175–1179, 2009, doi: 10.2109/jcersj2.117.1175.

[40] M. Khodabakhsh, B. Yilmaz, S. Firoozi, D. Fatmehsari Haghshenas, and U. Unal, 'Enhanced Photocatalytic Properties of Restacked Unilamellar $[SrTa_2O_7]^{2-}$ Nanosheets of Aurivillius Phase Layered Perovskites', *ACS Omega*, vol. 8, no. 11, pp. 10607–10617, Mar. 2023, doi: 10.1021/acsomega.3c00593.

[41] Y. Li, G. Chen, C. Zhou, and Z. Li, 'Photocatalytic Water Splitting Over a Protonated Layered Perovskite Tantalate $H_{1.81}Sr_{0.81}Bi_{0.19}Ta_2O_7$', *Catal Lett*, vol. 123, no. 1, pp. 80–83, Jun. 2008, doi: 10.1007/s10562-008-9397-5.

[42] W. Chen *et al.*, 'Photocatalytic water splitting on protonated form of layered perovskites $K_{0.5}La_{0.5}Bi_2M_2O_9$ (M = Ta; Nb) by ion-exchange', *International Journal of Hydrogen Energy*, vol. 37, no. 17, pp. 12846–12851, Sep. 2012, doi: 10.1016/j.ijhydene.2012.05.090.

[43] H. Jeong, T. Kim, D. Kim, and K. Kim, 'Hydrogen production by the photocatalytic overall water splitting on $NiO/Sr_3Ti_2O_7$, *International Journal of Hydrogen Energy*, vol. 31, no. 9, pp. 1142–1146, Aug. 2006, doi: 10.1016/j.ijhydene.2005.10.005.

[44] H. G. Kim, D. W. Hwang, and J. S. Lee, 'An Undoped, Single-Phase Oxide Photocatalyst Working under Visible Light', *Journal of the American Chemical Society*, vol. 126, no. 29, pp. 8912–8913, Jul. 2004, doi: 10.1021/ja049676a.

[45] T. Oshima, Y. Wang, D. Lu, T. Yokoi, and K. Maeda, 'Photocatalytic overall water splitting on Pt nanocluster-intercalated, restacked $KCa_2Nb_3O_{10}$ nanosheets: the promotional effect of co-existing ions', *Nanoscale Adv.*, vol. 1, no. 1, pp. 189–194, Jan. 2019, doi: 10.1039/C8NA00240A.

[46] Y. Huang, Y. Wei, L. Fan, M. Huang, J. Lin, and J. Wu, 'Photocatalytic activities of $HLaNb_2O_7$ prepared by polymerized complex method', *International Journal of Hydrogen Energy*, vol. 34, no. 13, pp. 5318–5325, 2009, doi: 10.1016/j.ijhydene.2009.04.040.

[47] J. Boltersdorf and P. A. Maggard, 'Silver Exchange of Layered Metal Oxides and Their Photocatalytic Activities', *ACS Catal.*, vol. 3, no. 11, pp. 2547–2555, Nov. 2013, doi: 10.1021/cs400466b.

[48] K. Maeda and M. Eguchi, 'Structural effects of two-dimensional perovskite $Ca_2Nb_2TaO_{10}^-$ nanosheets for photocatalytic hydrogen evolution', *Catal. Sci. Technol.*, vol. 6, no. 4, pp. 1064–1069, Feb. 2016, doi: 10.1039/C5CY01246E.

[49] S. Ida, Y. Okamoto, M. Matsuka, H. Hagiwara, and T. Ishihara, 'Preparation of Tantalum-Based Oxynitride Nanosheets by Exfoliation of a Layered Oxynitride, $CsCa_2Ta_3O_{10-x}N_y$, and Their Photocatalytic Activity', *J. Am. Chem. Soc.*, vol. 134, no. 38, pp. 15773–15782, Sep. 2012, doi: 10.1021/ja3043678.

[50] M. Lv, X. Sun, S. Wei, C. Shen, Y. Mi, and X. Xu, 'Ultrathin Lanthanum Tantalate Perovskite Nanosheets Modified by Nitrogen Doping for Efficient Photocatalytic Water Splitting', *ACS Nano*, vol. 11, no. 11, pp. 11441–11448, Nov. 2017, doi: 10.1021/acsnano.7b06131.

[51] M. Machida, J. Yabunaka, and T. Kijima, 'Efficient photocatalytic decomposition of water with the novel layered tantalate $RbNdTa_2O_7$', *Chem. Commun.*, no. 19, pp. 1939–1940, Jan. 1999, doi: 10.1039/A905246A.

[52] G. Zhang, G. Liu, L. Wang, and J. T. S. Irvine, 'Inorganic perovskite photocatalysts for solar energy utilization', *Chem. Soc. Rev.*, vol. 45, no. 21, pp. 5951–5984, Oct. 2016, doi: 10.1039/C5CS00769K.

[53] S. Akbarian-Tefaghi, 'Microwave-Assisted Topochemical Manipulation of Layered Oxide Perovskites: From Inorganic Layered Oxides to Inorganic-Organic Hybrid Perovskites and Functionalized Metal-Oxide Nanosheets', 2017. Accessed: Mar. 09, 2024. [Online]. Available: https://www.semanticscholar.org/paper/Microwave-Assisted-Topochemical-Manipulation-of-to-Akbarian-Tefaghi/17a27197dc1eb643daf156fc6aca6d737fe216b1

[54] L. Gustin, 'Synthesis and Topochemical Manipulation of New Layered Perovskites'.
[55] N. Shioda, J.-M. Heo, B. Kim, H. Imai, J.-M. Kim, and Y. Oaki, 'Layered macrocycles with flexibility and tunable dynamic properties for wide-range thermoresponsive color changes', *Sensors & Diagnostics*, vol. 1, no. 1, pp. 160–168, 2022, doi: 10.1039/D1SD00024A.
[56] P. F. Satterthwaite *et al.*, 'Van der Waals device integration beyond the limits of van der Waals forces using adhesive matrix transfer', *Nat Electron*, vol. 7, no. 1, pp. 17–28, Jan. 2024, doi: 10.1038/s41928-023-01079-8.
[57] D. Gerchman and A. K. Alves, 'Solution-processable exfoliation and suspension of atomically thin WSe_2', *Journal of Colloid and Interface Science*, vol. 468, pp. 247–252, Apr. 2016, doi: 10.1016/j.jcis.2016.01.073.
[58] B. S. Kwak, J. Y. Do, N.-K. Park, and M. Kang, 'Surface modification of layered perovskite Sr_2TiO_4 for improved CO_2 photoreduction with H_2O to CH_4', *Sci Rep*, vol. 7, no. 1, p. 16370, Nov. 2017, doi: 10.1038/s41598-017-16605-w.
[59] H. Li *et al.*, 'Strategies for improving the stability of perovskite for photocatalysis: A review of recent progress', *Chemosphere*, vol. 344, p. 140395, Dec. 2023, doi: 10.1016/j.chemosphere.2023.140395.
[60] Y. Hu *et al.*, 'Layered perovskite oxides and their derivative nanosheets adopting different modification strategies towards better photocatalytic performance of water splitting', *Renewable and Sustainable Energy Reviews*, vol. 119, Mar. 2020, doi: 10.1016/j.rser.2019.109527.
[61] C. Dong *et al.*, 'Size-dependent activity and selectivity of carbon dioxide photocatalytic reduction over platinum nanoparticles', *Nat Commun*, vol. 9, no. 1, p. 1252, Mar. 2018, doi: 10.1038/s41467-018-03666-2.
[62] H. Suzuki, O. Tomita, M. Higashi, and R. Abe, 'Design of nitrogen-doped layered tantalates for non-sacrificial and selective hydrogen evolution from water under visible light', *Journal of Materials Chemistry A*, vol. 4, no. 37, pp. 14444–14452, 2016, doi: 10.1039/c6ta04416f.
[63] Y. Huang, J. Li, Y. Wei, Y. Li, J. Lin, and J. Wu, 'Fabrication and photocatalytic property of Pt-intercalated layered perovskite niobates $H_{1-x}LaNb_{2-x}Mo_xO_7$ (x = 0–0.15)', *Journal of Hazardous Materials*, vol. 166, no. 1, pp. 103–108, Jul. 2009, doi: 10.1016/j.jhazmat.2008.11.040.
[64] Y. Hu *et al.*, 'Layered perovskite oxides and their derivative nanosheets adopting different modification strategies towards better photocatalytic performance of water splitting', *Renewable and Sustainable Energy Reviews*, vol. 119, p. 109527, Mar. 2020, doi: 10.1016/J.RSER.2019.109527.
[65] K. Shimizu, S. Itoh, T. Hatamachi, T. Kodama, M. Sato, and K. Toda, 'Photocatalytic Water Splitting on Ni-Intercalated Ruddlesden−Popper Tantalate $H_2La_{2/3}Ta_2O_7$', *Chem. Mater.*, vol. 17, no. 20, pp. 5161–5166, Oct. 2005, doi: 10.1021/cm050982c.
[66] J. Yang, D. Wang, H. Han, and C. Li, 'Roles of cocatalysts in photocatalysis and photoelectrocatalysis', *Acc Chem Res*, vol. 46, no. 8, pp. 1900–1909, Aug. 2013, doi: 10.1021/ar300227e.
[67] H. He, H. H. Wang, J. Liu, X. Liu, W. Li, and Y. Wang, 'Research Progress and Application of Single-Atom Catalysts: A Review', *Molecules*, vol. 26, no. 21, p. 6501, Oct. 2021, doi: 10.3390/molecules26216501.
[68] 'A new approach creates an exceptional single-atom catalyst for water splitting', SLAC National Accelerator Laboratory. Accessed: Mar. 10, 2024. [Online].

Available: https://www6.slac.stanford.edu/news/2021-08-31-new-approach-creates-exceptional-single-atom-catalyst-water-splitting

[69] X. Li *et al.*, 'Single-Atom Pt as Co-Catalyst for Enhanced Photocatalytic H2 Evolution', *Advanced Materials*, vol. 28, no. 12, pp. 2427–2431, 2016, doi: 10.1002/adma.201505281.

[70] L. Liu and A. Corma, 'Metal Catalysts for Heterogeneous Catalysis: From Single Atoms to Nanoclusters and Nanoparticles', *Chem. Rev.*, vol. 118, no. 10, pp. 4981–5079, May 2018, doi: 10.1021/acs.chemrev.7b00776.

[71] X. Yao *et al.*, 'Intrinsic and external active sites of single-atom catalysts', *iScience*, vol. 26, no. 7, p. 107275, Jul. 2023, doi: 10.1016/j.isci.2023.107275.

[72] M. Abbas and M. A. Z. G. Sial, 'New Horizon in stabilization of single atoms on metal-oxide supports for CO_2 reduction', *Nano Materials Science*, vol. 3, no. 4, pp. 368–389, Dec. 2021, doi: 10.1016/j.nanoms.2021.07.009.

[73] P. Zhai *et al.*, 'Engineering single-atomic ruthenium catalytic sites on defective nickel-iron layered double hydroxide for overall water splitting', *Nat Commun*, vol. 12, no. 1, p. 4587, Jul. 2021, doi: 10.1038/s41467-021-24828-9.

[74] Q. Zuo *et al.*, 'Ultrathin Metal–Organic Framework Nanosheets with Ultrahigh Loading of Single Pt Atoms for Efficient Visible-Light-Driven Photocatalytic H_2 Evolution', *Angewandte Chemie International Edition*, vol. 58, no. 30, pp. 10198–10203, 2019, doi: 10.1002/anie.201904058.

[75] X. Zheng *et al.*, 'Origin of enhanced water oxidation activity in an iridium single atom anchored on NiFe oxyhydroxide catalyst', *Proceedings of the National Academy of Sciences*, vol. 118, no. 36, p. e2101817118, Sep. 2021, doi: 10.1073/pnas.2101817118.

[76] M. Sun, T. Wu, and B. Huang, 'Designing the future atomic electrocatalyst for efficient energy systems', *Engineering Reports*, vol. 2, no. 12, p. e12327, 2020, doi: 10.1002/eng2.12327.

[77] X. Li, X. Kuang, and J. Sun, 'Rare earth elements based oxide ion conductors', *Inorg. Chem. Front.*, vol. 8, no. 5, pp. 1374–1398, Mar. 2021, doi: 10.1039/D0QI00848F.

[78] M. J. Geselbracht *et al.*, 'New solid acids in the triple-layer Dion–Jacobson layered perovskite family', *Materials Research Bulletin*, vol. 46, no. 3, pp. 398–406, Mar. 2011, doi: 10.1016/j.materresbull.2010.12.007.

[79] Y. Sun, G. Zhang, Y. Xu, and R. Zhang, 'Catalytic performance of dioxide reforming of methane over Co/AC-N catalysts: Effect of nitrogen doping content and calcination temperature', *International Journal of Hydrogen Energy*, vol. 44, no. 31, pp. 16424–16435, Jun. 2019, doi: 10.1016/j.ijhydene.2019.04.250.

[80] M. Chiesa, S. Livraghi, M. Cristina Paganini, E. Salvadori, and E. Giamello, 'Nitrogen-doped semiconducting oxides. Implications on photochemical, photocatalytic and electronic properties derived from EPR spectroscopy', *Chemical Science*, vol. 11, no. 26, pp. 6623–6641, 2020, doi: 10.1039/D0SC02876B.

[81] N. Kulischow, M. Ade, M. Weiss, and R. Marschall, 'Nitrogen-doped, proton-exchanged Dion-Jacobson layered niobate perovskites for photocatalytic hydrogen generation in solar light', *Photochem Photobiol Sci*, vol. 21, no. 11, pp. 1991–2000, Nov. 2022, doi: 10.1007/s43630-022-00273-5.

[82] J. J. Brown, Z. Ke, T. Ma, and A. J. Page, 'Defect Engineering for Photocatalysis: From Ternary to Perovskite Oxynitrides', *ChemNanoMat*, vol. 6, no. 5, pp. 708–719, 2020, doi: 10.1002/cnma.201900703.

[83] G. Doķe, 'RED AND NEAR INFRA-RED PERSISTENT LUMINESCENCE OF TRANSITION METAL ACTIVATED GERMANATE MATERIALS', 2023. doi: 10.13140/RG.2.2.29423.41128.

[84] P. Arunachalam, K. Nagai, M. S. Amer, M. A. Ghanem, R. J. Ramalingam, and A. M. Al-Mayouf, 'Recent Developments in the Use of Heterogeneous Semiconductor Photocatalyst Based Materials for a Visible-Light-Induced Water-Splitting System—A Brief Review', *Catalysts*, vol. 11, no. 2, Art. no. 2, Feb. 2021, doi: 10.3390/catal11020160.

[85] L. Huang, 'VAN DER WAALS STACKING OF TWO-DIMENSIONAL MATERIALS', Dec. 2017, Accessed: Mar. 10, 2024. [Online]. Available: https://hdl.handle.net/1813/58993

[86] E. M. Sabio, R. L. Chamousis, N. D. Browning, and F. E. Osterloh, 'Photocatalytic Water Splitting with Suspended Calcium Niobium Oxides: Why Nanoscale is Better than Bulk – A Kinetic Analysis', *J. Phys. Chem. C*, vol. 116, no. 4, pp. 3161–3170, Feb. 2012, doi: 10.1021/jp209006n.

[87] K. Maeda, M. Eguchi, W. J. Youngblood, and T. E. Mallouk, 'Calcium Niobate Nanosheets Prepared by the Polymerized Complex Method as Catalytic Materials for Photochemical Hydrogen Evolution', *Chem. Mater.*, vol. 21, no. 15, pp. 3611–3617, Aug. 2009, doi: 10.1021/cm9007766.

[88] O. C. Compton, E. C. Carroll, J. Y. Kim, D. S. Larsen, and F. E. Osterloh, 'Calcium Niobate Semiconductor Nanosheets as Catalysts for Photochemical Hydrogen Evolution from Water', *J. Phys. Chem. C*, vol. 111, no. 40, pp. 14589–14592, Oct. 2007, doi: 10.1021/jp0751155.

[89] S. A. Kurnosenko, V. V. Voytovich, O. I. Silyukov, I. A. Rodionov, E. N. Malygina, and I. A. Zvereva, 'Influence of $HB_2Nb_3O_{10}$-Based Nanosheet Photocatalysts (B = Ca, Sr) Preparation Method on Hydrogen Production Efficiency', *Catalysts*, vol. 13, no. 3, Art. no. 3, Mar. 2023, doi: 10.3390/catal13030614.

[90] K. Maeda and T. E. Mallouk, 'Comparison of two- and three-layer restacked Dion–Jacobson phase niobate nanosheets as catalysts for photochemical hydrogen evolution', *J. Mater. Chem.*, vol. 19, no. 27, p. 4813, 2009, doi: 10.1039/b903692j.

[91] Y. Okamoto, S. Ida, J. Hyodo, H. Hagiwara, and T. Ishihara, 'Synthesis and photocatalytic activity of rhodium-doped calcium niobate nanosheets for hydrogen production from a water/methanol system without cocatalyst loading', *Journal of the American Chemical Society*, vol. 133, no. 45, pp. 18034–18037, Nov. 2011, doi: 10.1021/ja207103j.

[92] M. M. J. Treacy, S. B. Rice, A. J. Jacobson, and J. T. Lewandowski, 'Electron microscopy study of delamination in dispersions of the perovskite-related layered phases $K[Ca_2Na_{n-3}Nb_nO_{3n-1}]$: evidence for single-layer formation', *Chem. Mater.*, vol. 2, no. 3, pp. 279–286, May 1990, doi: 10.1021/cm00009a018.

[93] L. Liu, M. A. Gonzalez-Olivares, H. Bai, H. Yi, and S. Song, 'Colloidal stability of silica and graphite in aqueous suspensions', *Chemical Physics*, vol. 525, p. 110405, Sep. 2019, doi: 10.1016/j.chemphys.2019.110405.

[94] M. A. Timmerman, R. Xia, Y. Wang, K. Sotthewes, M. Huijben, and J. E. Ten Elshof, 'Long-range ordering of two-dimensional wide bandgap tantalum oxide nanosheets in printed films', *Journal of Materials Chemistry C*, vol. 9, no. 17, pp. 5699–5705, 2021, doi: 10.1039/d1tc00801c.

[95] T. Oshima *et al.*, 'Two-Dimensional Perovskite Oxynitride $K_2LaTa_2O_6N$ with an H^+/K^+ Exchangeability in Aqueous Solution Forming a Stable Photocatalyst for

Visible-Light H_2 Evolution', *Angewandte Chemie - International Edition*, vol. 59, no. 24, pp. 9736–9743, Jun. 2020, doi: 10.1002/anie.202002534.

[96] A. Rao *et al.*, 'Investigating the effect of dopant type and concentration on TiO_2 powder microstructure via rietveld analysis', *Journal of Physics and Chemistry of Solids*, vol. 113, pp. 164–176, Feb. 2018, doi: 10.1016/j.jpcs.2017.10.030.

[97] 'Monitoring surface metal oxide catalytic active sites with Raman spectroscopy - Chemical Society Reviews (RSC Publishing) DOI:10.1039/C0CS00145G'. Accessed: Mar. 12, 2024. [Online]. Available: https://pubs.rsc.org/en/content/articlehtml/2010/cs/c0cs00145g

[98] V. Nadtochenko *et al.*, 'Correlations for photocatalytic activity and spectral features of the absorption band edge of TiO_2 modified by thiourea', *Applied Catalysis B: Environmental*, vol. 91, no. 1, pp. 460–469, Sep. 2009, doi: 10.1016/j.apcatb.2009.06.015.

[99] A. Landström *et al.*, 'Electron spectroscopies of 3-hydroxyflavone and 7-hydroxyflavone in MCM-41 silica nanoparticles and in acetonitrile solutions. Experimental data and DFT/TD-DFT calculations', *Data Brief*, vol. 34, p. 106630, Dec. 2020, doi: 10.1016/j.dib.2020.106630.

[100] S. Neppl and O. Gessner, 'Time-resolved X-ray photoelectron spectroscopy techniques for the study of interfacial charge dynamics', *Journal of Electron Spectroscopy and Related Phenomena*, vol. 200, pp. 64–77, Apr. 2015, doi: 10.1016/j.elspec.2015.03.002.

[101] R. S. Houk, 'Mass spectrometry of inductively coupled plasmas', *Anal. Chem.*, vol. 58, no. 1, pp. 97A-105A, Jan. 1986, doi: 10.1021/ac00292a003.

[102] A. K. Worku *et al.*, 'Structural and thermal properties of pure and chromium doped zinc oxide nanoparticles', *SN Appl. Sci.*, vol. 3, no. 7, p. 699, Jun. 2021, doi: 10.1007/s42452-021-04682-6.

[103] S. W. Chee, T. Lunkenbein, R. Schlögl, and B. Roldán Cuenya, 'Operando Electron Microscopy of Catalysts: The Missing Cornerstone in Heterogeneous Catalysis Research?', *Chem. Rev.*, vol. 123, no. 23, pp. 13374–13418, Dec. 2023, doi: 10.1021/acs.chemrev.3c00352.

[104] A. Ali, N. Zhang, and R. M. Santos, 'Mineral Characterization Using Scanning Electron Microscopy (SEM): A Review of the Fundamentals, Advancements, and Research Directions', *Applied Sciences*, vol. 13, no. 23, Art. no. 23, Jan. 2023, doi: 10.3390/app132312600.

[105] M. Thommes *et al.*, 'Physisorption of gases, with special reference to the evaluation of surface area and pore size distribution (IUPAC Technical Report)', *Pure and Applied Chemistry*, vol. 87, no. 9–10, pp. 1051–1069, Oct. 2015, doi: 10.1515/pac-2014-1117.

[106] Y. Shi, M. Osada, Y. Ebina, and T. Sasaki, 'Single Droplet Assembly for Two-Dimensional Nanosheet Tiling', *ACS Nano*, vol. 14, no. 11, pp. 15216–15226, Nov. 2020, doi: 10.1021/acsnano.0c05434.

[107] K. Oka, B. Winther-Jensen, and H. Nishide, 'Organic π-Conjugated Polymers as Photocathode Materials for Visible-Light-Enhanced Hydrogen and Hydrogen Peroxide Production from Water', *Advanced Energy Materials*, vol. 11, no. 43, p. 2003724, 2021, doi: 10.1002/aenm.202003724.

[108] Y. Xiao *et al.*, 'Oxynitrides enabled photoelectrochemical water splitting with over 3,000 hrs stable operation in practical two-electrode configuration', *Nat Commun*, vol. 14, p. 2047, Apr. 2023, doi: 10.1038/s41467-023-37754-9.

[109] H.-W. Chen *et al.*, 'Efficiency Enhancement of Hybrid Perovskite Solar Cells with MEH-PPV Hole-Transporting Layers', *Sci Rep*, vol. 6, no. 1, p. 34319, Oct. 2016, doi: 10.1038/srep34319.

[110] L. Li *et al.*, 'Dual-channel D-(π-A)2 phenoxazine/phenothiazine dyes with an auxiliary N-alkoxy benzoic acid anchor for fabrication of dye-sensitized solar cells', *Solar Energy*, vol. 225, pp. 173–183, Sep. 2021, doi: 10.1016/j.solener.2021.07.030.

[111] B. He *et al.*, 'Rapid Charge Transfer Endowed by Interfacial Ni-O Bonding in S-scheme Heterojunction for Efficient Photocatalytic H_2 and Imine Production', *Angewandte Chemie International Edition*, vol. 62, no. 50, p. e202313172, 2023, doi: 10.1002/anie.202313172.

[112] P. Wang, W. Chen, Z. Wang, Y. Tang, W. Shi, and L. Tang, 'Effect of layers on the photocatalytic hydrogen evolution in Dion–Jacobson layered-tantalum perovskites', *Dalton Trans.*, vol. 50, no. 44, pp. 16076–16083, 2021, doi: 10.1039/D1DT02069B.

[113] N. Kulischow, M. Ade, M. Weiss, and R. Marschall, 'Nitrogen-doped, proton-exchanged Dion-Jacobson layered niobate perovskites for photocatalytic hydrogen generation in solar light', *Photochemical and Photobiological Sciences*, vol. 21, no. 11, pp. 1991–2000, Nov. 2022, doi: 10.1007/s43630-022-00273-5.

[114] Y. Tang *et al.*, 'Synthesis of Three-Layer Perovskite Oxynitride $K_2Ca_2Ta_3O_9N\cdot 2H_2O$ and Photocatalytic Activity for H_2 Evolution under Visible Light', *Inorganic Chemistry*, vol. 59, no. 15, pp. 11122–11128, Aug. 2020, doi: 10.1021/acs.inorgchem.0c01607.

[115] P. Wang, W. Chen, Z. Wang, Y. Tang, W. Shi, and L. Tang, 'Effect of layers on the photocatalytic hydrogen evolution in Dion–Jacobson layered-tantalum perovskites', *Dalton Trans.*, vol. 50, no. 44, pp. 16076–16083, 2021, doi: 10.1039/D1DT02069B.

[116] 'mp-10347: $CsCa_2Ta_3O_{10}$ (Tetragonal, P4/mmm, 123)', Materials Project. Accessed: Apr. 22, 2024. [Online]. Available: https://next-gen.materialsproject.org/materials/mp-10347/

[117] M. Hojamberdiev *et al.*, 'New Dion–Jacobson Phase Three-Layer Perovskite $CsBa_2Ta_3O_{10}$ and Its Conversion to Nitrided $Ba_2Ta_3O_{10}$ Nanosheets via a Nitridation–Protonation–Intercalation–Exfoliation Route for Water Splitting', *Crystal Growth & Design*, vol. 16, no. 4, pp. 2302–2308, Apr. 2016, doi: 10.1021/acs.cgd.6b00081.

[118] M. Raciulete *et al.*, 'Strategy for modifying layered perovskites toward efficient solar light-driven photocatalysts for removal of chlorinated pollutants', *Catalysts*, vol. 10, no. 6, Jun. 2020, doi: 10.3390/catal10060637.

[119] S. Ida, Y. Okamoto, M. Matsuka, H. Hagiwara, and T. Ishihara, 'Preparation of tantalum-based oxynitride nanosheets by exfoliation of a layered oxynitride, $CsCa_2Ta_3O_{10-x}N_y$, and their photocatalytic activity', *Journal of the American Chemical Society*, vol. 134, no. 38, pp. 15773–15782, Sep. 2012, doi: 10.1021/ja3043678.

[120] H. J. Yun, D. M. Lee, S. Yu, J. Yoon, H.-J. Park, and J. Yi, 'Effect of valence band energy on the photocatalytic performance of N-doped TiO_2 for the production of O2 via the oxidation of water by visible light', *Journal of Molecular Catalysis A: Chemical*, vol. 378, pp. 221–226, Nov. 2013, doi: 10.1016/j.molcata.2013.06.016.

[121] M. B. Clavel, S. Bhattacharya, and M. K. Hudait, 'Atomic layer deposited tantalum silicate on crystallographically-oriented epitaxial germanium: interface chemistry

and band alignment', *Mater. Adv.*, vol. 3, no. 12, pp. 5001–5011, Jun. 2022, doi: 10.1039/D2MA00208F.

[122] K. Saito *et al.*, 'Lepidocrocite-Type Layered Titanate Nanoparticles as Photocatalysts for H_2 Production', *ACS Appl. Nano Mater.*, vol. 5, no. 7, pp. 9053–9062, Jul. 2022, doi: 10.1021/acsanm.2c01353.

[123] D. Liu *et al.*, 'Hydrogen evolution activity enhancement by tuning the oxygen vacancies in self-supported mesoporous spinel oxide nanowire arrays', *Nano Res.*, vol. 11, no. 2, pp. 603–613, Feb. 2018, doi: 10.1007/s12274-017-1670-8.

[124] T. Üstünel, Y. Ide, S. Kaya, and E. Doustkhah, 'Single-Atom Sn-Loaded Exfoliated Layered Titanate Revealing Enhanced Photocatalytic Activity in Hydrogen Generation', *ACS Sustainable Chem. Eng.*, vol. 11, no. 8, pp. 3306–3315, Feb. 2023, doi: 10.1021/acssuschemeng.2c06181.

[125] T. Xiao, X. Liu, and J. Wang, 'Influence of Nitrogen Substitution on the Electronic Structure of Ti_2O_3: Insights into the Doping-Induced Insulator-to-Metal Transition', *physica status solidi (b)*, vol. 260, no. 6, p. 2200495, 2023, doi: 10.1002/pssb.202200495.

[126] S. Hann, E. Rudolph, G. Köllensperger, and C. Reiter, 'Analysis of Palladium by High Resolution ICP-MS', in *Palladium Emissions in the Environment: Analytical Methods, Environmental Assessment and Health Effects*, F. Zereini and F. Alt, Eds., Berlin, Heidelberg: Springer, 2006, pp. 73–82. doi: 10.1007/3-540-29220-9_5.

[127] D. V. Wellia, 'Green preparation of visible light active titanium dioxide films', Nanyang Technological University, 2012. doi: 10.32657/10356/50674.

[128] W. Wang *et al.*, 'Understanding improved photoelectrochemical performance in $Ba_xSr_{1-x}TiO_3/TiO_2$ rod-shell nanostructures', *AIP Advances*, vol. 11, no. 9, Sep. 2021, doi: 10.1063/5.0062958.

[129] M. Irshad *et al.*, 'Photocatalysis and perovskite oxide-based materials: a remedy for a clean and sustainable future', *RSC Advances*, vol. 12, no. 12, pp. 7009–7039, Mar. 2022, doi: 10.1039/d1ra08185c.

[130] D. Liu *et al.*, 'Single noble metal atoms doped 2D materials for catalysis', *Applied Catalysis B: Environmental*, vol. 297, p. 120389, Nov. 2021, doi: 10.1016/j.apcatb.2021.120389.

[131] Z. Chen, J. Zhao, C. R. Cabrera, and Z. Chen, 'Computational Screening of Efficient Single-Atom Catalysts Based on Graphitic Carbon Nitride (g-C_3N_4) for Nitrogen Electroreduction', *Small Methods*, vol. 3, no. 6, 2019, doi: 10.1002/smtd.201800368.

[132] 'mp-10347: $CsCa_2Ta_3O_{10}$ (Tetragonal, P4/mmm, 123)', Materials Project. Accessed: Mar. 27, 2024. [Online]. Available: https://next-gen.materialsproject.org/materials/mp-10347

[133] T. Kumari, R. Gopal, A. Goyal, and J. Joshi, 'Sol–Gel Synthesis of Pd@PdO Core–Shell Nanoparticles and Effect of Precursor Chemistry on Their Structural and Optical Properties', *J Inorg Organomet Polym*, vol. 29, no. 2, pp. 316–325, Mar. 2019, doi: 10.1007/s10904-018-1001-x.

[134] C.-C. Hu, C.-C. Tsai, and H. Teng, 'Structure Characterization and Tuning of Perovskite-Like $NaTaO_3$ for Applications in Photoluminescence and Photocatalysis', *Journal of the American Ceramic Society*, vol. 92, no. 2, pp. 460–466, 2009, doi: 10.1111/j.1551-2916.2008.02869. x.

[135] A. Yamakata and J. J. M. Vequizo, 'Curious behaviors of photogenerated electrons and holes at the defects on anatase, rutile, and brookite TiO_2 powders: A review',

Journal of Photochemistry and Photobiology C: Photochemistry Reviews, vol. 40, pp. 234–243, Sep. 2019, doi: 10.1016/j.jphotochemrev.2018.12.001.

[136] A. Kudo and T. Sakata, 'Effect of Ion Exchange on Photoluminescence of Layered Niobates $K_4Nb_6O_{17}$ and KNb_3O_8', *J. Phys. Chem.*, vol. 100, no. 43, pp. 17323–17326, Jan. 1996, doi: 10.1021/jp9619806.

[137] A. Kudo and E. Kaneko, 'Photoluminescent properties of ion-exchangeable layered oxides', *Microporous and Mesoporous Materials*, vol. 21, no. 4–6, pp. 615–620, May 1998, doi: 10.1016/S1387-1811(98)00037-7.

[138] 'NIST X-ray Photoelectron Spectroscopy Database'. Accessed: Apr. 19, 2024. [Online]. Available: https://srdata.nist.gov/xps/QueryByElmType/Pd/PE

[139] S. Sun, H. Li, and Z. J. Xu, 'Impact of Surface Area in Evaluation of Catalyst Activity', *Joule*, vol. 2, no. 6, pp. 1024–1027, Jun. 2018, doi: 10.1016/j.joule.2018.05.003.

[140] R. Uppuluri, A. S. Gupta, A. S. Rosas, and T. E. Mallouk, 'Soft chemistry of ion-exchangeable layered metal oxides', *Chem. Soc. Rev.*, vol. 47, no. 7, pp. 2401–2430, Apr. 2018, doi: 10.1039/C7CS00290D.

[141] W. Chen, T.-Y. Liu, T. Huang, X.-H. Liu, and X.-J. Yang, 'Novel mesoporous P-doped graphitic carbon nitride nanosheets coupled with $ZnIn_2S_4$ nanosheets as efficient visible light driven heterostructures with remarkably enhanced photo-reduction activity', *Nanoscale*, vol. 8, no. 6, pp. 3711–3719, Feb. 2016, doi: 10.1039/C5NR07695A.

[142] C. P. Canales, 'Electrochemical Impedance Spectroscopy and Its Applications', in *21st Century Nanostructured Materials - Physics, Chemistry, Classification, and Emerging Applications in Industry, Biomedicine, and Agriculture*, IntechOpen, 2021. doi: 10.5772/intechopen.101636.

[143] N. Iqbal, A. Afzal, I. Khan, M. S. Khan, and A. Qurashi, 'Molybdenum impregnated g-C3N4 nanotubes as potentially active photocatalyst for renewable energy applications', *Sci Rep*, vol. 11, no. 1, p. 16886, Aug. 2021, doi: 10.1038/s41598-021-96490-6.

[144] T. Liu, M. Dupuis, and C. Li, 'Band Structure Engineering: Insights from Defects, Band Gap, and Electron Mobility, from Study of Magnesium Tantalate', *J. Phys. Chem. C*, vol. 120, no. 13, pp. 6930–6937, Apr. 2016, doi: 10.1021/acs.jpcc.5b12314.

[145] P. R. Mishra, P. K. Shukla, A. K. Singh, and O. N. Srivastava, 'Investigation and optimization of nanostructured TiO_2 photoelectrode in regard to hydrogen production through photoelectrochemical process', *International Journal of Hydrogen Energy*, vol. 28, no. 10, pp. 1089–1094, Oct. 2003, doi: 10.1016/S0360-3199(02)00197-0.

[146] S. Kang *et al.*, 'Intercalation–exfoliation processes during ionic exchange reactions from sodium lepidocrocite-type titanate toward a proton-based trititanate structure', *Phys. Chem. Chem. Phys.*, vol. 23, no. 17, pp. 10498–10508, May 2021, doi: 10.1039/D1CP00352F.

[147] 'Single-atom catalysis of CO oxidation using Pt_1/FeO_x | Nature Chemistry'. Accessed: Mar. 13, 2024. [Online]. Available: https://www.nature.com/articles/nchem.1095

[148] P. Wang, W. Chen, Z. Wang, Y. Tang, W. Shi, and L. Tang, 'Effect of layers on the photocatalytic hydrogen evolution in Dion-Jacobson layered-tantalum perovskites', *Dalton Transactions*, vol. 50, no. 44, pp. 16076–16083, Nov. 2021, doi: 10.1039/d1dt02069b.

[149] Á. Fernández-Galiana, O. Bibikova, S. Vilms Pedersen, and M. M. Stevens, 'Fundamentals and Applications of Raman-Based Techniques for the Design and Development of Active Biomedical Materials', *Advanced Materials*, vol. n/a, no. n/a, p. 2210807, doi: 10.1002/adma.202210807.

[150] T. Kumari, R. Gopal, A. Goyal, and J. Joshi, 'Sol–Gel Synthesis of Pd@PdO Core–Shell Nanoparticles and Effect of Precursor Chemistry on Their Structural and Optical Properties', *J Inorg Organomet Polym*, vol. 29, no. 2, pp. 316–325, Mar. 2019, doi: 10.1007/s10904-018-1001-x.

[151] S. K. Suram, P. F. Newhouse, and J. M. Gregoire, 'High Throughput Light Absorber Discovery, Part 1: An Algorithm for Automated Tauc Analysis', *ACS Comb. Sci.*, vol. 18, no. 11, pp. 673–681, Nov. 2016, doi: 10.1021/acscombsci.6b00053.

[152] A. Kösemen, Z. A. Kösemen, S. Öztürk, N. Kılınç, S. E. San, and A. V. Tunç, 'Electrochemical Growth of Pd Doped ZnO Nanorods', *J. Electrochem. Soc.*, vol. 162, no. 4, p. D142, Jan. 2015, doi: 10.1149/2.0341504jes.

[153] A. K. Mohamedkhair, Q. A. Drmosh, M. Qamar, and Z. H. Yamani, 'Tuning Structural Properties of WO3 Thin Films for Photoelectrocatalytic Water Oxidation', *Catalysts*, vol. 11, no. 3, Art. no. 3, Mar. 2021, doi: 10.3390/catal11030381.

[154] M. Yadav *et al.*, 'Strategically fabricated Ag loaded Fe-g-C_3N_4 nanosheet for photocatalytic removal of aqueous organic pollutant', *Optical Materials*, vol. 125, p. 112043, Mar. 2022, doi: 10.1016/j.optmat.2022.112043.

[155] W. Zhou, T. Jiang, Y. Zhao, C. Xu, C. Pei, and H. Xue, 'Ultrathin Ti/TiO_2/$BiVO_4$ nanosheet heterojunction arrays for photoelectrochemical water oxidation', *Journal of Alloys and Compounds*, vol. 777, pp. 1152–1158, Mar. 2019, doi: 10.1016/j.jallcom.2018.11.078.

[156] N. O. Laschuk, E. B. Easton, and O. V. Zenkina, 'Reducing the resistance for the use of electrochemical impedance spectroscopy analysis in materials chemistry', *RSC Adv*, vol. 11, no. 45, pp. 27925–27936, doi: 10.1039/d1ra03785d.

[157] Y. Li, L. Wang, J. Liang, F. Gao, K. Yin, and P. Dai, 'Hierarchical Heterostructure of ZnO@TiO_2 Hollow Spheres for Highly Efficient Photocatalytic Hydrogen Evolution', *Nanoscale Res Lett*, vol. 12, no. 1, p. 531, Sep. 2017, doi: 10.1186/s11671-017-2304-5.

[158] B. Qiao *et al.*, 'Single-atom catalysis of CO oxidation using Pt1/FeOx', *Nature Chem*, vol. 3, no. 8, pp. 634–641, Aug. 2011, doi: 10.1038/nchem.1095.

[159] L. Ju *et al.*, 'Controllable CO_2 electrocatalytic reduction via ferroelectric switching on single atom anchored In2Se3 monolayer', *Nature Communications*, vol. 12, 2021, doi: 10.1038/s41467-021-25426-5.

[160] T. Üstünel, Y. Ide, S. Kaya, and E. Doustkhah, 'Single-Atom Sn-Loaded Exfoliated Layered Titanate Revealing Enhanced Photocatalytic Activity in Hydrogen Generation', *ACS Sustainable Chem. Eng.*, vol. 11, no. 8, pp. 3306–3315, Feb. 2023, doi: 10.1021/acssuschemeng.2c06181.

[161] J. Wang, T. Liao, Z. Wei, J. Sun, J. Guo, and Z. Sun, 'Heteroatom-Doping of Non-Noble Metal-Based Catalysts for Electrocatalytic Hydrogen Evolution: An Electronic Structure Tuning Strategy', *Small Methods*, vol. 5, no. 4, p. 2000988, 2021, doi: 10.1002/smtd.202000988.

[162] Y. Akinay, H. C. Kazici, I. N. Akkuş, and F. Salman, 'Synthesis of 3D Sn doped Sb2O3 catalysts with different morphologies and their effects on the electrocatalytic hydrogen evolution reaction in acidic medium', *Ceramics*

International, vol. 47, no. 20, pp. 29515–29524, Oct. 2021, doi: 10.1016/j.ceramint.2021.07.278.

[163] S.-T. Bae, H. Shin, S. Lee, D. W. Kim, H. S. Jung, and K. S. Hong, 'Visible-light photocatalytic activity of NH_3-heat-treated Ta_2O_5 to decompose rhodamine B in aqueous solution', *Reac Kinet Mech Cat*, vol. 106, no. 1, pp. 67–81, Jun. 2012, doi: 10.1007/s11144-011-0404-2.

[164] T. Helmenstine, 'List of Electronegativity Values of the Elements', Science Notes and Projects. Accessed: Apr. 18, 2024. [Online]. Available: https://sciencenotes.org/list-of-electronegativity-values-of-the-elements/

[165] T. Üstünel, Y. Ide, S. Kaya, and E. Doustkhah, 'Single-Atom Sn-Loaded Exfoliated Layered Titanate Revealing Enhanced Photocatalytic Activity in Hydrogen Generation', *ACS Sustainable Chem. Eng.*, vol. 11, no. 8, pp. 3306–3315, Feb. 2023, doi: 10.1021/acssuschemeng.2c06181.

[166] X. Liu *et al.*, 'Highly exposed discrete Co atoms anchored in ultrathin porous N, P-codoped carbon nanosheets for efficient oxygen electrocatalysis and rechargeable aqueous/solid-state Zn–air batteries', *J. Mater. Chem. A*, vol. 9, no. 39, pp. 22643–22652, Oct. 2021, doi: 10.1039/D1TA07404K.

[167] B. 1 Babu, S. G. Peera 2, K. 1 1 S. of M. E. Yoo, and K. U. babu. physicist@gmail.com 2 Department of Environmental Science, 'Fabrication of ZnWO4-SnO2 Core–Shell Nanorods for Enhanced Solar Light-Driven Photoelectrochemical Performance', p. 213, 2023, doi: 10.3390/inorganics11050213.

[168] P. Yadav, S. Yadav, S. Atri, and R. Tomar, 'A Brief Review on Key Role of Perovskite Oxides as Catalyst', *ChemistrySelect*, vol. 6, no. 45, pp. 12947–12959, 2021, doi: 10.1002/slct.202102292.

[169] J. Seo and K. Domen, 'Perovskite and layered perovskite oxynitrides for efficient sunlight-driven artificial synthesis', *Materials Chemistry Frontiers*, vol. 8, no. 6, pp. 1451–1479, 2024, doi: 10.1039/D3QM01019H.